UNIVERSITY OF LIVERPOOL

Doctoral Thesis

The Role of Magmatism at Rifted Margins

Thesis submitted in accordance with the requirements of the University of Liverpool for the degree of Doctor in Philosophy

By

Caroline J. Harkin

March 2019

Declaration of Authorship

I declare that this thesis titled 'The role of magmatism at rifted margins' and the work therein are my own work. The material contained within this thesis has not been presented, nor is currently been presented, either wholly or in part, for any other degree or qualification.

Signed:

_____

Caroline J. Harkin

March 2019

Abstract

Rifted margins form by the thinning and stretching of continental lithosphere until it ruptures, forming new oceanic crust and lithosphere, which can be accompanied by decompression melting and the addition of magmatic material. Despite numerous studies on magma-rich margins, we still do not fully understand how and when magmatic features form at rifted margins. To address this I investigate the formation of various magmatic features on three rifted margins, the East Indian margin, the Pelotas margin and the Southeast (SE) Greenland margin, using a range of quantitative techniques.

The East Indian margin is an often-cited example of a magma-poor margin; however, some interpretations suggest the transition from exhumed mantle to oceanic crust consists of 9 km thick magmatic crust. Gravity inversion, RDA analysis, subsidence analysis and joint inversion of seismic and gravity data alongside seismic observations, reveal the presence of magma-poor and magma-rich characteristics in the form of exhumed mantle and 9 km thick magmatic crust juxtaposed against each other, resulting from a two-stage breakup. Juxtaposition of end-member characteristics suggests that the use of end-member terminology based on volumes of magma alone is misleading.

The Pelotas margin in the South Atlantic shows an extraordinarily thick sequence of seaward dipping reflectors (SDRs), of which the composition and formation is poorly understood. I investigate these SDRs using gravity inversion with a sensitivity to basalt/sediment composition, flexural backstripping and reverse thermal subsidence modelling, joint inversion of seismic and gravity data and seismic observations. I show there are two types of SDRs present on the Pelotas margin, an inner subaerial set of SDRs formed of basalt during pre-breakup intra-continental rifting and an outer set of SDRs formed of a mix of volcaniclastics and basalts during breakup in a subaqueous environment at an embryonic mid-ocean ridge.

The SE Greenland margin in the North Atlantic has a broad region of ~15 km thick crust and exhibits strong crustal asymmetry with its conjugate Hatton Bank similar to magma-poor margins. I investigate whether the SE Greenland margin consists of magmatic crust or hyper-extended continental crust sandwiched by magmatic material. Gravity inversion, joint inversion of seismic and gravity data as well as seismic velocity analysis suggest the 15 km thick crust on the SE Greenland margin is magmatic rather than a sandwich of thinned continental crust and magmatic additions. This interpretation requires a sharp continent-ocean boundary, similar to Hatton Bank.

Together, these case studies investigate the relationship between magmatism and breakup at rifted margins. The East Indian margin suggests that the use of end-member terminology in the classification of rifted margins is misleading when based only on the magmatic budget. The Pelotas margin shows how extrusive magmatism can record different stages in margin formation. Finally, the SE Greenland margin shows the importance of using quantitative techniques to interpret margin structure and subsequent formation processes.

Acknowledgements

Firstly, I want to thank Nick Kusznir, for your years of dedication and encouragement as my supervisor. Your enthusiasm and knowledge know no bounds, constantly inspiring me to be a better scientist. You have been patient, kind and I cannot imagine having a better supervisor. Thank you for taking a chance on me.

Thank you to the MM4 consortium who funded this PhD and everyone who was involved. I would particularly like to thank Gianreto Manatschal for his supervision and for showing me that geology is not all that bad. Thank you as well to Alan Roberts who constantly offered up his knowledge and advice, which has been invaluable.

To those in the department, I want to thank you for making this PhD fun. To my office mates, past and present, it has been a real hoot. Thank you to Oliver, Cécile, Elliot, Becky, James, Ludo, Anthony, Amy, Jenny, Josh and everyone else!

I have to say a big thank you to Júlia for being there every step of the way. We may have started our PhDs as strangers, but we will be finishing together as friends for life. Over the past four years we have grown together, shared many memories and learnt far too much about rifted margins and I would do it all over again… except Tasna!

To Louise, Suraya and Mila, you guys rock. Here's too many more years of nonsensical conversation and coffee days complete with cake. Your advice and support, often in the form of gifs, got me through the hard times. We may now be separated by many miles and several time zones, but I am sure we will always be there cheering each other on.

I want to thank my family for nodding along when I talk about my research. It is not the world's most interesting subject but you all always listened and it meant a lot to me. To Emma and Sarah, thank you for being the best sisters I could have asked for. To my parents, you have given me unwavering support and always encouraged me to be the best person I can be. I don't know if any words can express how grateful I am and how lucky I am to have you both as my parents.

Finally, thank you to Simon. This has been a real journey and I could not have done it without you by my side. Thank you for being patient and feeding me when I was hangry. Together with Casper, you keep me smiling and I hope it continues for many years to come.

Contents

Chapter 1

Introduction

1.1 Aims

A rifted margin is formed by the rupture and separation of continental lithosphere generating new oceanic lithosphere, resulting in thinned continental crust transitioning to new oceanic crust. Rifted margins represent palaeo-plate boundaries and are a fundamental part of the Wilson cycle and plate tectonics. Presently, rifted margins account for ~42% of the world's tectonic boundaries with a total collective length of ~105,000 km, longer than convergent margins, spreading ridges and transform margins (Bradley, 2008).

Most of what we know about the structure and formation of rifted margins comes from extensive studies of magma-poor rifted margins. Despite a large number of studies on magma-rich rifted margins, much less is known about their structure and formation as the addition of magma makes it harder to image and access the structures on rifted margins, meaning that detailed studies of magma-rich margins have been limited. However, advances in technology, in particular the use of long-offset wide-angle seismic reflection data, now image all areas of rifted margins including magmatic features such as high-velocity lower crustal bodies, seaward dipping reflector sequences, sill intrusions and new magmatic basement.

Within this PhD, I investigate the role of magma within rifted margins, in particular how magmatic features such as seaward dipping reflectors and the formation of magmatic basement relate to breakup using various quantitative geophysical techniques. The quantitative geophysical techniques consist of gravity anomaly inversion, residual depth anomaly (RDA) analysis, subsidence analysis, seismic velocity analysis, palaeobathymetry analysis and joint gravity and seismic inversion of Moho data. Each method investigates certain aspects of a rifted margin, for example, subsidence analysis calculates lithosphere thinning factors, which predict the extent of continental crust while the joint gravity and seismic inversion examines lateral variations in basement density and seismic velocity. Integrating the results of each geophysical technique provides a better understanding of the main structures on the margin, which can then be used to discuss the parameters that control magmatism. Rifted margins can provide an insight into mantle dynamics

To investigate the role of magma at rifted margins, three diverse rifted margins were selected for study: the East Indian margin, the Pelotas margin of the South Atlantic and the Southeast (SE) Greenland margin of the Northeast (NE) Atlantic. The East Indian margin is regarded as a classic magma-poor margin displaying typical characteristics of exhumed mantle and crustal thinning with very little magmatism. The Pelotas margin exhibits an anomalous amount of extrusive magmatism in the form of seaward dipping reflectors. Finally, the SE Greenland margin displays asymmetry when compared to its conjugate Hatton Bank, similar to magma-poor rifted margins such as Iberia-Newfoundland, but is interpreted to consist entirely of igneous material. Examining margins with varying degrees of magmatism allows us to understand the diversity of magmatism and its relationship to rifted margin formation.

In particular, the chapters within this thesis aim to examine:

1) The use of end-member terminology, i.e. magma-poor vs. magma-rich, to classify rifted margins.
2) The composition and timing relative to breakup of extrusive magmatism in the form of seaward dipping reflectors, on magma-rich margins.
3) The depositional environment of seaward dipping reflectors during breakup.
4) The formation of asymmetric magma-rich conjugate margins.

Resolving these aims will improve how we classify rifted margins, but also improve our understanding of the controls on magmatism at rifted margins, in particular the controlling parameter on rifted margin magmatism, whether it is elevated mantle temperatures or active upwelling, both of which can be related to mantle plumes. Mantle plumes are often credited with influencing rifted margin formation; I use the results of this thesis to discuss the level of influence mantle plumes have in rifted formation.

1.2 Thesis structure

Chapters 3, 4, 5 and 6 are first-authored papers of which Chapter 3 is published, Chapter 4 is under review and Chapters 5 and 6 are ready for submission to their relevant journals. Each chapter is structured to stand alone, with an abstract, an introduction, a methodology, results, a discussion and a conclusion. Some of the topics discussed within each paper are repeated and overlap, in particular the introduction and methodology of each. These papers have been incorporated as chapters with none of the duplicated material removed in order to preserve the overall integrity of each paper. Each chapter begins with a summary introduction detailing the aim of the paper within the overall aim of the thesis, the publication status as well as co-author contributions. Figure numbers within each chapter have been altered to be consecutive throughout the thesis, while the references have been combined into an overall bibliography at the end of the thesis. A summary of the methods used throughout the thesis is provided in Appendix A.

Chapter 3 investigates the ocean-continent transition structure of the magma-poor East Indian margin. Within the paper, we question the definition of magma-poor vs. magma-rich rifted margins. We integrate various quantitative geophysical techniques such as gravity inversion, residual depth anomaly analysis, subsidence analysis and joint inversion of gravity and seismic Moho data to validate different geological interpretations based on seismic data. In doing so, we aim to improve our understanding of tectonic and magmatic processes and the subsequent classification of magma-poor and magma-rich rifted margins.

Chapter 4 discusses the formation of SDR sequences in the Pelotas Basin, offshore Brazil. Contrasting formation models for SDRs exist, two of them are the volcanic faulting model and volcanic loading model and there is no consensus as to which model is the most appropriate. We combine seismic observations and gravity anomaly inversion with a sensitivity to basalt/sediment SDR composition to investigate the origin, composition and timing of the SDRs relative to breakup to investigate if either the formation models are applicable. With this work, we aim to better understand the relationship between extrusive magmatism and breakup.

Chapter 5 also looks at the SDR sequences in the Pelotas Basin but investigates SDR palaeobathymetries using flexural backstripping and reverse thermal subsidence modelling for end-member compositions and densities from joint inversion of time seismic and gravity data. Subaerial vs. subaqueous SDR formation is often debated throughout formation models with conflicting evidence from seismic studies and drill hole data. We combine

palaeobathymetry estimates with density analysis to interpret the depositional environment of the SDR package. With this knowledge, we can constrain the evolution of the Pelotas margin relative to breakup and improve our understanding of deep-water petroleum systems.

Chapter 6 looks at the Southeast (SE) Greenland margin, in particular it focuses on the composition of the basement from the proximal to distal domains as the SE Greenland margin displays asymmetry similar to magma-poor margins when compared against its conjugate, Hatton bank. If the conjugate structure of SE Greenland-Hatton Bank is similar to magma-poor margins, it could imply a similar tectonic evolution. Using gravity inversion, seismic velocity analysis and joint inversion of gravity and seismic Moho data, we investigate whether the basement is likely to be composed of magmatic material or hyper-extended continental crust surrounded by extrusive and intrusive material. By analysing and interpreting the structure of the basement on the SE Greenland margin, we can gain a better understanding of the breakup mechanism.

Chapter 7 presents the main discussion and conclusions of the thesis, discussing the individual chapters together to address the overall theme of magma and breakup along with the parameters that control magmatism at rifted margins.

Chapter 2

Background

2.1 What is a rifted margin?

Within this chapter I define what a rifted margin is using structural domains and I review the current viewpoints of rifted margin formation, giving an overview of the features found within the ocean-continent transitions at magma poor and magma rich margins so that the difference between end member margins is clear. This thesis aims to add to this current knowledge, in particular to our knowledge of magmatic features at rifted margins and the potential parameters that form them. Historically, investigation of magma rich margins has been difficult, mainly due to imaging problems, so the features common to magma rich margins are less understood than the features seen at magma-poor margins. Later chapters will focus on the formation of seaward dipping reflectors, a characteristic feature of magma rich margins formed during breakup, and basement composition within ocean-continent transition zones, which is often debated.

A rifted margin develops from the rupture and separation of continental lithosphere to form new oceanic lithosphere, generating thinned continental crust that transitions into new oceanic crust. The simplest description of a rifted margin would be normal thickness

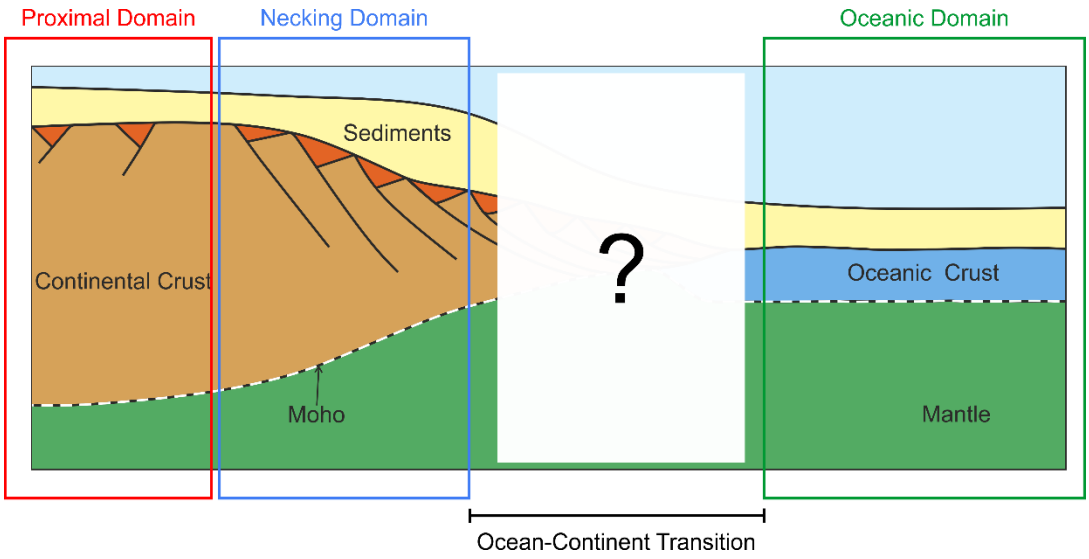

Fig. 2.1 Simple cross-sectional view of a rifted margin with general structural domains identified: Proximal Domain, Necking Zone, and Oceanic Domain. The location of the ocean-continent transition is also labelled.

continental crust thinned to a point where it breaks, allowing the formation of new oceanic crust with a clear, defined boundary between the two crustal types (Fig. 2.1).

In reality, rifted margins are more complex and vary globally. To be able to compare and contrast various rifted margins, structural domains have been defined based predominantly on crustal thickness and lithosphere thinning (Manatschal, 2004; Mohn et al., 2012; Sutra and Manatschal, 2012; Tugend et al., 2014a), where β-factors are used to quantify the amount of stretching that continental crust has undergone (Table 2.1). The β-factor is defined as the ratio of initial continental crustal thickness to current continental crustal thickness assuming pure shear deformation (McKenzie, 1978). Low β-factors denote small amounts of stretching and high β-factors represent large amounts of stretching which is related to thinning through the relationship $\gamma = 1 - 1/\beta$ (Chappell and Kusznir, 2008a; Greenhalgh and Kusznir, 2007; Kusznir et al., 2018). Throughout this thesis, crustal extension is assumed to undergo pure shear deformation, in which the entire lithosphere stretches and thins by the same amount (McKenzie, 1978). Alternatively, there exists the simple-shear extensional model, which can be related to depth-dependent stretching and thinning, whereby the upper lithosphere appears to be less extended than the whole lithosphere (Davis and Kusznir, 2004; Karner and Driscoll, 1999; Kusznir and Karner, 2007). The occurrence of depth-dependent stretching and thinning is debated, with the extension discrepancy currently only observed at proximal and necking domains (Davis and Kusznir, 2004), leading to suggestions that it is a by-product of the limitation of seismic imaging (Reston, 2007).

Within oceanic crust, β is infinity as continental crustal thickness is zero. Areas that have undergone extension can be generalised into low- and high-β environments (Tugend et al., 2014a; Wilson et al., 2001). A low β-factor environment is characterised by high-angle normal faults and half-graben type basins containing wedge-shaped sedimentary sequences that thicken towards the footwall. A high β-factor environment displays large normal faults, which accommodate kilometres of displacement resulting in the pronounced thinning of the crust. At very large extensions, the footwall of these faults can be exhumed creating 'new' basement. It is important to note that the active portion of these faults is considered to be the high-angle area situated within the crust and not the exhumed footwall.

Generally, a rifted margin will have the following structural domains; the proximal domain, the necking domain and the oceanic domain (Fig. 2.1), which can be defined using stretching and thinning factors (Table 2.1.). Depending on the type of rifted margin, the area between

the necking and oceanic domains, defined here as the ocean-continent transition (OCT), can vary.

Domain	Crustal Thickness (km)	Stretching Factor (β)	Thinning Factor (γ)
Proximal	25 +	< 1.25	0.0 – 0.3
Necking	25 – 10	1.25 - 4	0.3 – 0.7
Ocean-Continent Transition	?	?	?
Oceanic	7	∞	1.0

Table 2.1. Summary of rifted margin structural domains and the associated crustal thicknesses, stretching factors and thinning factors. Thinning factors and crustal thicknesses taken from Cowie et al. (2015). Stretching factors calculated using the ratio of initial crustal thickness (35 km) to stretched crustal thickness.

The proximal domain is situated continentward of a rifted margin, where continental crust has undergone moderate extension from normal thickness, 40-35 km (Christensen and Mooney, 1995), to 30-25 km. The proximal domain is an example of a low β-factor environment (β<1.25) with small amounts of stretching and thinning over a wide area (>200 km), accommodated by a series of high-angle normal faults (Manatschal, 2004). Prior to formation of a rifted margin these areas would correspond to intra-continental rifts.

Extension of continental crust below 25 km to 10 km thickness within a narrow area, ~50-60 km (Osmundsen and Ebbing, 2008) is defined as the necking domain (Mohn et al., 2012). Necking initiates when continental crust is decoupled from the lithosphere by the weak and ductile lower crust. This rheology structure, combined with the lithosphere having a higher viscosity than continental crust, means necking of the lithosphere occurs first which results in a loss of strength, causing it to rebound. The rebounding of the lithosphere then results in the necking of continental crust (Chenin et al., 2018). Necking of continental crust over a narrow area necessitates a sharp change to a steeply dipping Moho from a relatively flat-lying geometry in the proximal domain (Lau et al., 2006). β-factors for the necking domain are 1.25-4, due to the extreme crustal thinning and the domain is a high β-environment transitioning from a low β-factor environment.

Eventually, rupture of the continental lithosphere leads to the production of steady-state oceanic crust and lithosphere that defines the oceanic domain, where β is infinity. Within the oceanic domain, Penrose-type oceanic crust consists of three distinct layers, layer 1 which is sedimentary, layer 2 which consists of extrusive basalts and dykes and layer 3 which is the thickest, composed of intrusive gabbroic rocks (White et al., 1992).

Throughout this thesis the terms ‘seismic Moho’ and ‘gravity inversion Moho’ are consistently used. The ‘seismic Moho’ is defined as the deepest continuous reflector visible on seismic reflection images that lies within a reasonable Moho range as defined by Warner (1987). The ‘gravity inversion Moho’ is the position of the density contrast between continental crust and mantle, calculated in the gravity inversion by inverting free air gravity for the depth to the Moho accounting for lithosphere thermal effects and the addition of magma. Where the seismic and gravity inversion Mohos coincide suggests the basement is predominantly homogeneous, while the mismatch of both Mohos suggests there are some lateral heterogeneities within the basement. Where differences between the seismic and gravity inversion Mohos occurs we use the joint inversion of seismic and gravity data to investigate the cause.

2.2 Types of rifted margins

The volume of magma has long been identified as a feature that varies across rifted margins with some rifted margins displaying excessive amounts (>10 km thickness) while others demonstrate very little magmatism. As a result, rifted margins were classified as either volcanic or non-volcanic based on the presence or supposed lack of magma (Sawyer et al., 2007). Later studies demonstrated the misleading nature of these terms (Reston, 2009; Reston and Manatschal, 2011) and instead proposed the terms ‘magma-poor’ and ‘magma-rich’ as even non-volcanic rifted margins display some evidence of magmatism.

In addition to the magma-poor and magma-rich classification, there are alternative ways to classify rifted margins. Rifted margins can be classified as narrow or wide based on the lateral extent of rift-related structures. Whether a margin is characterised as narrow or wide is attributed to lithospheric strength. Wide margins, consisting of continental crust extended for 50-600 km, develop from thickened crust and lithosphere, while narrow margins have a sharp transition zone, which develops from normal thickness crust and lithosphere with a strong sub-mantle (Brun, 1999). Where rifting is accompanied by magmatism, lithosphere strength profiles change and necking of the crust is localised, producing narrow margins, as magmatism is usually associated with elevated mantle temperatures (Davison, 1997; White and McKenzie, 1989). Additionally, the symmetry vs asymmetry of a conjugate rifted margin system is a useful way of classifying margins. Within this thesis, we concentrate on the volume of magma to distinguish between rifted margin types, although the different ways of classifying margins can sometimes overlap.

The main differences between magma-poor and magma-rich margins have been summarised in several studies, e.g. Tugend et al. (2018), Dore and Lundin (2015), Franke (2013) and Geoffroy (2005) as well as in Figure 2.2. One of the most notable differences includes the discrepancy in the timing and volume of magmatism. Many factors contribute towards this discrepancy between rifted margins, such as mantle fertility, asthenosphere temperature, active upwelling and strain rates within the lithosphere (Fletcher et al., 2009).

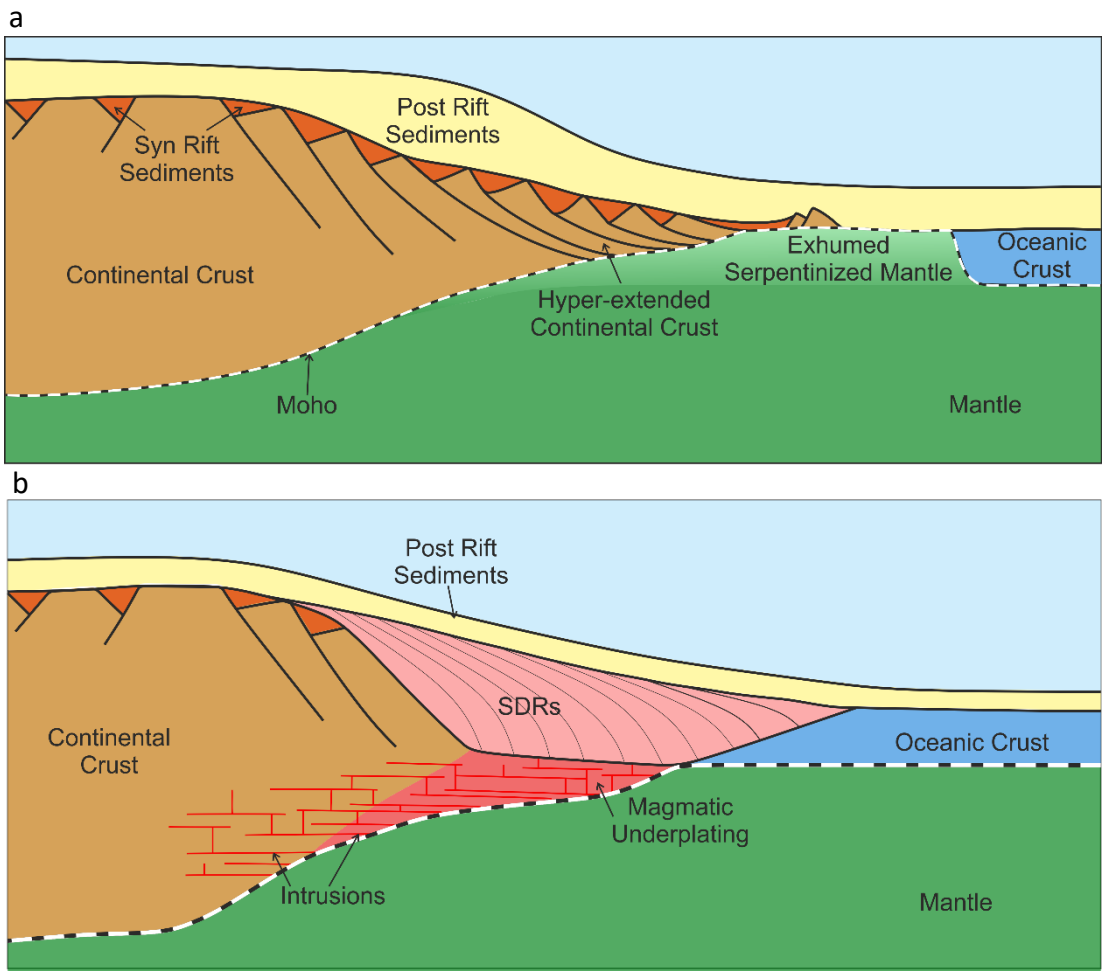

Fig. 2.2 Cartoons summarising main differences between end-member rifted margins. a) Cartoon of a typical magma-poor rifted margin displaying a wide region of thinned continental crust, hyper-extended continental crust and exhumed serpentinised mantle. b) Cartoon of a typical magma-rich rifted margin showing a narrow area of continental thinning, extrusive magmatism in the form of seaward dipping reflectors (SDRs) and intrusive magmatism in the form of magmatic underplating and sills and dykes.

A magma-poor rifted margin, in brief, typically displays zones of extreme crustal thinning over a wide area, hyper-extension of continental crust, exhumed serpentinised mantle and oceanic crust (Fig. 2.2a). Examples of such margins include Iberia-Newfoundland (Péron-Pinvidic and Manatschal, 2009; Sibuet et al., 2007), the fossilised Alpine-Tethyan rifted margins (Masini et al., 2013), parts of Labrador-West Greenland (Chian et al., 1995), the Bay

of Biscay and the Western Pyrenees (Tugend et al., 2014a) and Flemish Cap-Goban Spur (Keen et al., 1989).

In contrast to a magma-poor rifted margin, a magma-rich rifted margin tends to display crustal thinning over a narrow area and is associated with large amounts of extrusive and intrusive magmatism (Fig. 2.2b). There are notable examples of magma-rich rifted margins around the world including the margins of the South Atlantic (Gladczenko et al., 1997) and those of the North Atlantic (Funck et al., 2017; Larsen and Saunders, 1998; Mutter et al., 1984).

Intermediate, between magma-poor and magma-rich margins, are 'normal' magmatic rifted margins. These rifted margins do not exhibit such extreme features as the end-member cases, i.e. exhumed mantle or over-thickened oceanic crust. Instead these margins may display smaller scale magmatic features, such as seaward dipping reflectors that are not as laterally or vertically extensive as seen on a classic magma-rich margin. They may show crustal thinning over an intermediate area rather than a very sharp or wide area. Realistically it is hard to state what features may or may not be present on a 'normal' magmatic margin due to the variability. These margins represent a large proportion of global rifted margins but are often under-represented within the literature, possibly due to misclassification as an end-member margin.

2.2.1 Ocean-continent transition structure of a magma-poor rifted margin

Offshore drilling, fossil analogues and a large number of seismic reflection and refraction studies have culminated in a good understanding of the evolution of a magma-poor rifted margin and the structure of the ocean-continent transition.

Conventionally, the evolution of a magma-poor margin starts with normal thickness continental crust that undergoes laterally extensive (>200 km) deformation resulting in intra-continental basins. Localisation of deformation within the underlying lithosphere starts the process of necking (Fig. 2.1). Deformation in continental crust then localises and the eventual coupling of crust and mantle results in the hyperextension of continental crust (Fig. 2.2a). Mantle is often exhumed due to a lack, or delay, of decompression melting and eventually, lithospheric breakup occurs allowing for the formation oceanic crust. On a magma-poor margin, the ocean-continent transition zone is usually composed of the hyper-extended and exhumed mantle domains with very little magmatism.

2.2.1.1 Hyper-extension at magma-poor rifted margins

Hyperextended continental crust is defined as continental crust that has been thinned to 10 km or less (Fig. 2.2a) (Brune et al., 2014; Doré and Lundin, 2015; Lundin and Doré, 2011; McIntosh et al., 2013; Pérez-Gussinyé, 2013; Tugend et al., 2014b) which requires β-factors in excess of 4. For hyper-extension to occur, coherent faults penetrate through the upper and lower crust and eventually the mantle in a process known as coupling (Decarlis et al., 2015; Lundin and Doré, 2011; Pérez-Gussinyé, 2013; Sutra and Manatschal, 2012). In order for continental crust to be hyper-extended, little to no magmatism is required. Evidence for hyper-extension can be seen globally in modern-day and fossilised margins; some examples are Iberia-Newfoundland, Southern Australia and the Alpine-Tethys (Gillard et al., 2016; Masini et al., 2013; Sutra and Manatschal, 2012).

2.2.1.2 Exhumed serpentinised mantle at magma-poor rifted margins

Eventually, the hyper-extension of continental crust reaches the point at which mantle is exhumed (Fig. 2.2a). Exhumation of the mantle has been documented in obducted rifted margins such as the Alpine-Tethys (Masini et al., 2013) and drilled offshore at margins such as Iberia-Newfoundland (Sibuet et al., 2007). In areas where hyper-extension has occurred, the presence of pervasive faults from the crust into the mantle leads to partial hydration of the uppermost mantle resulting in serpentinisation. Serpentinisation of the upper mantle decreases with depth, with the 100% serpentinisation occurring in the top 1.5-2.0 km below top basement, according to seismic refraction data (Cole et al., 2002; Skelton et al., 2005). The density of serpentinised mantle varies according to a number of factors, one of which is the percentage of magnetite present. The higher the concentration of magnetite the lower the average density, with 10% magnetite content resulting in a serpentinite surface density of 2575 kg m^{-3}. The absence of magnetite results in a much higher surface density of 2850 kg m^{-3} (Cole et al., 2002; Cooper, 2010; Cowie et al., 2015b).

2.2.1.3 Magmatism at magma-poor rifted margins

By definition, very little magmatism is seen along magma-poor rifted margins. If found at a magma-poor margin, magmatism commonly takes the form of dykes and sills within the area of hyper-extended continental crust (Franke, 2013). Melt can also infiltrate serpentinised mantle and be frozen in situ (Fletcher et al., 2009; Jeanniot et al., 2016); for example, in the Alps, serpentinised mantle is found to contain up to 12% volume MORB-type basalts (Müntener et al., 2010). Recognising either form of magmatism is difficult using seismic reflection profiles due to imaging and resolution problems, however if visible then

differentiating between both types of magmatism should be straightforward. Intrusions will only be seismically imaged if they are above the resolution capability of the seismic equipment and if they are sub-vertical or horizontal (Schofield et al., 2012). The intrusions believed to be situated at magma-poor margins are often small-scale, below the capability of seismic surveys, suggesting seismic observations are few and far in between. Melt infiltration would present a reduced velocity structure with no seismically visible Moho (Müntener et al., 2010).

2.2.2 Ocean-continent transition structure of a magma-rich rifted margin

In recent years, advances in technology mean that the deeper structure of magma-rich rifted margins is now imaged better than ever. Combined with drill hole data, potential field data and onshore analogues, our understanding of the formation of magma-rich rifted margins has improved.

In brief, a magma-rich rifted margin consists of normal thickness continental crust that thins and necks over a narrow region creating a sharp ocean-continent boundary. This is associated with large volumes of extrusive and intrusive magmatism, which eventually transitions into new oceanic crust. The ocean-continent transition of a magma-rich rifted margin generally consists of extrusive magmatism in the form of seaward dipping reflectors and large bodies of intrusive magmatism (Fig. 2.2b).

2.2.2.1 Extrusive magmatism at magma-rich rifted margins: seaward dipping reflector sequences

Seaward dipping reflectors (SDRs) are a feature commonly associated with the formation of magma-rich rifted margins and the onset of seafloor spreading. Briefly, they consist of a seaward-dipping wedge of stacked reflectors with arcuate reflection geometries that increase and thicken down-dip (Buck, 2017; McDermott et al., 2018; Paton et al., 2017). Over the years, many studies have attempted to unravel the composition and formation history of SDRs using seismic reflection and refraction studies, limited drill data and some onshore analogues. It is generally agreed that SDRs are magmatic features, a conclusion that has been reached based mainly on seismic velocity analysis and drill hole data (e.g. Buck, 2017; Hinz, 1981; Larsen and Jakobsdottir, 1988; Larsen and Saunders, 1998; Mutter et al., 1984). Here we give a brief review of SDR studies detailing their general structure, physical properties and formation interpretations.

The first recorded descriptions of SDRs come from Iceland, although not named as such at the time, and led to one of the main SDR formation models; the volcanic loading model (summarised by Buck, 2017). Walker (1959) described a large outcrop, ~4.5 km thick, in the Reydarfjördur area of tholeiites, olivine basalt and porphyritic basalt lava flows that had a uniform dip of 7° towards the centre of Iceland. Similar geology was noted in other areas of Iceland such as Berufjördur-Breidalur (Walker, 1960), leading to the general conclusion that these lava piles were formed via feeder dykes that contributed to overall extension and continental drift (Bodvarsson and Walker, 1964; Walker, 1981). A kinematic model to explain the formation of the Iceland SDRs was developed by Palmason (1973) and expanded on by Buck (2017), whereby lava flows, fed by dykes, stack together as a wedge. The eventual solidification and subsequent loading of the flows generates the isostatic readjustment of the underlying lithosphere, making it flex and bend, producing lava flows that dip towards the spreading centre.

The Northeast (NE) Atlantic contains some of the world's best studied magma-rich margins and SDR sequences. Breakup of Avalonia, Baltica and Laurentia during the Eocene in association with the North Atlantic Igneous Province led to the formation of magma-rich margins of the NE Atlantic including the Southeast (SE) Greenland, Hatton Bank and Faroes margins (Funck et al., 2017). Drilled SDR sequences on the SE Greenland margin (Larsen, 1994a) generally consist of 97% lava flows that have a ~20-30° dip, 2% volcaniclastics and 1% dykes. There is variation in lava flow composition, including olivine-basalt pahoehoe lavas, tuffs, hyaloclastites, intercalculated aphyric olivine-basalts and more evolved porphyritic basalts. Some SDRs showed red, oxidised flow tops suggesting subaerial formation. Compositional variations in Ni content suggest both continental lithosphere and depleted magma sources for the lava flows. On the Faroes margin, the SDR sequence analysed by White et al. (2008) has a maximum thickness of 7 km and extends for over ~100 km. The SDR sequence had an average velocity of ~5 km s^{-1}, but there is a decrease in seismic velocity (~4.2-4.5 km s^{-1}) at the base of the flows, interpreted as a combination of hyaloclastites and Palaeocene sediments. The Outer Vøring Plateau, offshore Norway, is part of the well-known Vøring magma-rich rifted margin formed over three rifting episodes with the final episode resulting in breakup at ~55 Ma (Eldholm et al., 1987). Large amounts of magmatism accompanied breakup, which was concentrated on the Vøring Plateau and in the Vøring Basin. The Outer Vøring Plateau contains sequences of SDRs that have been studied using drill holes, seismic reflection and seismic refraction data (e.g. Eldholm, 1972; Mjelde et al., 2005; Mutter et al., 1984; Skogseid and Eldholm, 1987; Viereck et al., 1988). Seismic velocity

analysis from Hinz (1981) demonstrated a varying velocity across the flows, with an average 3-4 km s^{-1} in the upper portion of the SDR wedge and an average of 5 km s^{-1} in the lower section of the wedge. Talwani et al. (1981) and Mutter et al. (1982) produced similar seismic velocities for the SDRs on the Outer Vøring Plateau, giving an average of 4.8 km s^{-1} for the entire SDR wedge with a total range of 2.6 km s^{-1} to 6.4 km s^{-1}.

In more recent years, studies have focused on the magma-rich margins of the South Atlantic, formed from the breakup of Gondwana during the Cretaceous alongside the formation of the Paraná-Etendeka Large Igneous Province (LIP) (Fromm et al., 2015; Gladczenko et al., 1997). The margins of southern Brazil, Argentina, Uruguay and Namibia all display large SDR sequences that in some cases exceed 10 km thickness and extend for hundreds of kilometres. Forward gravity modelling of the Argentinian SDRs gives a bulk density of 2750 kg m^{-3} interpreted as a combination of basalt and interstratified sediments (Paton et al., 2017) with seismic velocities varying from 4 km s^{-1} at the top to 6 km s^{-1} at the base (Hinz et al., 1999). The origin of the Argentinian SDR packages is two-fold. The first SDRs are emplaced subaerially over continental crust while the later SDRs form the upper layer of oceanic crust. Similar interpretations of two-stage SDR formation were made in the Pelotas Basin, offshore Brazil margin (McDermott et al., 2018). In the Pelotas Basin, an analysis of individual reflectors shows a range of dips from 0-28° and a range of reflector lengths of 1-91 km with an average length of 17.5 km across different types of packages. At the base of the SDRs in the Pelotas Basin, a marked increase in velocity was noted and attributed to the presence of feeder dykes but no evidence of dykes in the underlying basement was noted.

2.2.2.2 Intrusive magmatism at magma-rich rifted margins

Many studies on magma-rich margins have noted the presence of a high-velocity lower crustal body in association with extrusive magmatism such as SDRs (e.g. Cox, 1993; Gernigon et al., 2004; Holbrook et al., 2001; Mjelde et al., 2009, 2002; Reynisson and Ebbing, 2010; Thybo and Artemieva, 2013; White et al., 2008; White and McKenzie, 1989). Velocities often exceed 7 km s^{-1} for these bodies with some margins recording velocities of 7.9 km s^{-1}. On most seismic reflection profiles these bodies do not appear to have any internal structures, instead appearing as large masses at the base of crust. However, recent seismic studies (R. S. White et al., 2008) show that lower crustal bodies appear as sill intrusions in lower continental crust. The internal seismic visibility of lower crustal bodies could indicate how they formed, as McBride et al. (2004) suggest that lower crustal intrusions are only visible on seismic profiles when formed in pre-existing continental crust or older igneous crust due to

the contrasting densities. There is less of a contrast when formed alongside hotter crust giving the appearance of one large lower crustal body.

As lower crustal bodies remain deep within the crust, observations come from seismic reflection, seismic refraction and potential field data (e.g. Mjelde et al., 2009; White et al., 2008). Some additional evidence comes from petrological studies of erupted basalt sequences believed to originate from these bodies (Cox, 1993). Interpretations based on these datasets range from thick underplated magmatic material to heavily intruded continental crust.

The most popular interpretation of these lower crustal bodies is that they are thick piles of mafic magmatic material with a high magnesium content, ponded at the base of the crust due to buoyancy effects (Clerc et al., 2018; Cox, 1993; Gernigon et al., 2004, 2006; Mjelde et al., 2009; Mutter et al., 1984; White and McKenzie, 1989). This is known as magmatic underplating. Often, the decompression melting of large volumes of magma is explained using mantle plumes and small increases in mantle temperature (White and McKenzie, 1989), but other explanations exist, such as high extension rates, small-scale convection and fertile areas of mantle material.

More recently, evidence from seismic studies suggests high velocities in the lower crust are the result of large volumes of melt intruded into the crust as sills instead of thick piles of underplating (R. S. White et al., 2008). This interpretation lowers the total igneous thickness on a margin and therefore implies that melt production is controlled predominantly by mantle temperatures instead of small-scale convection or pockets of fertile mantle.

Chapter 3

Evaluating magmatic additions at a magma-poor rifted margin: An East Indian case study

This chapter comes from a manuscript published in Geophysical Journal International in January 2019. The authors of the manuscript are Caroline Harkin (first author), Nick Kusznir, Julie Tugend and Gianreto Manatschal. This study investigated the structure and formation of the supposed magma-poor East Indian margin by integrating seismic observations, quantitative techniques and plate kinematic history. Caroline Harkin carried out the quantitative analysis, while Julie Tugend and Gianreto Manatschal helped with the seismic interpretation. All authors contributed towards the interpretation and discussion of the results. All authors read and approved the manuscript prior to submission. The manuscript is accompanied by one supplementary figure, which has been provided at the end of the chapter.

Paper Abstract

Rifted margins are often classified as magma-poor or magma-rich based on a magmatic budget interpretation from seismic reflection data. The southern segment of the East Indian rifted margin is often regarded as a type-example of a magma-poor margin displaying exhumed mantle. However, in its southern segment, 9 km thick transitional crust, previously interpreted as magmatic crust, separates the exhumed mantle from thin oceanic crust. Such thick transitional crust is atypical for a magma-poor margin, so we investigate its likely formation and potential implications for the evolution of magma-poor margins. Using an integrated set of geophysical techniques alongside seismic reflection data, we test the existence of exhumed mantle and the composition of the transitional crust. These geophysical techniques consist of gravity inversion, residual depth anomaly (RDA) analysis, flexural subsidence analysis and joint inversion of gravity and seismic data. We apply these methods to high quality seismic reflection data (ION line INE1-1000) on the southern segment of the East Indian rifted margin and test a series of geological scenarios for the margin structure using our integrated quantitative analysis. Of these, our quantitative analysis, seismic observations and the regional plate kinematic history support a structure consisting of thinned continental crust inboard of exhumed, serpentinised mantle followed by thick (~9

km) magmatic crust transitioning into thin oceanic crust (~5 km). The juxtaposition of exhumed mantle and thick magmatic crust is explained by the occurrence of a jump in seafloor spreading during the Early Cretaceous formation of the southeast Indian Ocean. The final rifted margin structure contains characteristics of both magma-poor and magma-rich rifted margins resulting from two distinct rift events with different magmatic budgets. The investigation of the East Indian rifted margin structure and evolution shows the importance of incorporating the plate kinematic history and quantitative validation of seismic interpretation into the analysis. Classifying the East Indian margin as a typical magma-poor rifted margin is misleading causing us to question the use of end-member terminology to describe rifted margins.

3.1 Introduction

The classification of rifted margins commonly falls into two end-member types, magma-poor and magma-rich (e.g. Boillot et al., 1989; Franke, 2013; Geoffroy, 2005; Pickup et al., 1996; Reston, 2009; Reston and Manatschal, 2011), using an estimation of the volume of magmatic additions based on seismic interpretations with little to no quantitative assessment. Resolving the magmatic budget based on seismic reflection observations can be ambiguous, leading to several potential interpretations of the magmatic volume (Tugend et al., 2018), with different implications for rifted margin formation processes. By definition, a magma-poor rifted margin is characterised by relatively small amounts of magmatic additions. In some cases, this leads to the rupture and separation of continental crust and consequent mantle exhumation before the onset of decompression melting and seafloor spreading. The delay in the onset of decompression melting, with respect to crustal rupture, may be due to depleted or cool mantle or slow spreading rates (Doré and Lundin, 2015; Fletcher et al., 2009; Lundin and Doré, 2011; Pérez-Gussinyé, 2013). Alternatively, there may be an initial retention of melt (Lizarralde et al., 2004) until a critical melt threshold is exceeded. The formation processes of magma-poor rifted margins and mantle exhumation have been extensively investigated on the Iberian margin by deep-sea drilling and seismology. During the development of these rifted margins, once continental crust is thinned to less than 10 km the entire crust becomes embrittled and is termed ‘hyper-extended’ (Pérez-Gussinyé et al., 2006; Reston, 2009; Sawyer et al., 2007; Sutra et al., 2013; Tugend et al., 2015). Embrittlement of the crust allows for faults to penetrate into the underlying mantle, transporting fluids and leading to the serpentinisation of the mantle underneath hyper-extended crust (Doré and Lundin, 2015; Gillard et al., 2016; Pérez-Gussinyé, 2013; Reston, 2009; Tucholke et al., 2008). Seismic velocities for exhumed, serpentinised mantle range from 5 km s^{-1} to 8 km s^{-1} (Reston,

2009) with depth-dependent densities ranging from 2650 kg m^{-3} to 2850 kg m^{-3} at the surface, to 3000 kg m^{-3} at depth, depending on the amount of magnetite present (Cooper, 2010). The transition between exhumed mantle and first oceanic crust is believed to occur when the rise of the asthenosphere is enough to generate decompression melting that initiates seafloor spreading (Tucholke et al., 2007) with average oceanic crust that has a thickness of 7 km (White et al., 1992) and an average basement density of 2860 kg m^{-3} (Carlson and Herrick, 1990).

The East Indian rifted margin (Fig. 3.1) has previously been classified as magma-poor following seismic interpretations of high quality seismic reflection data, such as seismic line INE1-1000 (Fig. 3.2) and others from ION Geophysical, that deduce the presence of hyper-extended continental crust and exhumed mantle (Haupert et al., 2016; Nemčok et al., 2013; Pindell et al., 2014; Sinha et al., 2015; Tugend et al., 2018). In addition, these seismic interpretations show a ~9 km thick transitional crust separating exhumed mantle and thin oceanic crust. The juxtaposition of mantle exhumation, thick transitional crust and thin oceanic crust poses an interesting question for the evolution of a supposedly typical magma-poor rifted margin during breakup, the initiation of decompression melting and the extraction of that melt to form oceanic crust. In order to investigate this enigma, we carry out validations of these previous interpretations.

We test the presence of exhumed mantle and investigate the composition of the transitional crust using a set of quantitative methods, gravity inversion, residual depth anomaly analysis, subsidence analysis and joint inversion of gravity and seismic data. We also provide and examine alternative geological interpretations based on seismic observations and quantitative analyses with the aim of better understanding the tectonic and magmatic structures present at rifted margins and the magma-poor versus magma-rich classification of rifted margins.

3.1.1 Geological background

3.1.1.1 Formation of the East Indian rifted margin

The East Indian rifted margin formed as a result of a polyphase breakup between India and Antarctica (Chand et al., 2001; Frey et al., 2000; Gaina et al., 2003, 2007; Gibbons et al., 2013; Lal et al., 2009; Radhakrishna et al., 2012; Ramana et al., 1994, 2001; Sinha et al., 2015) and now consists of a series of segmented basins which from north to south are; Bengal Basin, Mahanadi Basin, Krishna-Godavari Basin and the Cauvery Basin (Lal et al., 2009)(Fig. 3.1a). The complex evolution of extensional deformation related to breakup and the formation of

the East Indian rifted margin, is associated with the creation of a microcontinent, Elan Bank. This microcontinent currently lies in the Enderby Basin, the conjugate to the East Indian margin, as part of the Kerguelen Plateau (Borissova et al., 2003; Gaina et al., 2003, 2007; Ingle et al., 2002a; Müller et al., 2001; Nicolaysen et al., 2001; Sinha et al., 2015). Geochemical, petrological, seismic and potential field evidence suggest Elan Bank was situated adjacent to East India within the Krishna-Godavari Basin prior to lithospheric breakup (Borissova et al., 2003; Charvis et al., 1995; Charvis and Operto, 1999; Frey et al., 2000; Gaina et al., 2003, 2007; Ingle et al., 2002a; Nicolaysen et al., 2001).

In this study we refer to lithospheric breakup as the point where sea floor spreading has initiated after the separation of continental crust and the rise of the underlying lithosphere (Soares et al., 2012).

Due to the polyphase and complex nature of breakup along the East Indian rifted margin, it has been suggested that lithospheric breakup between India, Elan Bank and Antarctica occurred in two stages separated by an ocean ridge jump. Initially, seafloor spreading occurred between India/Elan Bank and Antarctica. The age of lithospheric breakup and seafloor spreading is debated, with ages based on both magnetic anomaly evidence and plate reconstructions. Magnetic anomaly M11, present in Enderby Basin (Ramana et al., 2001), implies that seafloor spreading was active at 134 Ma. However, Sinha et al. (2015) used plate reconstructions to suggest that the breakup between India/Elan Bank and Antarctica occurred at 132 Ma. Other magnetic anomalies found in the Enderby Basin M9o to M2o suggest seafloor spreading between India/Elan Bank and Antarctica occurred from 130.2 Ma to 124.1 Ma (Gaina et al., 2007).

An ocean ridge jump northwards, to between India and Elan Bank, then leads to a second stage of rifting with a proposed lithospheric breakup age ranging between 124 Ma to 120 Ma. Evidence for an ocean ridge jump comes from south of Elan Bank, where magnetic lineations in oceanic crust show a fossilised spreading centre that became extinct after the formation of magnetic anomaly M2 at 124 Ma (Borissova et al., 2003; Gaina et al., 2007; Müller et al., 2001). Apart from limited magnetic lineations, there is little geophysical evidence for the age of breakup, however some studies use plate reconstructions to show breakup occurred at ~120 Ma (Müller et al., 2000; Royer and Coffin, 1988).

Around the time of lithospheric breakup between India and Elan Bank, magmatic events in the Bay of Bengal, produced large volumes of extrusive material (Coffin et al., 2002; Frey et al., 2000; Ingle et al., 2002b; Olierook et al., 2016). These events were associated with

asthenosphere temperature anomalies linked to the Kerguelen plume, occurring as early as 137 Ma through to the present day (Olierook et al., 2016).

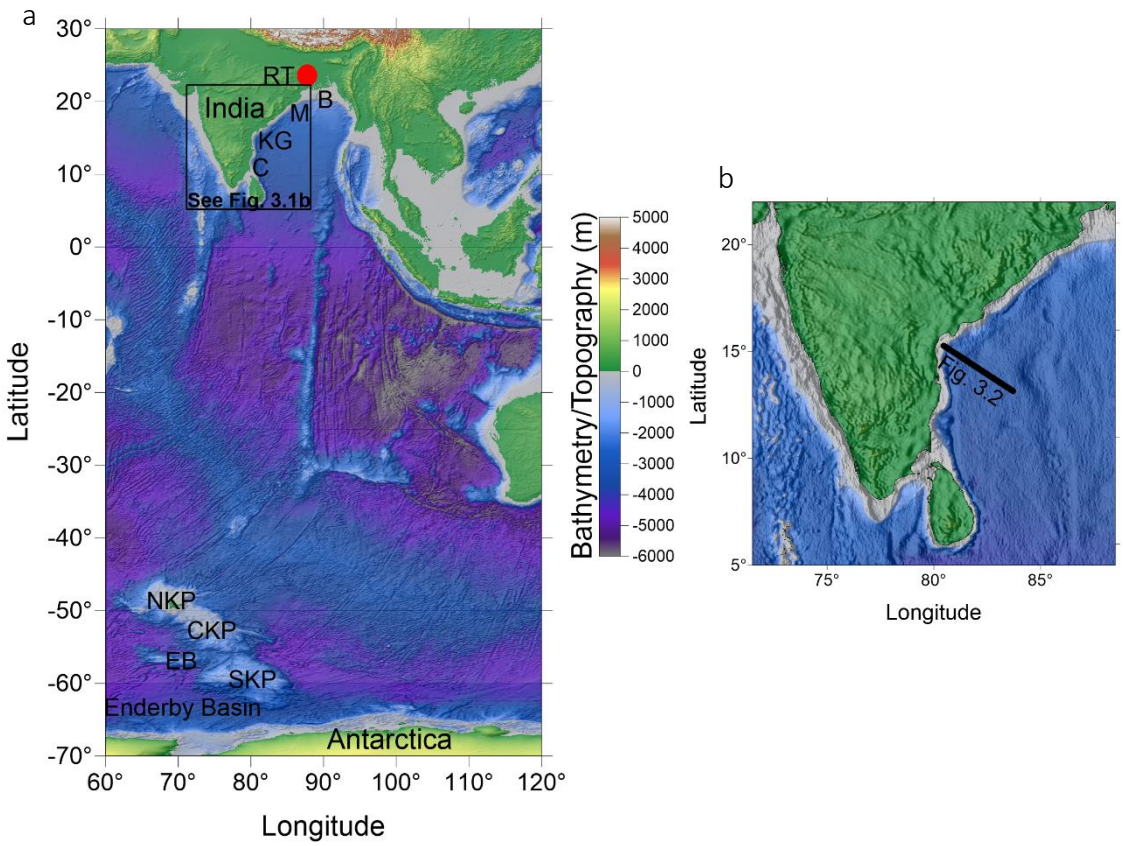

Fig. 3.1. a) Bathymetry/topography map of India, Antarctica and the Indian Ocean (Smith and Sandwell, 1997) with an overlay of free-air gravity anomaly shaded relief (Sandwell and Smith, 2009); B, Bengal Basin; C, Cauvery Basin; CKP, Central Kerguelen Plateau; EB, Elan Bank; KG, Krishna-Godavari Basin; M, Mahanadi Basin; NKP, North Kerguelen Plateau; RT, Rajmahal Traps; SKP, South Kerguelen Plateau. b) Enlargement of box shown in (a) with location of seismic profile shown in Fig. 3.2.

3.1.1.2 Previous work on INE1-1000

Previous studies have analysed seismic reflection data on the East Indian rifted margin (Fig. 3.1b) including ION line INE1-1000 (Fig. 3.2), which is the focus of this paper. These studies give interpretations of the regional tectonic history based predominantly on seismic data, with the addition of other methods such as forward gravity modelling (Nemčok et al., 2013).

Nemčok et al. (2013) discussed the presence of exhumed mantle along the East Indian rifted margin, with a thin layer of volcanic cover that was unroofed from beneath the proximal continental crust along certain segments of the margin. In particular, on seismic line INE1-1000, the exhumed mantle was shown to be adjacent to an area of thick crust (~9 km) defined as the proto-oceanic corridor that varies in thickness from 4.2 km to 11.2 km before terminating to form oceanic crust with an average thickness of 5.4 km. Proto-oceanic crust is

here defined as magmatic crust that does not yet display all the properties and characteristics of normal oceanic crust. Nemčok et al. (2013) used gravity forward modelling with densities for the proto-oceanic crust varying between 2.99 and 3.13 g cm^{-3} representing a combination of seaward dipping reflectors, exhumed mantle and continental fragments resulting from disorganised seafloor spreading. Sinha et al. (2015) is in agreement with Nemčok et al. (2013) with the interpretation of exhumed mantle and thick crust as part of a proto-oceanic corridor using adjacent seismic profiles. However, they focus on the formation of Elan Bank as a microcontinent, stating the margin of Elan Bank also contains proto-oceanic crust that matches in seismic reflectivity to the East Indian margin. Pindell et al. (2014) also interpreted the presence of serpentinised mantle on INE1-1000, but suggested it is in direct contact with sediments/continental crust stratigraphically above, rather than volcanics, with the outboard thick crust being termed oceanic crust, but with the same properties as the proto-oceanic crust described by Nemčok et al. (2013) and Sinha et al. (2015). Haupert et al. (2016) focused on the continental thinning and mantle exhumation of INE1-1000 showing a series of continental faults that accommodate thinning over a distance of 90 km. They show a top basement surface that lies above a narrow band of parallel reflectivity on top of exhumed mantle. A breakup point is defined at the distal edge of the exhumed mantle, at the onset of thick crust, which is considered to be part of the oceanic domain.

3.1.2 Seismic observations

Seismic reflection ION line INE1-1000 is situated on the East Indian rifted margin (Fig. 3.1b) as part of the IndiaSPAN survey from ION Geophysical. Both pre-stacked time and depth migrated seismic reflection profiles (Fig. 3.2) were interpreted and analysed with each reaching 16 s TWTT and 25 km respectively.

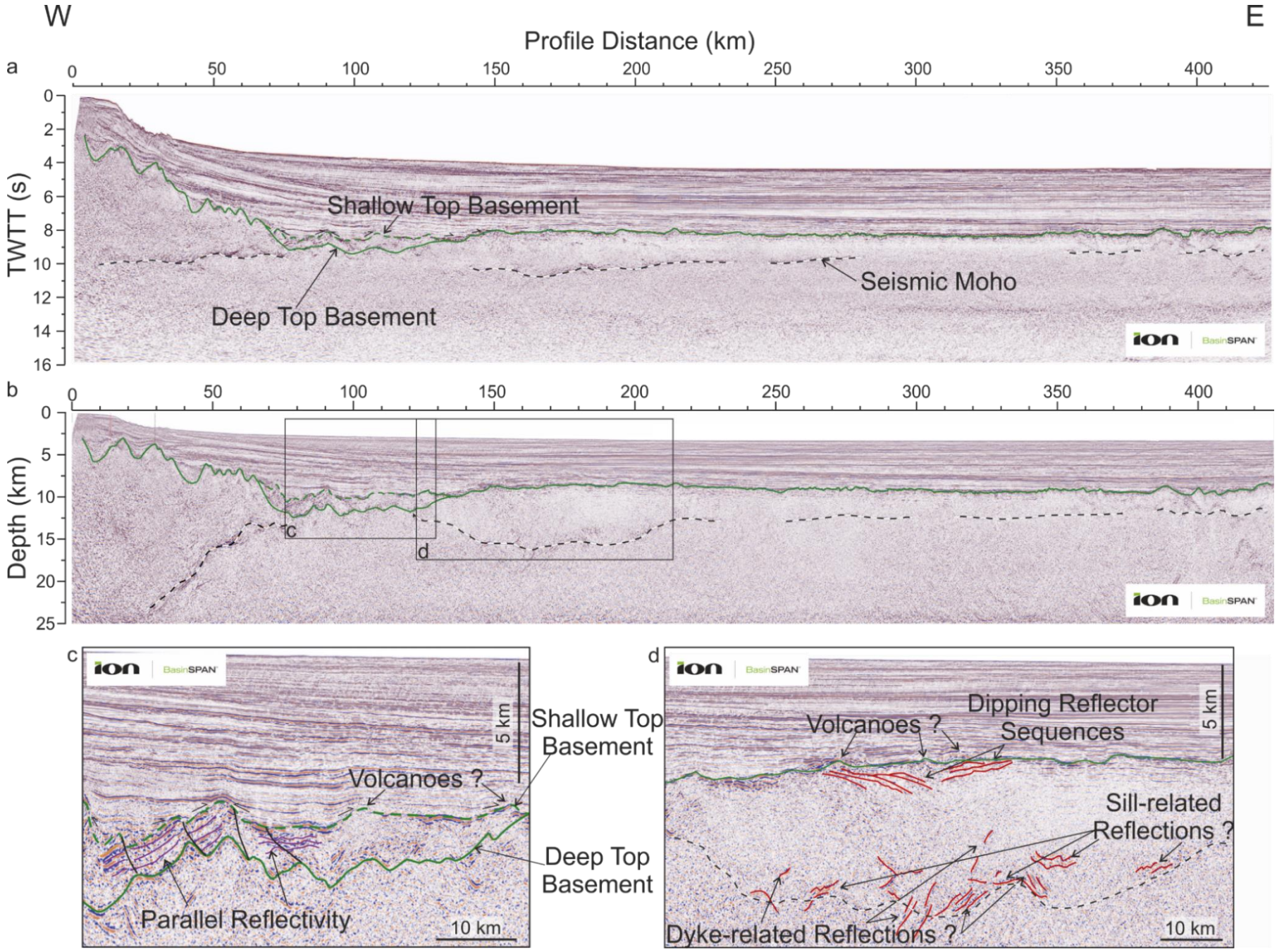
W
E
Profile Distance (km)
a
TWTT (s)
Shallow Top Basement
Deep Top Basement
Seismic Moho
b
Depth (km)
c
d
Volcanoes ?
Shallow Top Basement
Deep Top Basement
Parallel Reflectivity
5 km
10 km
Dipping Reflector Sequences
Sill-related Reflections ?
Dyke-related Reflections ?

Fig. 3.2. Seismic observations of INE1-1000, location shown by Fig. 3.1b. a) Pre-stacked time migrated (PSTM) seismic reflection profile showing top basement surfaces (shallow top basement, dashed green and deep top basement, solid green) and seismic Moho (dashed white and black). b) Pre-stacked depth migrated (PSDM) seismic reflection profile showing top basement surfaces (shallow top basement, dashed green and deep top basement, solid green) and seismic Moho (dashed white and black). c) Enlargement of box in b) showing two top basement surfaces over region of presumed exhumed mantle. Parallel reflectivity between the two surfaces is highlighted. d) Enlargement of box in b) showing area of thick crust. Volcanic and magmatic features are highlighted, e.g. intrusions, submarine volcanoes and dipping reflector sequences. Within the central region of the thick crust, there is a lack of any clear internal reflections.

Here we use first order seismic observations to define the position of seismic interfaces such as top basement and seismic Moho. Our interpretation of this line follows a methodology similar to that presented in Tugend et al. (2018). Top basement is defined as the base of passive infill or the base of syn-rift sediments, and the top of crystalline basement/pre-rift sediments. We define seismic Moho as the deepest continuous visible reflector, which we assume corresponds to the base of the petrological crust, using Warner (1987) as a guide within the time domain to constrain our Moho picks to within 10 ± 1 s TWTT. In addition to identifying seismic interfaces, we investigate the internal seismicity of the proposed basement. We categorise seismic reflections as magmatic intrusions based on work done by Magee et al. (2015, 2018), Schofield et al. (2012) and Planke et al. (2005).

The top basement surface can be traced throughout the seismic reflection profile. Over the proximal domain from a line-distance of 0-7 km, top basement deepens by ~7 km, cut by a series of seaward dipping faults. From a line-distance of 75 km to 120 km, there are two candidates for top basement. The first possible top basement surface lies at a depth of 8.5-10 km at the base of passive infill, characterised by onlap and downlap geometries of the overlying sediments, similar to the top basement surface presented in Haupert et al. (2016), Nemčok et al. (2013) and Pindell et al. (2014) (shallow top basement surface, Fig. 3.2). The second possible top basement surface is situated at the base of a reflective package stratigraphically below the passive infill at a depth of ~12 km similar to the top basement shown by Tugend et al. (2018) (deep top basement surface, Fig. 3.2). Within the package, reflectivity shows sub-parallel layers that are offset from one another periodically and that downlap onto the base of the package (Fig. 3.2c). Depending on the nature of underlying basement, the parallel-bedded reflectors are either pre-rift sediments formed on existing continental crust, or they are post-rift sediments deposited on newly formed basement (i.e. exhumed mantle or magmatic basement) that have been faulted in a later rift event. From a line-distance of 120 km to 220 km, top basement depth shallows to ~7.5 km where reflectors

that are largely continuous form the surface. These reflectors are interrupted by volcanoes that extend into the overlying, onlapping sediments (Fig. 3.2d). From a line-distance of 220 km to 380 km, top basement is parallel to bathymetry with little to no topography and is represented by a series of short, discontinuous reflectors. At the end of the profile, from line-distance 380 km onwards, top basement topography forms dome-like structures. From these first order observations, there are two possible top basement interfaces that will be tested in this study, which vary in depth between line-distances of 75 km and 120 km (Fig. 3.2c).

Seismic Moho from a line-distance of 0 km to 75 km shows a continuous reflector that shallows rapidly, merging with the base of the parallel-bedded reflective package at a line-distance of 75 km. Between line-distances 75 km and 120 km, there is no visible seismic Moho, possibly suggesting the presence of serpentinised mantle. The deepest reflector here is the base of the reflective package at ~12 km. Seismic Moho is once again visible from a line-distance of ~120 km, at a depth of ~16 km where it forms a succession of discontinuous reflectors. From a line-distance of 200 km to 220 km seismic Moho begins to shallow once more to ~12 km and from line-distance 220 km to the end of the profile it remains sub-parallel to the top basement surface. It should be noted that the seismic Moho is more visible on the PSTM seismic section (Fig. 3.2a).

Between a line-distance of 120 km and 220 km, the crust is ~9 km thick and is the thick crustal area under investigation. In the lower section of the basement, defined as crystalline material, there is seismic evidence for a number of intrusions (Fig. 3.2d), including step geometries that are indicative of sill complexes and sub-vertical dyke-related reflections (Magee et al., 2015, 2018). In the top portion of the crust, dipping reflector sequences that dip both seawards and landwards can be seen (Fig. 3.2d), features commonly associated with volcanic activity.

3.2 Methods

The methods presented here provide a range of results that together give a robust and comprehensive view of the margin. The gravity inversion determines Moho depth, crustal thickness and lithosphere thinning while the residual depth anomaly analysis can estimate the extent of continental crust. Subsidence analysis gives lithosphere thinning independent of the gravity inversion and the joint inversion of seismic and gravity data is able to investigate basement heterogeneities.

3.2.1 Gravity anomaly inversion

Depth to the Moho, crustal thickness and lithosphere thinning have been calculated using the gravity anomaly inversion (Alvey et al., 2008; Chappell and Kusznir, 2008a; Cowie et al., 2015b; Greenhalgh and Kusznir, 2007; Roberts et al., 2013). We use bathymetry data from Smith and Sandwell (1997) alongside satellite-derived free-air gravity from Sandwell and Smith (2009). Ocean age isochrons are taken from Müller et al. (2008) and 2D sediment thickness is calculated from pre-stacked depth-migrated seismic reflection data on the East Indian rifted margin.

We perform the inversion in the 3D spectral domain to give 3D Moho geometry using the method of Parker (1972) and invoking Smith's theorem (Smith, 1961) to provide a unique solution for the assumptions made. We use a constant crustal density of 2850 kg m^{-3} (averaged from: Carlson and Herrick, 1990; Christensen and Mooney, 1995). Continental rifted margins and oceanic lithosphere have an elevated geotherm (Chappell and Kusznir, 2008a), which results in a large negative mass deficiency and lithosphere thermal gravity anomaly. Our gravity inversion incorporates a correction for this lithosphere thermal gravity anomaly; without this correction Moho depth would be over-estimated.

The lithosphere thermal anomaly correction is determined from present-day lithosphere temperatures calculated using a 3D lithosphere thermal model. Cooling times for oceanic lithosphere are derived from ocean isochrons, while cooling time for rifted continental margin lithosphere uses the breakup age (Chappell and Kusznir, 2008a). The initial thermal perturbation of rifted continental margin lithosphere is derived from the lithosphere thinning factor, γ, calculated in the gravity inversion. For oceanic lithosphere γ = 1.0. The lithosphere thinning factor, γ, is defined as $\gamma = 1 - 1/\beta$, where β is the lithosphere stretching factor (McKenzie, 1978). For rifted margin lithosphere, β is determined from the ratio of initial continental crustal thickness to present-day continental crustal thickness. Lithosphere thinning and crustal thinning are taken to be equivalent assuming depth-uniform stretching and thinning (Chappell and Kusznir, 2008a; Kusznir et al., 2018).

We investigate the sensitivity to breakup age using rounded values of 130 Ma and 120 Ma, which correspond to the breakup ages of the two rift phases discussed earlier. Due to the uncertainty in the breakup ages for each rift phase, we also investigate breakup ages of 135 Ma and 115 Ma. Tests show that the depth to the Moho produced by the gravity inversion (Fig. 3.3a) is not significantly dependent on the breakup age.

3.2.1.1 Reference Moho depth calibration

The calculation of Moho depth from gravity inversion requires a reference Moho depth. Reference Moho depth is dependent on the long wavelength gravity field which is controlled by deep mantle processes which vary globally, not by crustal or lithosphere density structure. It is important that this reference Moho depth is calibrated. In the absence of seismic refraction data, we have calibrated the reference Moho depth against the seismic oceanic Moho. We use a reference Moho depth of 35 km in the gravity inversion which gives Moho depths which, when taken into the time domain, closely match the seismic Moho visible oceanward on the TWTT seismic section (Fig. 3.2 and Fig. 3.3b).

3.2.1.2 Sensitivity to magmatic addition

During rifting, magmatic material resulting from decompression melting may be added to the crust in the form of extrusives and intrusives. Determining the remaining thickness of continental crustal basement at rifted margins is required in order to locate the distal limit of continental crust and to calculate the lithosphere thinning factor from the gravity inversion. Furthermore, the amount of magmatic addition and the timing of its initiation with respect to breakup is highly variable at rifted margins, as testified by the differences between magma-poor and magma-rich rifted margins. While the gravity inversion gives the total thickness of crustal basement, it cannot alone distinguish continental basement from new magmatic material, which eventually forms oceanic crust.

Within the gravity inversion we regard the degree of decompression melting (e.g. magma-poor, 'normal', magma-rich) as an *a priori* assumption and test for each end-member scenario. The thickness of magmatic addition is determined from lithosphere thinning factor using a parameterisation of the decompression melting models of McKenzie & Bickle (1988) and White & McKenzie (1989). This parameterisation is discussed in more detail in Chappell & Kusznir (2008).

Figure 3.3c shows the lithosphere thinning factor profiles determined from gravity inversion for a range of decompression melt parameterisations, spanning magma-poor to magma-rich. The corresponding crustal cross sections are shown in Figure 3.3d where we see the various partitioning of crustal basement into remnant continental crust and new magmatic crust depending on the melt parameterisation used. Note that for the crustal cross sections, the entire volume of magmatic addition is added as underplated material. In reality, the magmatic addition would be a combination of intrusive and extrusive material. In Figures 3.3c and 3.3d we examine three different parameterisations of decompression melting; (i)

'normal' magmatic, (ii) magma-poor and (iii) magma-rich. The associated critical thinning factors for the onset of decompression melting and maximum magmatic addition (final oceanic crust thickness) are summarised in Table 3.1. For magma-rich margins decompression melting occurs at a lower thinning factor (γ=0.5) and produces a larger thickness of melt (10 km) due to elevated mantle temperatures, while at 'normal' margins a lower mantle temperature means more thinning is required to initiate decompression melting and less melt is produced (White & McKenzie, 1989). Although decompression melting is predicted to start at γ=0.7 for magma-poor margins, melt is suppressed to represent an extreme end-member scenario. An additional parameterisation appropriate to serpentinised mantle is also shown in Figures 3.3c and 3.3d to test for the presence of serpentinised mantle. Within this parameterisation, the mass deficiency of serpentinised mantle with respect to normal mantle is equivalent to 3.1 km of basement material with a density of 2850 kg m^{-3}. This means that if the gravity inversion predicts basement with a thickness of ~3 km when using the serpentinised mantle parameterisation then serpentinised mantle can exist (see Cowie et al., (2015) for greater detail).

Margin Type	Critical Thinning Factor (γ)	Max. Oceanic Crustal Thickness (km)
'Normal' Magmatic	0.7	7.0
Magma-Poor	0.7	0.0
Magma-Rich	0.5	10.0
Serpentinised Mantle	0.7	3.1

Table 3.1 - Rifted margin end-member gravity inversion parameters taken from Chappell & Kusznir (2008) and Cowie et al. (2015)

None of the lithosphere thinning factor profiles and crustal cross section shown in Figures 3.3c and 3.3d are geologically plausible or applicable across the whole profile, because the parameterisation of decompression melt for each end-member scenario does not apply across the whole section, implying the margin is not a typical end-member margin or a 'normal' margin. However, each parameterisation is applicable for part of the section. We identify where the parameterisations may be applicable and where they are not. For example, Fig. 3.3di displays the solution for 'normal' magmatic parameterisation which in the proximal domain suggests the presence of magmatic basement that is ~7 km thick. Magmatic basement would likely produce an impedance contrast with the underlying mantle, i.e. a seismic Moho, which is not visible on seismic reflection images making this solution not realistic in the proximal domain.

Decompression melt solutions for a top basement pick at the base of passive infill (shallow top basement) have also been calculated (see supplementary information).

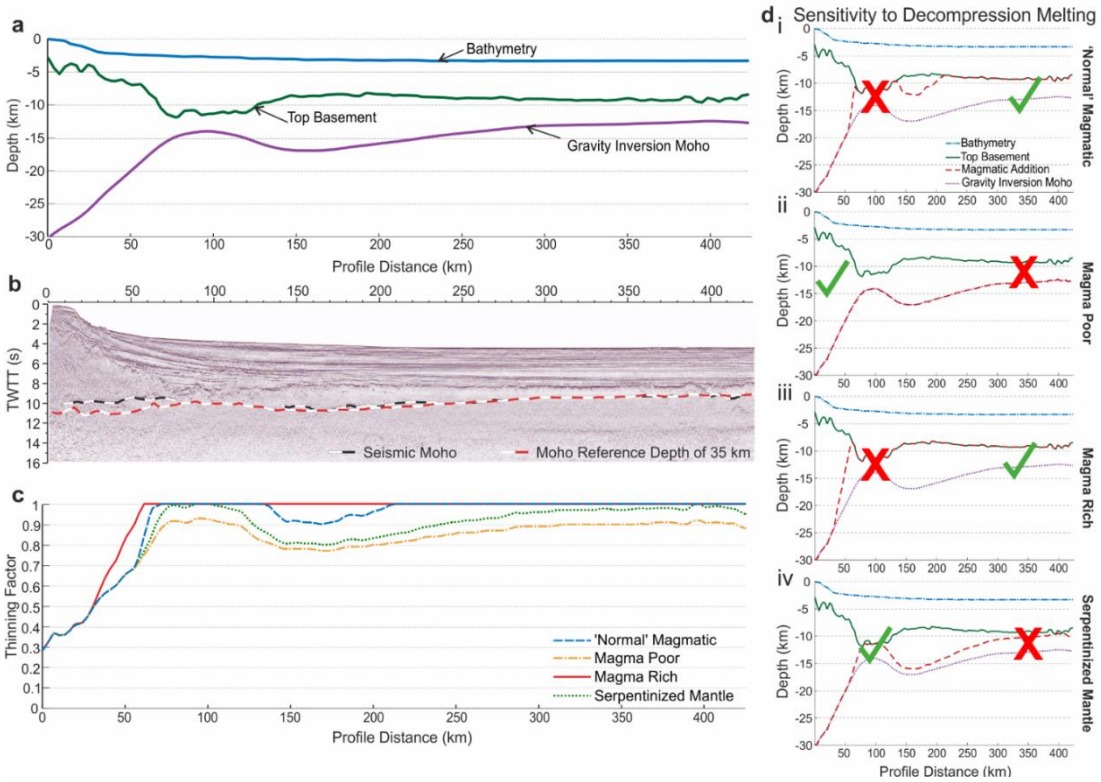

Fig. 3.3 Gravity anomaly inversion results, calibration and parameterisations of decompression melting. a) INE1-1000 crustal cross section without a decompression melting parameterisation. It shows bathymetry, deep top basement and the gravity inversion Moho. When decompression melt parameterisations are included, the depth to the gravity inversion Moho remains robust. b) Comparison of observed seismic Moho and a Moho reference depth of 35 km, for calibration of Moho reference depth. c) Lithosphere thinning factors generated for each melting parameterisation listed in d) and Table 3.1. d) Cross section profiles of INE1-1000 for each decompression melting scenario; i) 'normal' magmatic, ii) magma-poor, iii) magma-rich and iv) serpentinised mantle. Ticks indicate areas that match seismic observations, crosses indicate areas that do not match with seismic observations.

3.2.2 Residual depth anomaly analysis

The residual depth anomaly (RDA) analysis identifies anomalous bathymetries compared against expected bathymetric anomalies, as calculated from thermal plate model predictions from Crosby & McKenzie (2009). In order to calculate the RDA, the difference between the observed bathymetry (b_{obs}, Fig. 3.4a) and predicted bathymetry (b_{pre}, Fig. 3.4a) is taken.

$$RDA = b_{obs} - b_{pre} \quad (2)$$

Sensitivities to alternative thermal plate model predictions of b_{pre} have been discussed in Cowie et al., (2015) and are shown to have little variation.

The use of sediment corrected bathymetry in the calculation of the RDA is important as it removes the effect of sediment loading on the basement. The sediment corrected bathymetry was calculated using flexural backstripping (Kusznir et al., 1995) and sediment decompaction assuming shaly-sand compaction parameters (Sclater and Christie, 1980).

A negative RDA, whether it is a raw RDA or sediment corrected RDA, is indicative of crust thinner than the global average of 7 km (White et al., 1992). A positive RDA indicates that the crust is thicker than the global average of 7 km.

We also compare the RDA component from crustal basement thickness variations (RDA_{CT}) (Cowie et al., 2015b) (Fig. 3.4b). By observing the difference between the sediment corrected RDA and the RDA_{CT}, the effect of present-day mantle dynamic topography can be quantified, where a positive difference is representative of mantle dynamic uplift and a negative difference implies mantle dynamic subsidence. Present-day mantle dynamic topography is not necessarily representative of dynamic topography during margin formation but could be indicative of remnant mantle topography if a large thermal anomaly was present and has slowly dissipated over time.

3.2.2.1 Sensitivity to breakup age

As a result of the complex, polyphase breakup between India/Elan Bank and Antarctica the age of lithospheric breakup is uncertain. Müller (2008) gives global ocean age isochrons based on magnetic anomalies but due to the uncertainty in magnetic anomalies dating it is necessary to consider alternate breakup ages that fit within the uncertainty estimates. Therefore, the sensitivity to lithospheric breakup ages of 115 Ma, 120 Ma, 130 Ma and 135 Ma (as used in the gravity inversion), in addition to Müller isochrons were calculated and are shown in Figure 3.4c. There is little variation between results, so no preferred lithospheric breakup age can be identified. We use Müller isochrons (Müller et al., 2008) in our RDA calculations as there is no notable difference.

3.2.2.2 Sensitivity to effective elastic thickness

Sensitivity to effective elastic thickness (T_e) was investigated using T_e values of 0.01, 1.0, 3.0 and 5.0 km. T_e controls the flexural strength of the lithosphere that depends on many factors (Kusznir & Karner, 1985). T_e can vary from margin to margin and often lies in the range of 1.5 to 5 km (Roberts et al. 1998). Our results show some variation (Fig. 3.4d) but it is not significant in changing the overall result. A T_e of 3.0 km was used to calculate the sediment

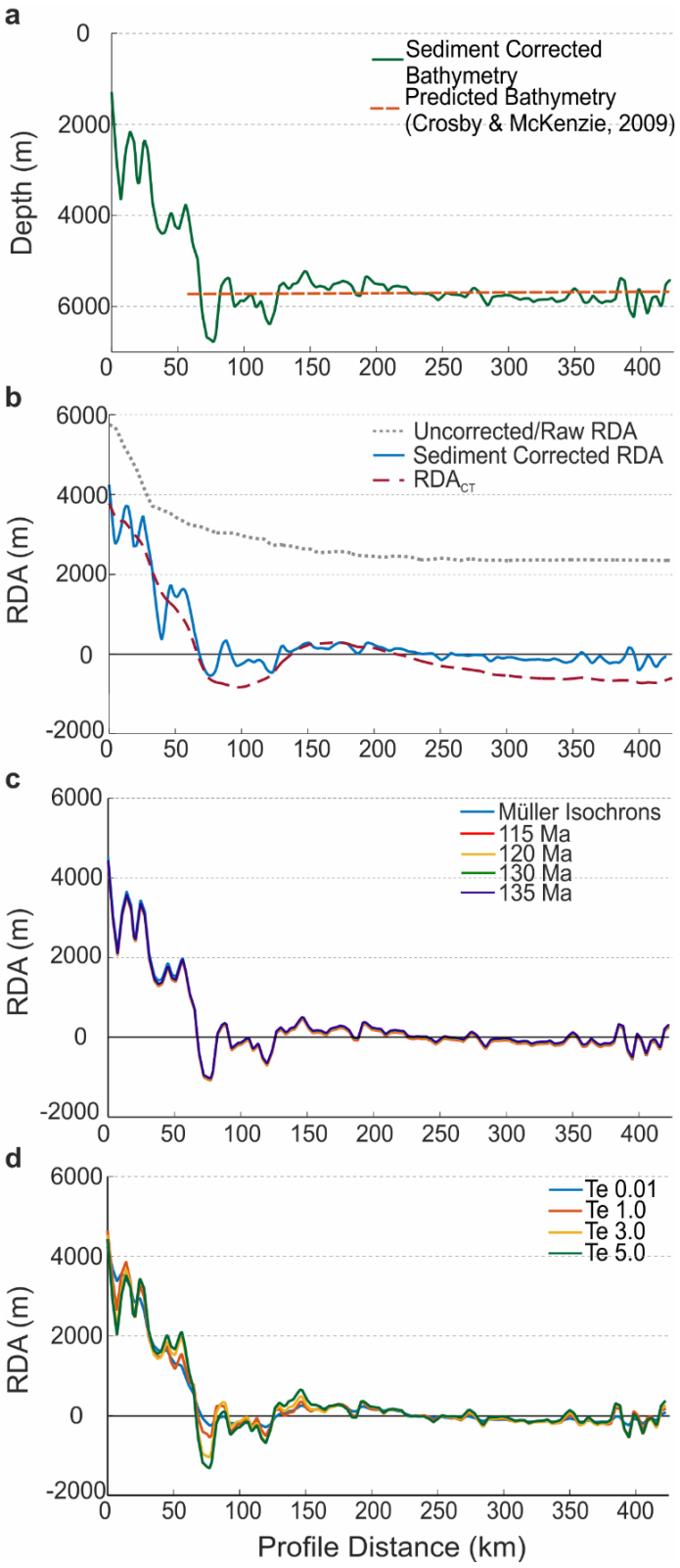

Fig. 3.4. Residual depth anomaly analysis. a) Cross-section showing sediment-corrected bathymetry and the predicted bathymetry from Crosby & McKenzie, 2009. b) RDA results for uncorrected RDA (black), sediment corrected RDA (blue) and crustal basement thickness variation component RDA (red) using deep top basement surface. c) Age sensitivity test for ION line INE1-1000 using Müller isochrons and constant breakup ages of 115 Ma, 120 Ma, 130 Ma and 135 Ma. d) Effective elastic thickness (T_e) sensitivity test for ION line INE1-1000 using T_e of 0.01, 1, 3 and 5 km.

corrected bathymetry and subsequent RDA results which is equivalent to a flexural rigidity of ~$1.7x10^{20}$ N m, representative of basement rocks (Roberts et al., 1998).

3.2.3 Subsidence analysis

Lithosphere thinning factors can also be calculated using subsidence analysis and are independent to those determined from gravity inversion. Flexural backstripping and decompaction assuming shaly-sand parameters (Sclater and Christie, 1980), removes sedimentary layers and loading to the top of the pre-rift sequence and top of oceanic crust, giving a sediment corrected bathymetry, not an estimate of palaeobathymetry. Sediment corrected bathymetry approximates water-loaded subsidence if the top of the pre-rift sequence is assumed to have been at sea level prior to rifting. Water-loaded subsidence is assumed to be a combination of initial (S_i) and thermal subsidence (S_t) (McKenzie, 1978). We convert water-loaded subsidence into thinning factors with the inclusion of a correction for the addition of new magmatic material from decompression melting using a parameterisation melt model of White and McKenzie (1989). Magmatic addition results in thicker crust that isostatically reduces the initial subsidence. For the same water-loaded subsidence, the subsidence analysis therefore gives a higher thinning factor. We parameterise decompression melting using the same method as in the gravity inversion (section 3.1.1 and Fig. 3.3d). An example of the relationship between water-loaded subsidence and thinning factor is shown in Figure 3.5a for 'normal' decompression melting which produces 7 km thick oceanic crust. As with the gravity inversion, depth-uniform thinning is assumed. The methodology is described in greater detail in Roberts et al. (2013) and Cowie et al. (2015).

The lithosphere thinning factor profiles produced by subsidence analysis assuming magma-rich, 'normal' and serpentinised mantle are shown in Figure 3.5b. The lithosphere thinning factor can be used to establish the oceanward boundary of continental crust and therefore the location of the continent-ocean boundary defined here as the transition between continental and oceanic crust. A thinning factor of 1.0 suggests complete thinning of continental crust to the point where no continental crust remains while a low thinning factor

of 0.0 suggests no thinning has taken place and the thickness of the continental crust is the initial amount.

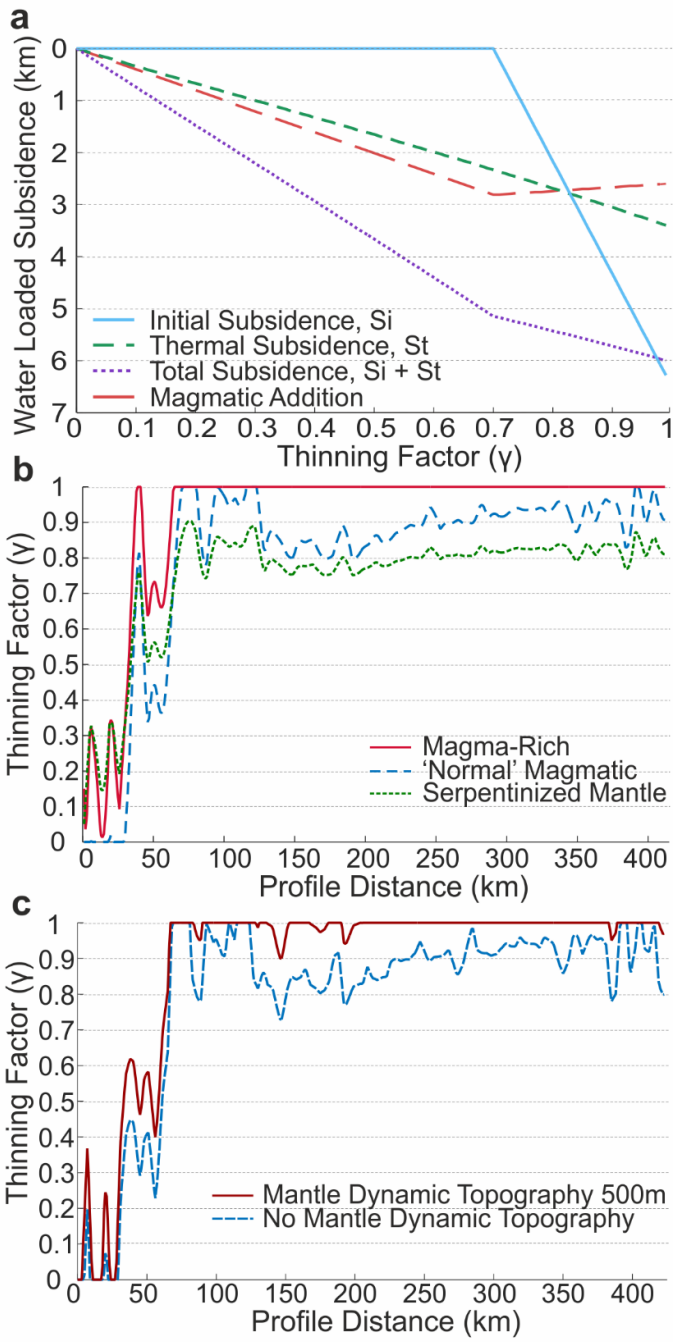

Fig. 3.5. Subsidence analysis a) Water loaded subsidence as a function of thinning factor for a 'normal' magmatic solution according to McKenzie (1978). b) Lithosphere thinning factors calculated from subsidence analysis for INE1-1000 for a magma-rich, a 'normal' magmatic solution and a serpentinised mantle solution. c) 'Normal' magmatic thinning factor from subsidence analysis showing the effect of 500 m of mantle dynamic topography.

3.2.3.1 Sensitivity to magmatic addition

As mentioned previously, Figure 3.5b displays the lithosphere thinning factor profile determined from subsidence analysis for a magma-rich decompression melt parameterisation. For the same water-loaded subsidence as the 'normal' decompression melt, the greater amount of magmatic addition gives a higher thinning factor and implies reduced remnant continental crust. Figure 3.5b also shows the lithosphere thinning factor profile for a parameterisation that represents the serpentinisation of exhumed mantle. Serpentinised mantle has been shown to have the equivalent mass deficiency as 3.1 km thick crustal basement (Cooper, 2010). The detailed explanation of how this can be used for subsidence analysis over serpentinised mantle is given in Cowie et al. (2015).

3.2.3.2 Sensitivity to present-day dynamic topography

Subsidence analysis is an independent way of calculating the lithosphere thinning factor from the gravity inversion but does not directly compensate for mantle dynamic topography. If a margin is experiencing mantle dynamic topography, then thinning factors calculated using subsidence analysis will be underestimated and less than those from gravity inversion. If present-day dynamic topography is known then a correction for it may be applied to the water-loaded subsidence from flexural backstripping, prior to conversion into lithosphere thinning factors. An example of this is shown in Figure 3.5c, where a correction for +500 m present-day dynamic uplift has been applied. A present-day dynamic uplift of +500 m is consistent with the difference between the distal oceanic sediment corrected RDA and the crustal thickness component RDA shown in Figure 3.4b (see Cowie et al., (2015) for further discussion on methodology).

3.2.4 Joint inversion of seismic and gravity data

Joint inversion of Moho depth using gravity and time domain seismic reflection data can be used to calculate the lateral variations in basement density and seismic velocity across the seismic profile. This joint inversion methodology described by Cowie et al. (2016), determines the combination of basement seismic velocities and densities needed to match the gravity inversion Moho with the interpreted seismic Moho in TWTT. Performing the joint inversion in the time domain avoids possible uncertainties in stacking velocities used in depth conversion.

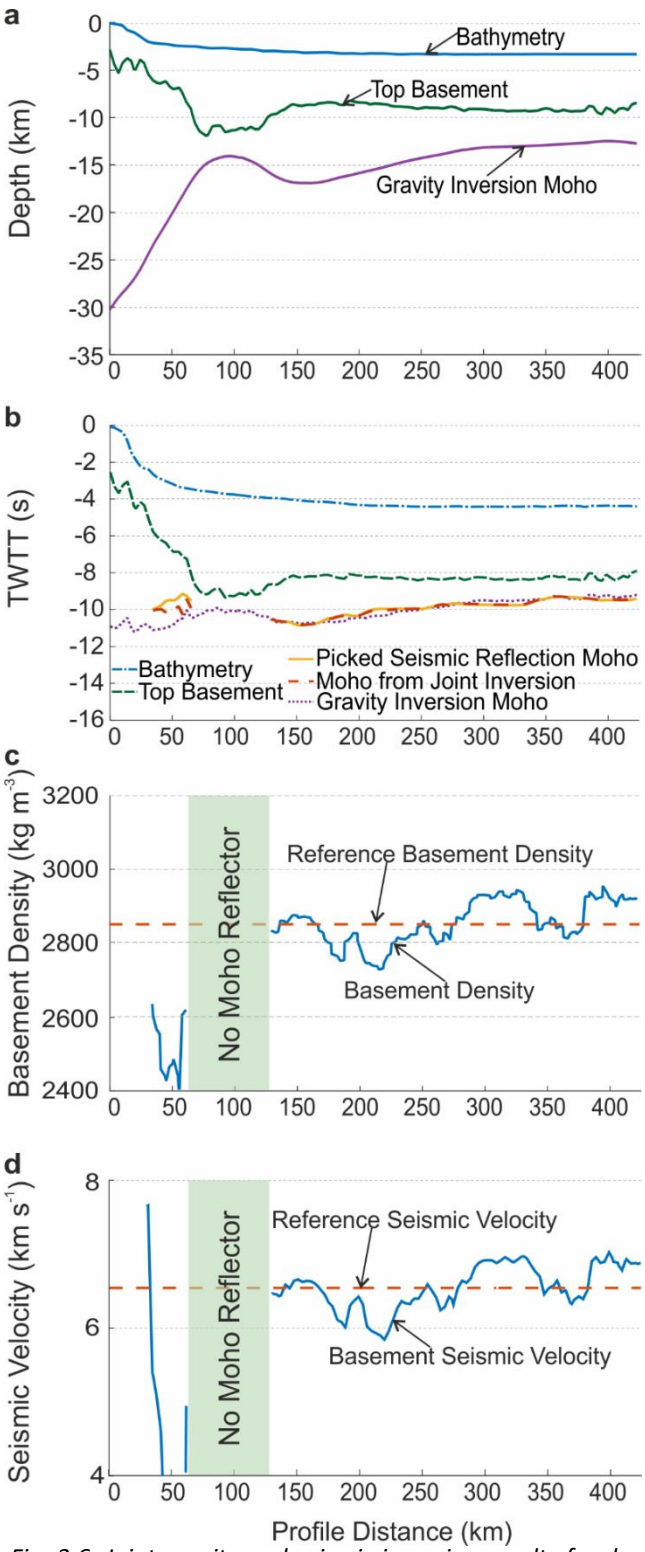

Fig. 3.6. Joint gravity and seismic inversion results for deep top basement surface a) Gravity inversion depth section using deep top basement pick. b) Two-way travel time cross section showing gravity inversion Moho, picked seismic reflection Moho and joint inversion Moho. c) Average crustal basement density variation resulting from the joint inversion. d) Average basement seismic velocity variation resulting from the joint inversion.

In the joint inversion process, first the Moho depth calculated from the gravity inversion (Fig. 3.6a) is converted into two-way travel time (TWTT) using a seismic velocity corresponding to the basement. Basement density and seismic velocity are linked by the empirical linear relationship defined by Birch, (1964), $V_p = 2.27*\rho + 0.25$. The initial basement density of 2850 kg m^{-3}, used in the gravity inversion, corresponds to a seismic velocity of 6.72 km s^{-1}. The gravity Moho depth (in time) is then compared to a seismic interpretation of the Moho made in the time domain (Fig. 3.6b). Differences between the two Moho's in the time domain arise due to heterogeneities of the basement density and seismic velocity of the crustal basement. By laterally varying the basement density and seismic velocity the gravity Moho (in time) is adjusted to fit the observed seismic Moho. The fit is achieved by iterative modifications of the basement density used in the gravity inversion to give Moho depth and the corresponding modifications to basement seismic velocity. The result of the joint inversion is the profiles of the lateral variation in basement density and seismic velocity.

Figures 3.6c and 3.6d show profiles of laterally varying average basement density and seismic velocity predicted by the joint inversion of the gravity and seismic Moho data. Basement densities predicted for the distal section of the seismic profile reach values of 2900 kg m^{-3}, consistent with densities for oceanic crust (Carlson and Herrick, 1990). In contrast, basement densities for the 9 km thick crust are noticeably less, reaching a low of 2750 kg m^{-3}. In the region of exhumed mantle, it is not possible to determine basement density or seismic velocity from joint inversion because no seismic Moho is visible. The low basement densities in the proximal domain may indicate that significant thicknesses of sediment are present beneath the top basement seismic interpretation.

3.3 Results

3.3.1 Testing top basement surface interpretations

Our seismic observations identified two possible candidates for top basement in the region interpreted as exhumed mantle. One interpretation is the deep top basement surface, situated at the base of a faulted set of parallel reflectors at ~12 km depth (Fig. 3.7a), which we interpret as being sedimentary material. In contrast, the shallow top basement surface is interpreted to lie at the base of passive infill (Fig. 3.7b) at ~9 km depth, similar to previous interpretations by Haupert et al. (2016), Sinha et al. (2015), Nemcock et al. (2015) and Pindell et al. (2014). We examine the differences and implications of using the two different top basement interpretations in our quantitative analysis.

Figure 3.7 shows and compares results from gravity inversion and RDA analysis using the two different interpretations of top basement surface. The deeper top basement surface at the base of the parallel reflectors produces a gravity inversion Moho and crustal basement thickness shown in Figure 3.7a. Between 75 km and 125 km the gravity Moho shallows to ~14 km, which is ~3 km below the picked top basement.

Placing top basement at the base of passive infill, ~2 km shallower than the deep top basement interpretation, produces the gravity inversion Moho shown in Figure 3.7b. The gravity Moho shows a varying topography across the profile with a similar pattern to Figure 3.7a. They differ though between 75 km and 125 km where the gravity Moho is deeper at 15-16 km giving a crustal thickness of ~5 km.

The region between 75 km and 125 km where the Moho depth and crustal thickness from gravity inversion differ, corresponds to the region which has previously been interpreted as exhumed mantle (Haupert et al., 2016; Nemčok et al., 2013; Sinha et al., 2015). The difference in crustal thickness from gravity inversion using the two different top basement interpretations is ~2 km. The deep top basement surface gives a crustal thickness of ~3 km. This crustal thickness is equivalent to the mass deficiency of serpentinised mantle with respect to the mantle (Cowie et al., 2015b). In contrast, the shallow top basement surface gives a crustal thickness of ~5 km, which is too deep for our solution to be interpreted as exhumed serpentinised mantle. This gravity inversion solution using the shallow top basement surface implies a thin layer of crustal basement in addition to serpentinised mantle, or alternatively a 5 km thick layer of crustal basement with no serpentinised mantle. No exhumation of mantle rocks is predicted using the shallow top basement surface

The associated thinning factors from gravity inversion calculated for the deep top basement surface (Fig. 3.7c) reach a maximum crustal thinning between 75 km and 125 km implying the complete removal of continental crust, consistent with the interpretation of exhumed mantle. Thinning factors for the shallow top basement surface (Fig. 3.7d) in a serpentinised mantle solution are less than 0.8, which is too low for complete continental crustal thinning to have occurred, implying the presence of some crustal material.

RDA results between 75 km and 125 km for the deep top basement surface are negative (Fig. 3.7e), implying crust is thinner than 7 km or absent, consistent with the signal expected by exhumed mantle. RDA results for the shallow top basement surface (Fig. 3.7f) are positive (~200 m) showing that the crust at this point is thicker than average 7 km thick oceanic crust,

a signal that is not indicative of exhumed mantle but consistent with the presence of very thin continental crust.

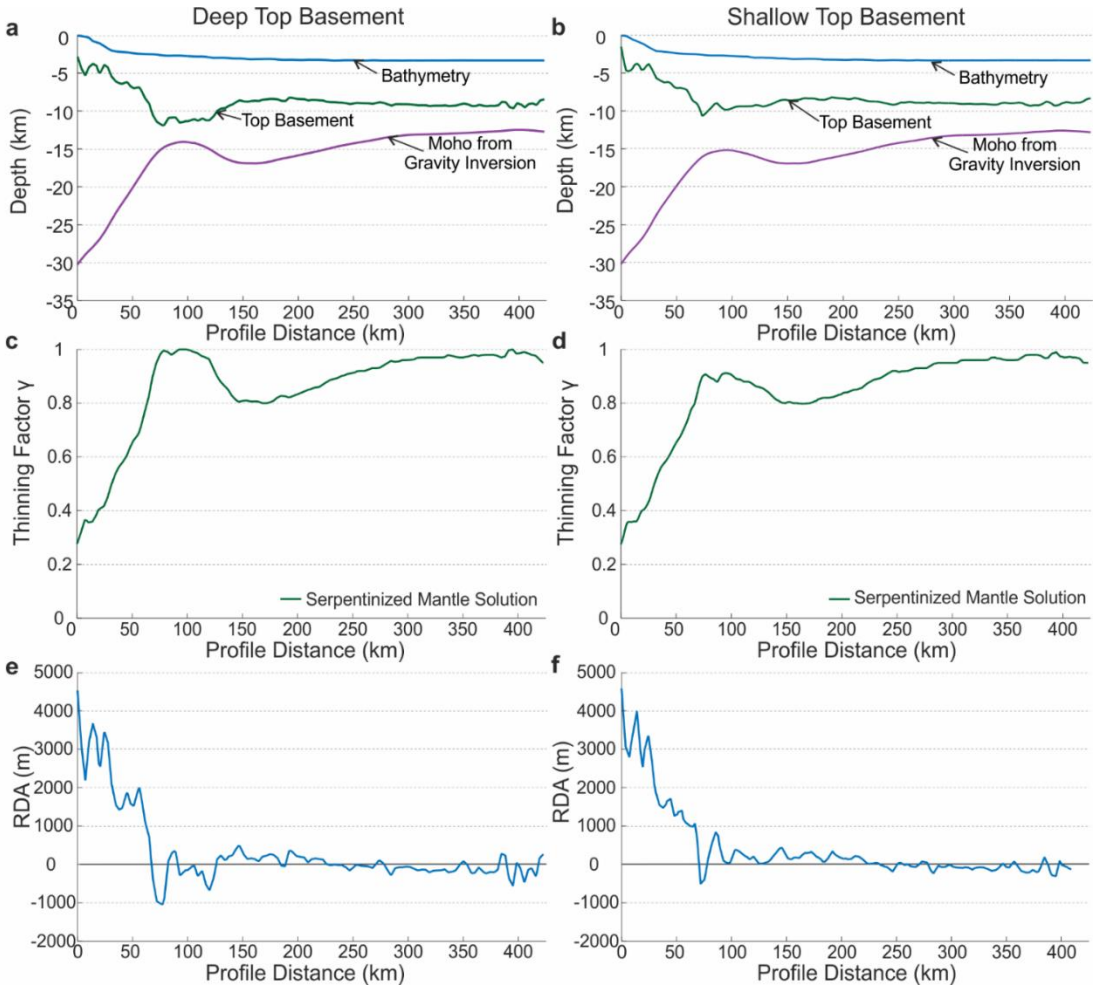

Fig. 3.7. Testing top basement surfaces a) Gravity inversion cross-section showing depth to the Moho using the deeper top basement surface below the package of parallel faulted reflectors. b) Gravity inversion cross-section showing depth to the Moho using the shallower top basement surface, above the package of parallel faulted reflectors. c) Lithosphere thinning factors associated with the gravity inversion shown in a). d) Lithosphere thinning factors associated with the gravity inversion in b). e) Residual depth anomaly analysis for deep top basement surface. f) Residual depth anomaly analysis for shallow top basement surface.

3.3.2 Geological scenarios

Resolving the magmatic budget cannot be done unambiguously which leads to several potential interpretations and implications for the estimation of magmatic volume (Tugend et al., 2018). We present five geological scenarios (Fig. 3.8) that are consistent with the integrated quantitative analysis. The interpretations are deliberately kept simple and are presented as end-members. Each scenario contains at least one feature that corresponds to previous studies and/or seismic interpretations such as exhumed serpentinised mantle (Haupert et al., 2016; Nemčok et al., 2013) or hyper-extended continental crust less than 10

km thick (Pindell et al., 2014). We also include two of the scenarios previously presented in Tugend et al. (2018) to test the nature of the transitional crust: ~ 9 km thick magmatic crust (Fig. 3.8a) or serpentinised mantle sandwiched between extrusive and intrusive additions (Fig. 3.8c). We later discuss the suitability of each scenario in Section 3.4.

Figure 3.8a displays exhumed serpentinised mantle beneath extensionally faulted sediments that are covered by passive infill. The ~9 km thick crust is composed entirely of magmatic material that transitions into normal oceanic crust with an average thickness of 5 km.

Figure 3.8b also shows exhumed serpentinised mantle beneath extensionally faulted sediments that covered are by passive infill. However, the more distal thick crust is a fragment of continental crust formed during breakup. The transition from this continental crustal fragment to oceanic crust would likely be accompanied by extrusive and intrusive magmatic additions.

Another scenario is termed the 'sandwich' scenario (Fig. 3.8c) (Gillard et al., 2017; Tugend et al., 2018) as it features serpentinised exhumed mantle and its associated sedimentary cover sandwiched between extrusive and intrusive magmatic additions. In this scenario, the exhumed mantle is progressively intruded oceanward before transitioning into thin oceanic crust.

An alternative to exhumed serpentinised mantle is the presence of hyper-extended continental crust less 10 km thick sitting atop serpentinised mantle material that is not exhumed to the seafloor (Fig. 3.8d, see also Pindell et al., 2014). Formation of hyper-extended continental crust could occur from 'outer marginal collapse' as suggested by Pindell et al. (2014). The outboard region of thick crust is represented as entirely magmatic in this scenario.

A final scenario (Fig. 3.8e), shows hyper-extended continental crust less than 10 km thick atop serpentinised mantle material adjacent to a continental fragment.

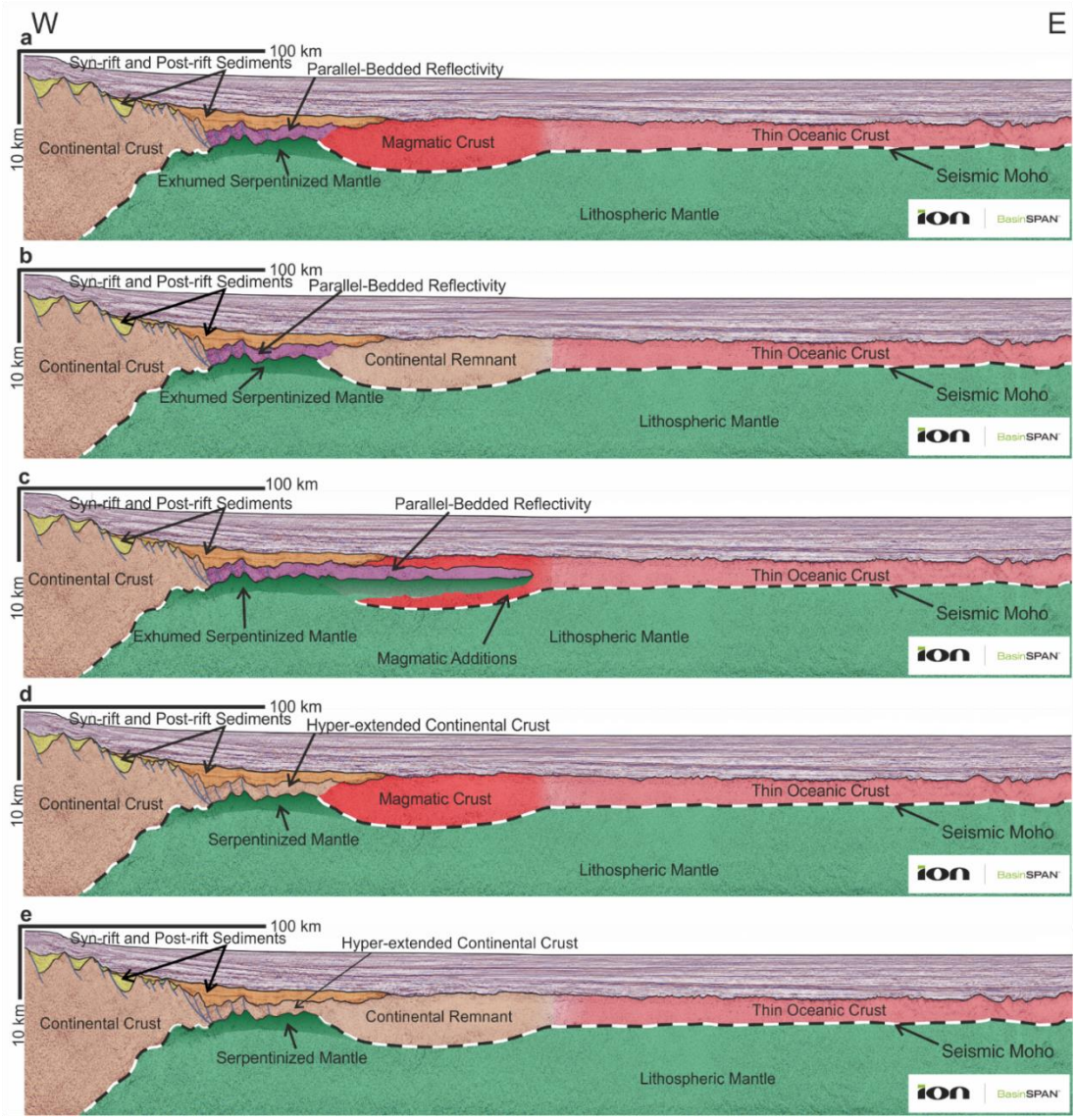

Fig. 3.8. Geological interpretations of INE1-1000 based on initial seismic observations, previous interpretations from other studies (Nemčok et al., 2013, Sinha et al., 2015 and Haupert et al., 2016) and initial quantitative results. a) Geological interpretation consisting of thinned continental crust transitioning into exhumed mantle below syn-rift passive infill shifting to thick magmatic crust for ~100 km followed by thin oceanic crust. b) Geological interpretation consisting of thinned continental crust transitioning into exhumed mantle below syn-rift passive infill shifting to a continental remnant approximately 100 km wide before transitioning into thin oceanic crust. c) 'Sandwich' scenario consisting of exhumed, serpentinised mantle topped with sediments surrounded by magmatic additions before transitioning into thin oceanic crust. d) Geological interpretation consisting of thinned continental crust transitioning into hyper-extended continental crust below syn-rift passive infill shifting to thick magmatic crust for ~100 km followed by thin oceanic crust. e) Geological interpretation consisting of thinned continental crust transitioning into hyper-extended continental crust below syn-rift passive infill shifting to a continental remnant approximately 100 km wide before transitioning into thin oceanic crust.

3.4 Discussion

In this section we discuss the various geological interpretations, described above, in conjunction with the results of the quantitative analysis and the regional plate kinematic history. Our preferred final interpretation is that of Figure 3.8a for which we give reasons below. In addition, we argue for the dismissal of the other five scenarios (Fig. 3.8b-e).

Both Figures 3.8d and 3.8e display hyper-extended continental crust arising from the crustal thickness estimates in the gravity inversion using the shallow top basement surface and the interpretation of Pindell et al. (2014). Seismic observations (Fig. 3.2) show a reflective package below the shallow top basement surface that contains parallel-bedded reflectors, indicative of sedimentary material, not continental crust. It is for this reason that we dismiss the geological scenarios presented in Figures 3.8d and 3.8e and the shallow top basement as a possible top basement surface (Fig. 3.7b).

Figures 3.8a, 3.8b and 3.8c display exhumed serpentinised mantle consistent with using the deep top basement surface in the gravity inversion to determine crustal basement thickness. These scenarios differ in their interpretation of the thick crust between exhumed mantle and oceanic crust, but all are consistent with results from the integrated quantitative analysis. We distinguish between them using seismic observations and the regional plate kinematic history.

Figure 3.8b shows a continental crust fragment between exhumed mantle and oceanic crust. This implies a jump of rifting prior to breakup and seafloor spreading in order to isolate the continental fragment. As discussed in section 3.1.2.1 there is evidence for an ocean ridge jump from between India/Elan Bank and Antarctica to the north between India and Elan Bank. If the interpretation shown in Figure 3.8b was correct, then the conjugate margin on the north-west side of Elan Bank should also show a transition from thinned continental crust to oceanic crust. However, interpretation of seismic reflection data from north Elan Bank (Sinha et al. 2015) shows a transition from thin continental crust to exhumed mantle and then to oceanic crust (see fig. 5 in Sinha et al., 2015). This suggests that the interpretation shown in Figure 3.8b is not consistent with observations.

The interpretation presented in Figure 3.8c is similar to that proposed by Tugend et al. (2018). In this scenario, the region of thicker crust between exhumed serpentinised mantle and oceanic crust consists of magmatic material that is extruded over and intruded within, exhumed serpentinised mantle with a cover of sedimentary material. In this scenario the

exhumation of serpentinised mantle is accompanied by a progressive increase in decompression melt production which produces a 'sandwich' of exhumed serpentinised mantle with extrusive volcanic material above and intrusive magmatic material below (Tugend et al., 2018). This scenario requires a single breakup event with a gradual increase in the volume of decompression melting. This complex basement transition to oceanic crust was initially suggested to occur at the conjugate Australia and Antarctica margins by Gillard et al. (2015). Our seismic observations (Fig. 3.2) do not show reflectivity suggestive of a 'sandwich' despite having good visibility down to the Moho. Seismic reflection data does not image these transitions well, one exceptional example from offshore West Africa (see fig. 2 in Gillard et al., 2017) displays this reflectivity but their interpretation often relies on analogues preserved in onshore remnants. Although our quantitative analysis cannot exclude the presence of an exhumed mantle 'sandwich', it is not supported by our seismic observations suggesting that this model is not applicable to the East Indian rifted margin.

Our preferred scenario, shown in Figure 3.8a, interprets the composition of the 9 km thick crust between exhumed mantle and oceanic crust as thick magmatic crust. Figure 3.9 shows the crustal cross section from gravity inversion, the RDA analysis, thinning factor from gravity inversion and subsidence analysis and basement density from joint inversion of gravity and seismic reflection data, which support this preferred interpretation. There is no single parameterisation of decompression melting within the gravity inversion and subsidence analysis that fully explains the seismic observations or fits with the geological interpretations for INE1-1000. Therefore, the preferred solution is a composite interpretation of the different melt parameterisations as shown in Figure 3.9a. From continent to ocean, the preferred composite of decompression melt parameterisation is as follows: magma-poor (0-55 km), serpentinised mantle (55-105 km), magma-rich (105-285 km) and 'normal' magmatic (285-423 km). Our gravity inversion melting parameterisation representing 'magma-rich' rifting over the thick, crustal area (Fig. 3.9a) is consistent with previous interpretations as well as seismic observations (Fig. 3.2d) that depict various intrusive magmatic features and extrusive features such as volcanoes and dipping reflector sequences. RDA analysis results over the thick crustal area are positive (Fig. 3.9b); indicating the crust there is thicker than normal oceanic crust. Both gravity inversion and subsidence analysis lithosphere thinning factors

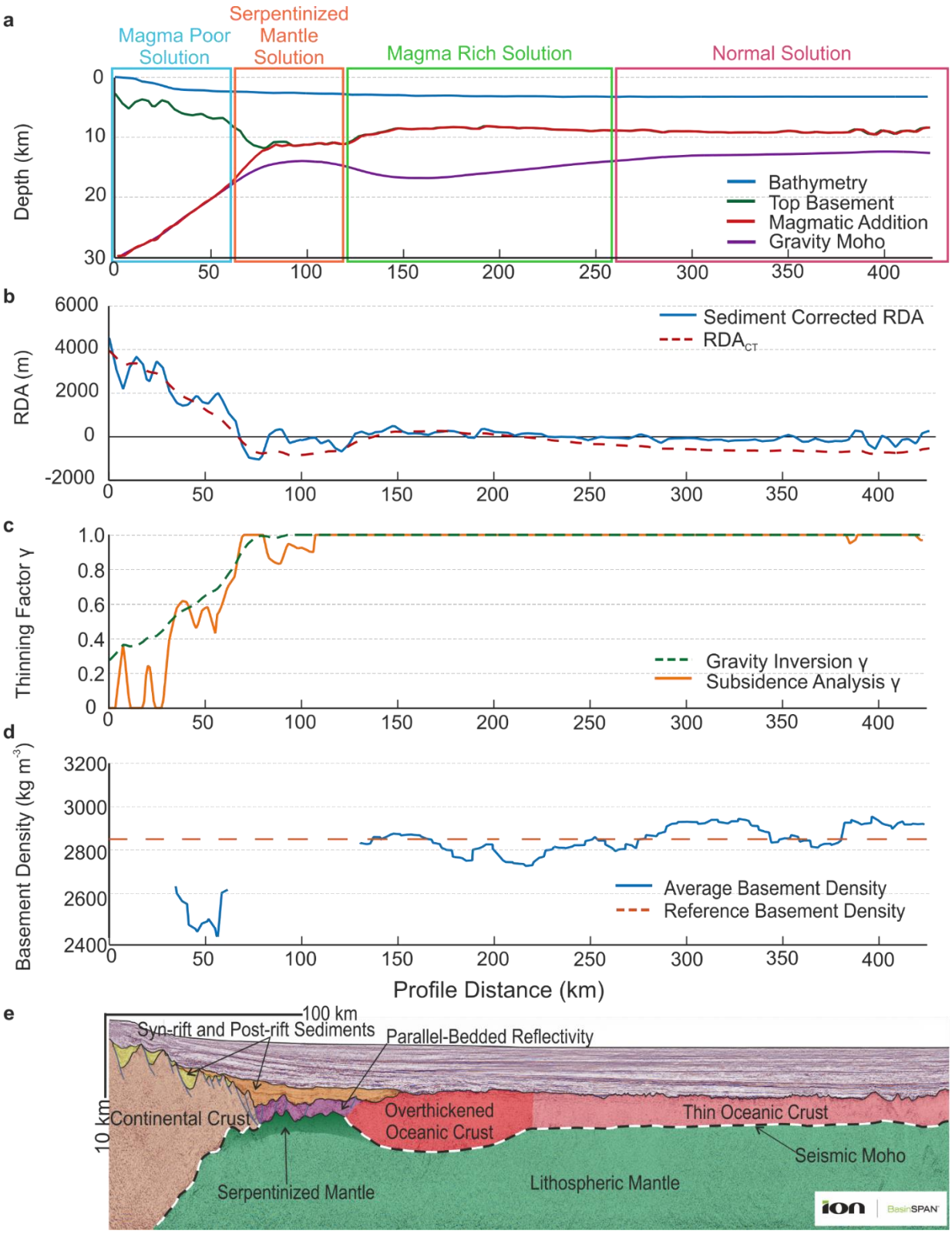
a
Magma Poor Solution
Serpentinized Mantle Solution
Magma Rich Solution
Normal Solution
Depth (km)
Bathymetry
Top Basement
Magmatic Addition
Gravity Moho
b
RDA (m)
Sediment Corrected RDA
RDA_CT
c
Thinning Factor γ
Gravity Inversion γ
Subsidence Analysis γ
d
Basement Density (kg m-3)
Average Basement Density
Reference Basement Density
Profile Distance (km)
e
100 km
10 km
Syn-rift and Post-rift Sediments
Parallel-Bedded Reflectivity
Continental Crust
Overthickened Oceanic Crust
Thin Oceanic Crust
Seismic Moho
Serpentinized Mantle
Lithospheric Mantle

reach 1.0 at the onset of the thick crust, implying the absence of continental material (Fig. 3.9c). Joint inversion of seismic and gravity data (Fig. 3.9d) show that the density of the 9 km thick crust between exhumed mantle and oceanic crust is less than that of the distal oceanic crust whose density is as expected for oceanic crustal basement (Carlson and Herrick, 1990). This lower density for the 9 km thick crust suggests the presence of lighter material, possibly sedimentary material or volcaniclastics. This is supported by seismic observations (Fig. 3.2) that indicate the presence of volcanoes at the top of the thick crust as well as dipping reflector sequences, which could be sources for volcaniclastic material.

The juxtaposition of exhumed mantle and thick magmatic crust, as shown in Figures 3.8a and 3.9, can be explained by the known reorganisation of seafloor spreading, via an ocean ridge jump, from the Enderby Basin, between Elan Bank and Antarctica northwards, to between India and Elan Bank (Gaina et al., 2003, 2007). A reorganisation of seafloor spreading into pre-existing exhumed mantle would place newly formed magmatic crust next to the exhumed mantle. A fossilised ocean ridge is present within Enderby Basin dated at 124 Ma (Gaina et al., 2003) suggesting a ridge jump occurred during rifting. Additional evidence comes in the form of the microcontinent Elan Bank, the formation of which requires a ridge jump in order to isolate it from the East Indian margin and transfer it to the Antarctic plate, where it lies in the present-day. Plate reconstructions (Gaina et al., 2003, Muller et al., 2008, Sinha et al., 2015) also depict a ridge jump from between Elan Bank and Antarctica to between India and Elan Bank during the Aptian at ~124 Ma, based on magnetic anomalies and seismic reflection data. This evidence combined with the development of proto-Kerguelen mantle plume magmatism at the time of India-Antarctica lithospheric breakup (Olierook et al., 2016), could explain decompression melting exceeding that of normal seafloor spreading (7 km, White et al., 1992) leading to thicker magmatic crust. This same development of the proto-Kerguelen mantle plume may also be a contributing factor to the ocean ridge jump.

In our interpretation, the scenario shown in Figures 3.8a and 3.9, containing thick magmatic crust outboard of exhumed mantle is not due to the inherent evolution of exhumed, serpentinised mantle into magmatic crust caused by the escape of retained melt (Lizarralde et al., 2004). Instead, the juxtaposition of exhumed mantle and thick magmatic crust is a result of a seafloor spreading reorganisation into exhumed mantle coinciding with an asthenosphere temperature anomaly.

By combining seismic observations, quantitative analysis and regional plate kinematic history we are able to dismiss alternative scenarios, arriving at a single favoured interpretation where the East Indian rifted margin preserves exhumed mantle juxtaposed to thick, magmatic crust. Classifying the East Indian rifted margin, in particular the Krishna-Godavari Basin, as magma-poor suggests little magmatism during rifting and breakup. However, the results presented within this study suggest it is not a simple end-member rifted margin, instead displaying both magma-poor and magma-rich characteristics.

3.5 Summary

Establishing the volume of magmatic crust on a margin using quantitative methods is important in distinguishing margin type. Yet, the classification of end-member magmatic rifted margin types is often assumed based on a morphological features interpreted from seismic data without the use of quantitative validation. ION line INE1-1000 is often described as a 'classic' magma-poor margin based on seismic interpretation alone. However, we have demonstrated that, by using an integrated set of geophysical techniques, that thick magmatic crust may separate exhumed serpentinised mantle and oceanic crust. Our quantitative analysis consists of gravity inversion, residual depth anomaly analysis, subsidence analysis and joint inversion of gravity and seismic reflection data alongside seismic observations. This analysis together with the plate kinematic history of the region indicates that the thick crust separating exhumed mantle and oceanic crust on the East Indian rifted margin is a result of polyphase rifting that is not genetically related to magma-poor continental breakup and seafloor spreading initiation. The first rift phase consisted of magma-poor rifting forming exhumed mantle, while the second phase of rifting resulted from a northwards reorganisation of seafloor spreading, forming 9 km thick magmatic crust. We find no evidence to suggest the thick crust formed via the release of retained melt within the mantle and is therefore not related to magma-poor continental breakup and the transition to magmatic seafloor spreading. Our interpretation suggests that the East Indian rifted margin is not a simple end-member magma-poor margin, and instead has characteristics of both magma-poor and magma-rich rifted margins because of the ocean ridge jump. As both rift phases contributed towards the final rifted margin structure, using end-member terminology of magma-poor or magma-rich to classify the rifted margin is misleading.

Supplementary Information

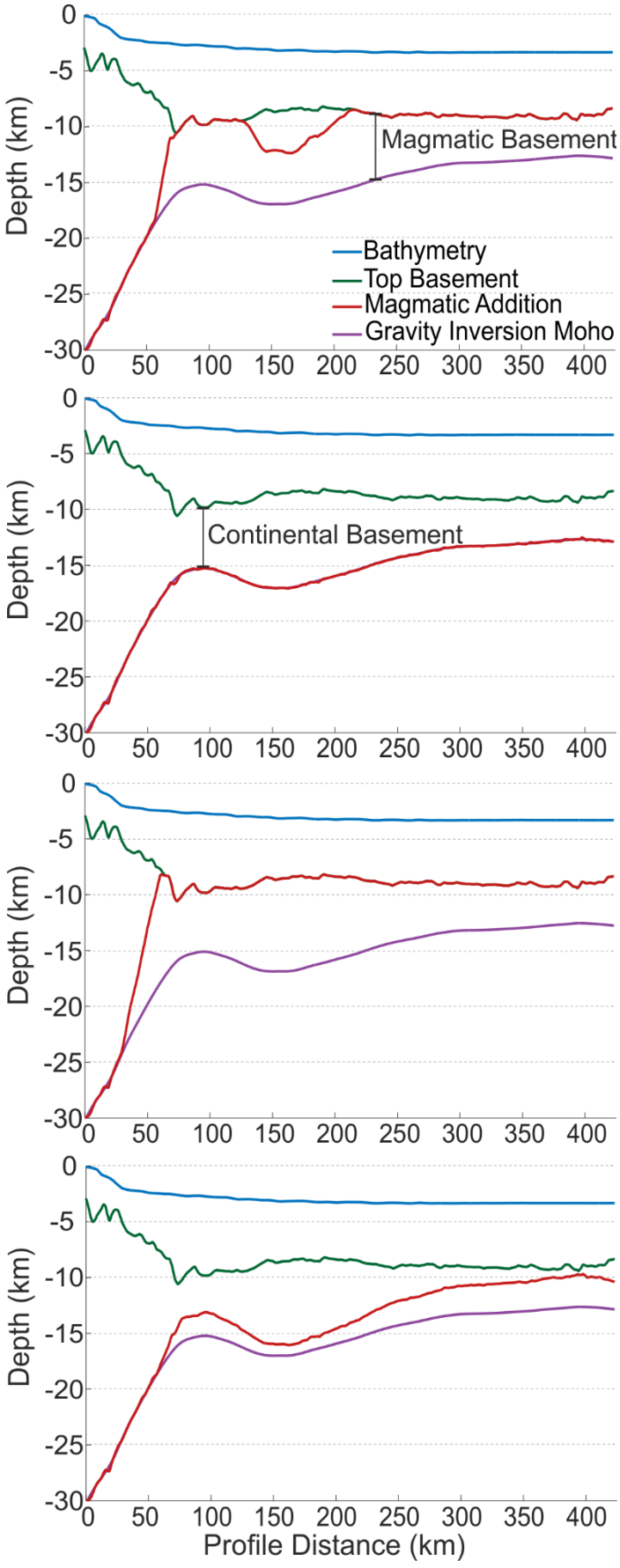

Fig. 3.S1. Gravity inversion parameterisation of decompression melting results for the shallow top basement surface. a) 'Normal' magmatic solution. b) Magma-poor solution. c) Magma-rich solution d) Serpentinised mantle solution.

Chapter 4

Origin, composition and relative timing of seaward dipping reflectors on the Pelotas rifted margin

This chapter is a manuscript currently under review at Marine and Petroleum Geology. The authors of the manuscript are Caroline Harkin (first author), Nick Kusznir, Alan Roberts, Gianreto Manatschal and Brian Horn. This chapter investigates the formation of seaward dipping reflectors on the Pelotas margin using a new method termed 'the basalt fraction' within the gravity inversion. Data were provided by ION Geophysical (Brian Horn), seismic interpretation was carried out by Alan Roberts, with discussion and interpretation of results undertaken by Caroline Harkin, Nick Kusznir, Alan Roberts and Gianreto Manatschal. This manuscript is accompanied by supplementary information in the form of a short discussion, which has been provided at the end of the chapter.

Paper Abstract

The mechanism by which seaward dipping reflectors (SDRs) are formed is a topic of debate. Two contrasting models exist for their formation, the volcanic-faulting model and the volcanic-loading model. Each of these models has important implications for the processes which control the structure and formation of magma-rich rifted continental margins. We have examined high-quality deep-seismic reflection data across the Pelotas Basin, offshore Brazil. This data reveals a remarkable set of SDRs, for which we have investigated the likely nature of their formation. The total package of SDRs has an across-strike width of ~200 km and a variable vertical thickness of ~10-17 km, previously interpreted as volcanic flows. Detailed observations, however, show changes in seismic character and geometry within the SDR package, which suggest a complex and varied evolution.

We have used gravity anomaly inversion and seismic observations together to investigate the likely composition of the SDRs by determining the proportion of basaltic material to sedimentary/volcaniclastic material (basalt fraction) within the SDRs. This has been achieved by minimising the difference between the depth of the gravity Moho and seismic Moho in order to quantify the lateral variation in basalt fraction, taken to be proportional to the bulk density of the package. The density of the SDR package together with seismic interpretation

is then used to infer the composition, depositional environment, source and time of formation relative to breakup.

Our analysis suggests that the overall SDR basalt fraction and bulk density decrease oceanwards, possibly due a change in the type of volcanic deposits from predominantly subaerial to volcaniclastics, possibly deposited subaqueously. The SDRs can be split into three sub-packages. The two inner SDR packages are interpreted to consist of lava flows sourced from syn-tectonic, subaerial eruptions, associated with the onshore Paraná Large Igneous Province, flowing eastwards into an extensional basin. The outer SDR package shows reflector geometries that progressively offlap oceanwards, interpreted as extrusion sourced from an eastwards-migrating, newly formed ocean ridge. Our analysis suggests that both the volcanic-faulting and volcanic-loading models for SDR formation are applicable to the Pelotas rifted margin, recording distinct syn-rift and syn-breakup magmatic events. We show that both SDR formation models can be recognised in a naturally occurring example and can coexist on the same margin.

4.1 Introduction

Magma-rich rifted margins are typically associated with extensive amounts of magmatic addition to the crust, comprising extrusive lavas and intrusive dykes, sills and gabbroic bodies. Magmatic extrusives commonly take the form of seaward dipping reflectors (SDRs), believed to result from the lateral migration and accretion of both subaerial and submarine lava flows during rifting, breakup and initial sea-floor spreading (e.g. Bodvarsson and Walker, 1964; Buck, 2017; Geoffroy, 2005; Hinz, 1981; Mutter et al., 1982). The formation and internal composition of SDRs has been generalised worldwide from a small number of well penetrations, localised onshore occurrences and seismic studies. As a result, two contrasting models exist for the formation of SDRs. In this paper we investigate whether either of these models can be applied to a spectacularly imaged set of SDRs, on the Pelotas margin, southern Brazil. To do so, we have used gravity inversion and seismic interpretation to investigate the composition, origin and timing (relative to breakup) of the Pelotas SDRs and have then interpreted the processes which led to their formation.

The term seaward dipping reflectors refers to a wedge of stacked, arcuate reflectors that dip seawards with increasing flow thickness down dip (Mutter et al., 1982). SDR wedges vary in size globally, but can reach several kilometres in vertical thickness and can extend laterally for hundreds of kilometres (Hinz et al., 1999; Mutter et al., 1982; R. S. White et al., 2008). Seismic velocities within SDR packages typically increase down-dip and commonly average

~5 km s^{-1} for the entire section (Mutter et al., 1982; R. S. White et al., 2008). Such velocities are compatible with an igneous origin, particularly basalt flows, leading to the assumption supported by limited well data (Fitton et al., 2000; Planke and Eldholm, 1994), that SDRs are composed predominantly of primary igneous material with minor associated deposits of tuffs, volcaniclastics and/or sedimentary material. The composition of SDRs worldwide is generally assumed to follow this premise, but with drilling expensive and SDRs often buried deep beneath sedimentary cover, the determination of actual SDR composition is often based only on seismic interpretation or observations from landward-flow equivalents. To advance this basic understanding, we present here a new technique to investigate the composition of SDRs using both gravity anomaly and seismic reflection data.

Using wide-angle, high-quality seismic reflection data and gravity anomaly inversion, we examine SDRs on the Pelotas margin, Brazil to investigate whether they are composed predominantly of massive basaltic flows, sedimentary/volcaniclastic material, or a combination of both. By matching the Moho in both depth and two-way travel-time (TWTT) from gravity and seismic reflection data, we test the proportion of basaltic material to sedimentary/volcaniclastic material (the basalt fraction). The results are used to determine the lateral variation in basalt fraction within the SDRs, which parameterises the bulk density of the package. Interpretation of SDR composition and their associated environment of emplacement can then lead to an interpretation of the magmatic/depositional source and timing relative to breakup. From this, we can assess the applicability of existing models for SDR formation to the Pelotas example. We use the joint inversion of gravity and seismic Moho results to test our approach and investigate the combined density of the SDR package and basement, comparing it against laterally varying basalt fraction results.

4.1.1 Previous models for the formation of seaward dipping reflectors

SDRs are believed to form from intense volcanic activity during rifting and breakup (Buck, 2017; Hinz, 1981; Mutter et al., 1982; Paton et al., 2017) and are often related to the formation of large igneous provinces (LIPs) (Buck, 2017). Their basic structure consists of a series of stacked flows forming a wedge with an angle of dip that increases with depth.

On the Outer Vøring Plateau (offshore Norway), Hinz (1981) showed that the seismic velocities of such flows vary from 3-4 km s^{-1} in the upper section of the wedge to 5 km s^{-1} in the lower section of the wedge. Similarly, also on the Outer Vøring Plateau, Mutter et al. (1982) and Talwani et al. (1981) derived an average velocity of 4.8 km s^{-1} across a set of SDRs for which the total range in velocity is 2.6 km s^{-1} to 6.4 km s^{-1}. Within the SDRs of the Faroes

margin (NE Atlantic), White et al. (2008) noted a marked decrease in velocity at the base of the flows (~4.2-4.5 km s^{-1},), while the average seismic velocity of the entire wedge is ~5 km s^{-1}. These seismic studies, together with sparse well data, have led to the general conclusion that SDRs are composed predominantly of volcanic material with localised interbedded deposits of volcaniclastic/sedimentary material.

Two different models for SDR formation exist within the literature. One suggests that the flows are formed subaerially on continental crust during fault-controlled extension prior to continental breakup, sourced from intrusive dykes (Geoffroy, 2005; Hinz, 1981; Paton et al., 2017; Quirk et al., 2014). The other also suggests that the flows are erupted subaerially and sourced from dykes, but contrastingly they are considered to form the uppermost layers of oceanic crust at the initiation of seafloor spreading (Bodvarsson and Walker, 1964; Mutter et al., 1982; Talwani et al., 1981). Following the terminology used by Buck (2017) we call these models the volcanic-faulting model and the volcanic-loading model respectively (Fig. 4.1). Barton & White (1997) have previously suggested both types of SDRs exist on the Rockall

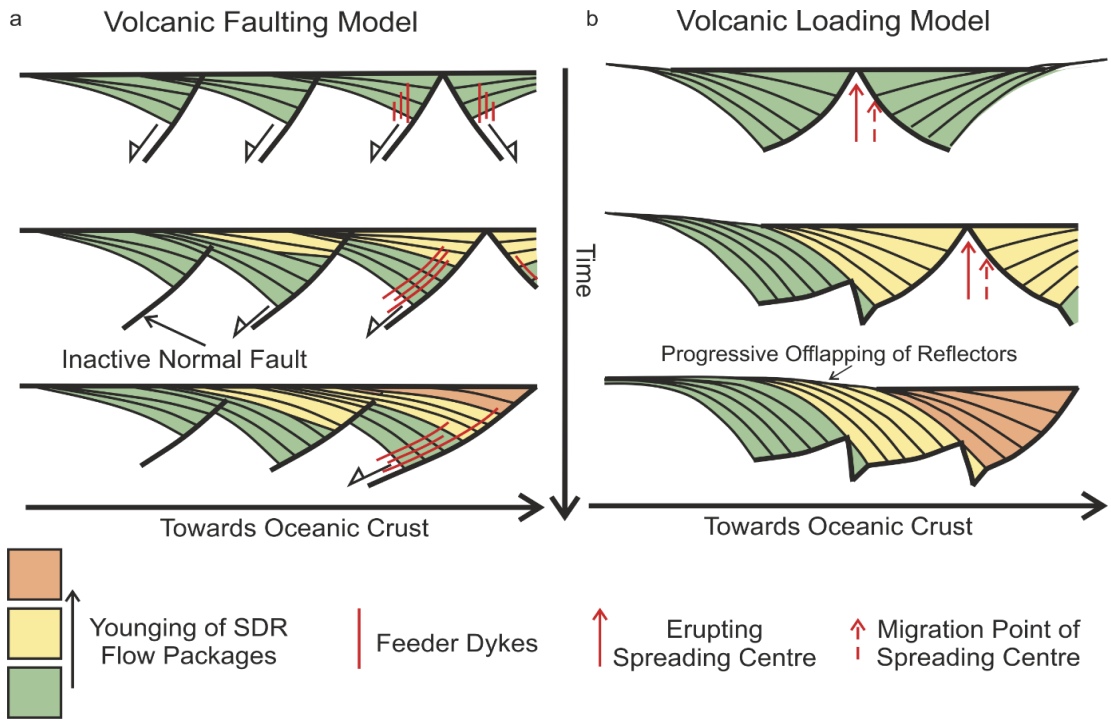

Figure 4.1. Cartoon summary of models for SDR formation (after Buck, 2017). a) Volcanic faulting model where large normal faults that dip towards the continent are intruded by dykes that fill the half-grabens with extrusive volcanic material. These faults progressively rotate and become inactive as younger faults are generated in an oceanwards direction. b) Volcanic loading model where a spreading centre erupts lava subaerially, forming successions of flows that dip towards the spreading centre. Migration of the spreading centre leads to a stacking of the SDR packages towards the oceanic crust.

Atlantic margin, while McDermott et al. (2018) interpret both types of SDR in the Pelotas Basin.

The volcanic-faulting model for SDR formation (Fig. 4.1a) invokes large landward-dipping normal faults, within continental crust, as the main mechanism for forming a large volume of accommodation space which then fills with extrusive basalt flows (Barton and White, 1997; Buck, 2017; Geoffroy, 2005; Geoffroy et al., 2001; Gibson and Love, 1989; Quirk et al., 2014). Using seismic reflection and well data from the Vøring Plateau (ODP Site 642), Eldholm et al. (1989) and Gibson & Love (1989) suggested that the observed SDR sequence formed by normal fault extension within continental crust. This work showed that the Vøring Plateau SDRs consist of subaerial tholeiitic basalt flows with a high silica content resulting from continental crustal contamination. They also contain xenoliths of gneiss and quartz-mica schist, implying the underlying basement comprises continental crust. These flows exhibit a low proportion of dykes relative to the flow volume, but it is suggested that SDR formation occurred predominantly by lava flowing onto continental crust from feeder dykes intruded along normal fault planes, which subsequently rotated to a low angle. The SDR structure should therefore consist of a thick inclined pile of lava flows underlain by a sheeted dyke complex and a fault surface. Later studies (Geoffroy, 2005; Geoffroy et al., 2001), have also used the same mechanism and process to explain SDR formation.

The volcanic-loading model (Fig. 4.1b) originated from onshore observations of dyke-fed volcanic flows in Iceland, that dip towards volcanic centres at ~5-10° and also thicken down-dip (Palmason, 1973; Palmason and Saemundsson, 1974; Walker, 1959, 1960). Subsidence, as a result of the successive loading of the flows, was recognised as the cause for their increasing dip (Walker, 1960). A kinematic model for the emplacement of the flows was developed by Bodvarsson and Walker (1964), in which isostatically-compensated lava flows are fed by dykes at a spreading centre. Subsequent studies have used the volcanic-loading model to explain the formation of SDRs as coincident with sea-floor spreading (Mutter et al., 1982; Paton et al., 2017; Pindell et al., 2014; Talwani et al., 1981).

4.1.2 The opening of the South Atlantic Ocean and the formation of the Paraná-Etendeka province

This study investigates a regional seismic line from the Pelotas Basin, offshore Brazil that lies on the Arc de Torres (Fig. 4.2). Offshore southern Brazil comprises several basins; the Esperito-Santo Basin, the Campos Basin, the Santos Basin and the Pelotas Basin (Fig. 4.2a, Stica et al., 2014). Typical magma-poor features dominate the northern basins (Esperito-

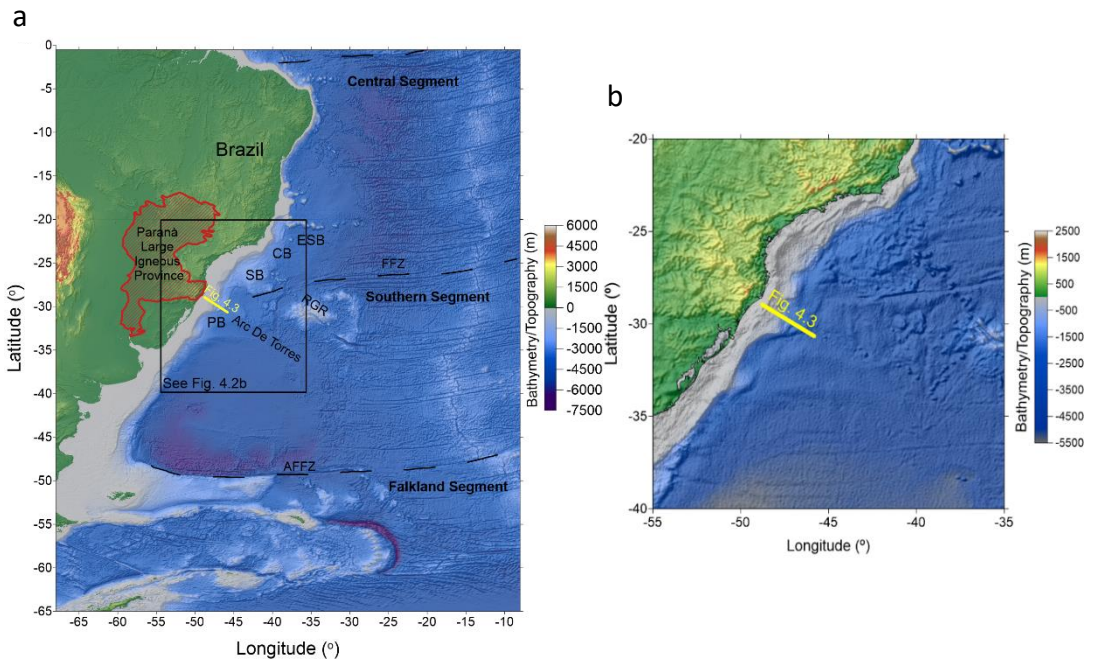

Figure 4.2. a) Bathymetric/topographic map of the South Atlantic on the western side of the Mid-Atlantic Ridge, with an overlay of shaded-relief free-air gravity anomaly. ESB, Esperito-Santo Basin; CB, Campos Basin; SB, Santos Basin; PB, Pelotas Basin; AFFZ, Agulhas-Falkland Fracture Zone; FFZ, Florianopolis Fracture Zone; RGR, Rio Grande Rise. Note location of seismic line (Fig 4.3) in relation to Paraná LIP and Arc De Torres. b) Enlargement of box shown in (a), location of seismic profile shown in Fig. 4.3.

Santo and Campos), while large amounts of volcanism typical of magma-rich margins, dominate in the south (Santos and Pelotas) (Stica et al., 2014). Namibia is often cited as the conjugate margin to the Pelotas Basin (Blaich et al., 2013; Gladczenko et al., 1997), however, plate reconstructions (Graça, 2018) suggest the conjugate to the Pelotas Basin could be the Western Rio Grande Rise, a small continental block forming part of the Rio Grande Rise (Fioravanti, 2014)(Fig. 4.2a), possibly affecting the overall symmetry of the Pelotas margin and its conjugate.

Formation of the South Atlantic Ocean resulted from the breakup of the South American and African plates as part of Gondwana during the Late Jurassic and Early Cretaceous. Diachronous breakup occurred from south to north, with the oldest breakup in the southern South Atlantic recorded at ~138 Ma, continuing through to ~115 Ma in the northern South Atlantic (Pérez-Diaz and Eagles, 2014). Breakup for the Pelotas Basin is dated using magnetic anomaly M4 at ~127 Ma (Gradstein et al., 1994; Hawkesworth et al., 2000).

The formation of the Paraná-Etendeka large igneous province (LIP) (Fig. 4.2a) is believed to be related to the breakup of Gondwana. The Paraná-Etendeka LIP covers an estimated area of 1.2×10^6 km^2 in both South America and Africa, with additional offshore deposits (Hawkesworth et al., 1992). Onshore deposits in South America reach the coastline at one

location in the Pelotas Basin, where the seismic line is situated. There is a major geographic asymmetry in the Paraná-Etendeka LIP, with ~95% of the rocks preserved on the South American plate (Paraná). The majority of the extrusives have been identified as tholeiitic basalts with subsidiary deposits of rhyolites, rhyodacites and andesites (Hawkesworth et al., 2000; Peate et al., 1992; P.R. Renne et al., 1996; Stica et al., 2014).

The main eruption period of the Paraná-Etendeka LIP is believed to have occurred within a relatively short time-period of ~3 Myr, with early ages recorded at ~133 Ma for Paraná basalts and ~131 Ma for the Ponta Grossa dyke swarm located in the northern region of the Paraná (P.R. Renne et al., 1996). Peak activity of the Paraná has been identified between 133-130 Ma with related volcanism continuing until 124 Ma (Hawkesworth et al., 2000).

4.2 Seismic observations

A wide-angle, long-offset seismic-reflection line from the Pelotas Basin (courtesy of ION Geophysical) has been used to establish a seismic interpretation that can be used as the basis for subsequent quantitative modelling and analysis (Fig. 4.3). A previous seismic interpretation of this line was carried out by Stica et al. (see fig. 6, 2014) and McDermott et al. (2018).

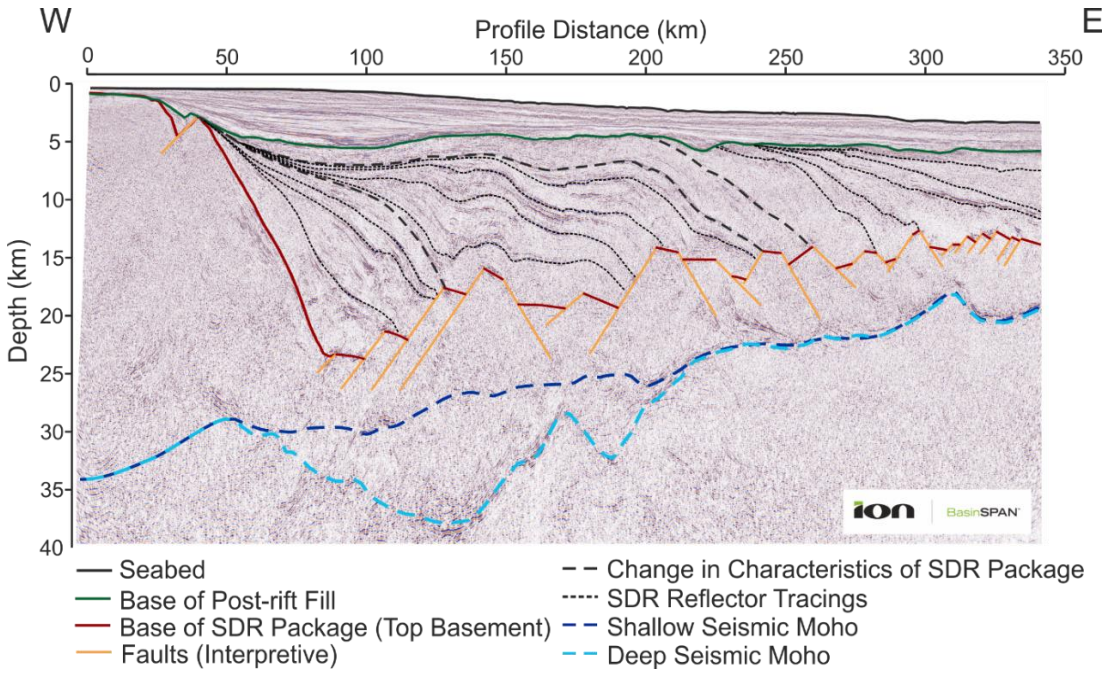

Figure 4.3. Seismic interpretation of Pelotas PSDM seismic profile, see Fig. 4.2 for location.

The pre-stack depth-migrated (PSDM) seismic profile has allowed us to interpret the geological boundaries of top basement and seismic Moho (Fig. 4.3). When interpreting the

seismic Moho, we look for a deep continuous reflector, of which there are two possible candidates (see discussion below). For top basement we take the base of the sediment fill and extrusive magmatic material (SDRs). We have also interpreted the base of the post-rift sediment fill above the SDR package, defining a base-sediment/top-SDR surface.

At the proximal margin, top basement is sub-horizontal at a shallow depth of ~500 m, passing eastwards into a more steeply-dipping surface (~25°) which reaches a maximum depth of ~23 km at line coordinate ~90 km. The top basement surface then follows an interpreted series of normal faults, which dip both continentwards and oceanwards, however the vertical extent of the faults into the basement is not clear. Sub-horizontal reflectors are occasionally visible at the base of the overlying flows possibly indicative of horsts. The hummocky geometry of the overlying flows also suggests an underlying set of horsts and grabens across most of the profile (see also Stica et al., 2014, fig. 6). These structures shallow oceanwards from a depth of ~23 km to ~14 km (Fig. 4.3).

Between the base of the post-rift sediments and the top basement is the package of seaward dipping reflectors which have previously been interpreted as volcanic flows by Stica et al. (2014). A lateral change in first-order SDR geometry occurs at line-coordinate ~200 km, west of which proximal reflectors appear (in 2D) to originate from a single-point source, while to the east, reflectors appear to migrate laterally towards the eastern end of the profile (Fig. 4.3).

Within the proximal SDRs two further separate packages can be seen (Fig. 4.3). The innermost reflectors have a single point of origin (at ~55 km) and extend across a distance of ~50 km as relatively smooth reflectors forming a wedge. These reflectors are also the deepest, reaching a depth of ~23 km. Immediately outboard and stratigraphically above, another set of proximal SDR reflectors (at a line-distance of 60-210 km) are more laterally extensive (~150 km), with an undulating geometry over the underlying top-basement horst and graben structure (Fig. 4.3). This package also originates from a single-point source in the west, close to that of the innermost SDRs, but the reflectors reach a shallower maximum depth of ~17 km. The uppermost oceanward SDRs progressively offlap eastwards towards the end of the profile, forming relatively sub-parallel flows dipping at ~5° and thickening down-dip. The oceanward SDRs are ~10 km thick with individual reflectors extending across ~75 km. Separating the proximal and oceanward SDRs is a transitional package with weak internal reflectivity and a seismically-discontinuous upper surface.

On Figure 4.3 two possible seismic Moho candidates have been identified. One, the shallow seismic Moho, is interpreted approximately parallel to the top basement surface below the proximal SDRs, shallowing as top basement shallows. The other, the deep seismic Moho, lies deep below the proximal SDRs, reaching a maximum depth of 39 km (Fig. 4.3) before sharply rising to meet the shallow seismic Moho at a line-distance of 210 km and a depth of 24 km. Both candidates for seismic Moho then follow a strong reflector oceanwards, approximately 6 km below the top basement surface.

4.3 Gravity inversion to determine Moho depth

At rifted margins gravity inversion can be used to estimate the depth to the Moho and lithosphere thinning factor. The gravity inversion follows the methodology previously published by Greenhalgh & Kusznir (2007), Chappell & Kusznir (2008a) and Kusznir et al (2018). Input requirements for the gravity inversion are bathymetry (Smith and Sandwell, 1997), satellite-derived free-air gravity anomaly (Sandwell and Smith, 2009), ocean-age isochrons (Müller et al., 1997) and sediment thickness information from seismic reflection data. First within the gravity inversion, the free-air gravity anomaly (g_{fag}) is corrected for the signals from bathymetry (g_b), sediment thickness (g_s) and lithosphere thermal effects (g_t) to calculate the mantle residual gravity anomaly (g_{mra}), where the density for seawater is taken as 1039 kg m^{-3} (Nayar et al., 2016), and the density of the mantle is 3300 kg m^{-3} (Jordan and Anderson, 1974). We take 2850 kg m^{-3} as the density for crustal material based on seismic velocity analysis, drilling results and laboratory experiments from Carlson and Herrick (1990) and Christensen and Mooney (1995).

$$g_{mra} = g_{fag} - g_b - g_s - g_t \qquad (4.1)$$

The mantle residual anomaly is then filtered to remove high-frequency components using a Butterworth filter with a cut-off of 100 km. Using a 3D spectral inversion (Parker 1972), we invert the mantle residual gravity anomaly for Moho topography and in turn the crustal thickness, assuming that the entire signal comes from variations in Moho depth. The incorporation of Smith's Theorem (Smith, 1961) allows us to provide a unique solution for any given set of input parameters. Iteration of the inversion gives an estimation of the lithosphere thinning factor, which is dependent upon the choice of decompression-melt parameterisation.

During rifting and breakup, magmatic material may be added to the crust in the form of extrusives and intrusives. We estimate the thickness of this magmatic addition using a parameterisation of the decompression melting model of McKenzie & Bickle (1988) and White & McKenzie (1989), which is in turn dependent upon the lithosphere thinning factor calculated from the gravity inversion. The lithosphere thinning factor (γ) is defined as:

$$\gamma = 1 - \frac{1}{\beta}$$

(4.2)

Where β is the lithosphere stretching factor (McKenzie 1978).

In this study, we use a melting parameterisation that is representative of an end-member magma-rich margin due to the proximity of the Paraná LIP, which could have resulted in elevated mantle temperatures producing a larger thickness and volume of decompression melting in excess of the average 7 km (White et al., 1992). In the magma-rich parameterisation, decompression melting is expected to produce 10 km thick oceanic crust when maximum thinning is reached (γ = 1.0), with the onset of decompression melting occurring at γ = 0.5. Within the parameterisation of decompression melting thinning factors are corrected for the addition of magma using the melting models of McKenzie & Bickle (1988) and White & McKenzie (1989). Parameterisation of decompression melting is discussed in more detail in Chappell & Kusznir (2008a) and Kusznir et al. (2018), with alternate solutions for modelling other types of rifted margins.

For the Pelotas profile, Moho sensitivity to alternative magmatic parameterisations has no significant effect on the position of the Moho. We have therefore continued to use a magma-rich parameterisation for calculation of Moho depth. Magmatic parameterisation would become important if we wished to derive estimates of thinning factor and continental-crustal-basement thickness along the profile, for which knowledge of the magmatic thickness is required (Chappell and Kusznir, 2008a; Kusznir et al., 2018).

4.3.1 Initial gravity inversion results

Gravity inversion can be used to determine Moho depth across the section. We use it initially to predict Moho depth for two end-member scenarios for the composition of the SDR package (Fig. 4.4). Within the gravity inversion the basement is assumed to be homogeneous, so the results discussed here focus on changes within the SDR package. A discussion of potential basement heterogeneities can be found in Section 4.6.

The first end-member scenario (Fig. 4.4a, c), models the SDR package as entirely compaction-controlled sedimentary material. This corresponds to a top basement surface located at the base of the SDR package (Fig. 4.4a). The second end-member scenario (Fig. 4.4b, d), models the SDR package as entirely incompactable basaltic material, with the top basement surface effectively located at the top of the SDR package (Fig. 4.4b). For both end-member scenarios (Fig. 4.4), the gravity inversion Moho does not consistently match with either seismic Moho candidate. In the sedimentary end-member (Fig. 4.4a, c), the gravity inversion Moho is too shallow when compared against the seismic Moho, while in the basaltic end-member scenario (Fig. 4.4b, d), the gravity inversion Moho matches the seismic Moho in the proximal domain but is too shallow within the distal domain. Additionally, for the sedimentary SDR package scenario a non-physical solution is produced where the gravity inversion Moho rises up into the deepest part of the SDR package (Fig. 4.4a). On the basis of the initial two gravity inversion results, the SDR package composition is likely to be neither fully sedimentary nor fully basaltic.

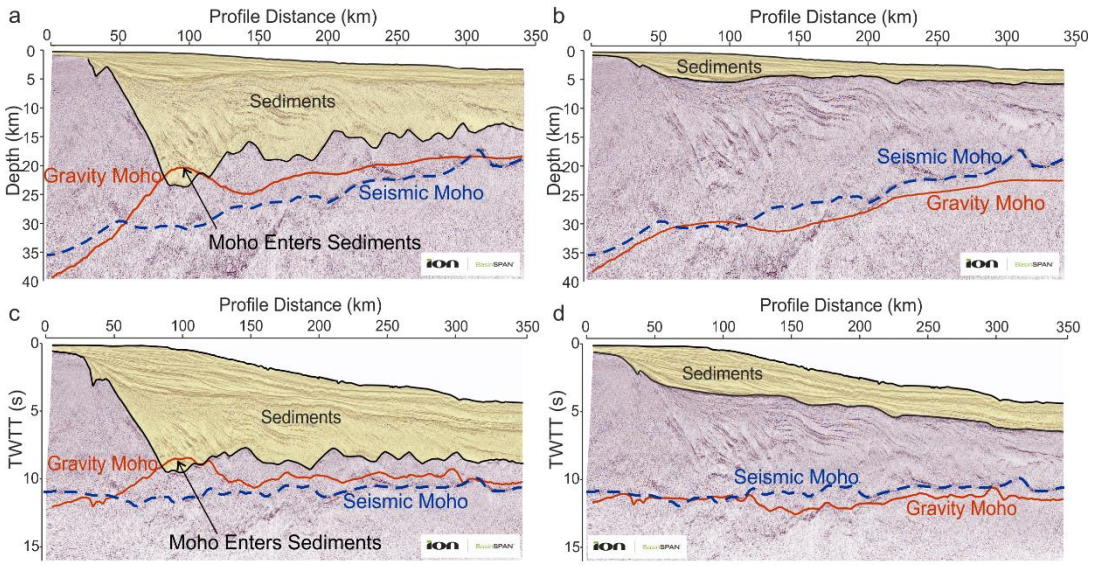

Figure 4.4. Testing end member scenarios for SDR package composition using gravity inversion. a) Gravity inversion Moho (red) in depth resulting from modelling SDR package as sedimentary. Note the gravity inversion Moho inadmissibly entering the overlying sediments. b) Gravity inversion Moho (red) in depth resulting from modelling SDR package as entirely basalt, with an equivalent density to basement. Black arrows highlight possible seismic Moho reflectors c) Gravity inversion Moho (red) in time resulting from modelling SDR package as sedimentary. Note the gravity inversion Moho inadmissibly entering the overlying sediments. d) Gravity inversion Moho (red) in time resulting from modelling SDR package as entirely basalt, with an equivalent density to basement. Black arrows highlight possible seismic Moho reflectors.

Uncertainties within the velocity model used for depth conversion below the SDR package can lead to uncertainties within the results using the PSDM seismic profile. Conversion of the gravity inversion Mohos into the time domain (PSTM profile), by assigning a velocity of 6.31

km s^{-1} to a basement density of 2850 kg m^{-3} (Ludwig et al., 1970) eliminates any depth-conversion uncertainties. Time domain results (Fig. 4.4c, d) once again show a mismatch between the gravity Moho for each scenario and the possible seismic Moho reflectors, as well as a non-physical solution for the sedimentary SDR package end-member.

Our initial results (Fig. 4.4) in both depth and time suggest that the SDR package is most likely to be a combination of both sedimentary and basaltic material, intermediate between the two end-member cases.

4.3.2 Gravity inversion with basalt fraction

Initial gravity inversion results (Fig. 4.4) show that the SDR package is likely to comprise basaltic material interbedded with compactable sediments/volcaniclastics, but the proportion of each is initially unknown. To investigate this further we have explored how varying the proportion of basaltic to sedimentary/volcaniclastic material in the SDR package, the basalt fraction, affects the Moho depth predicted by gravity inversion.

We define the basalt fraction (BF) as the proportion of basaltic material to volcanilastic/sedimentary material, given as a fraction between 0 and 1. The calculated combined density of basalt and compaction-controlled sedimentary/volcaniclastic material is then used within the gravity inversion. Gravity inversions with four basalt fractions at intervals of 0.333 were computed (Fig. 4.5). For example, a basalt fraction of 0.333 represents a mixture of 33% basaltic material and 66% sedimentary/volcaniclastic material.

For the sediment component, we assume the sediments are composed of grains plus fluid in order to estimate bulk density. Using parameters from Sclater and Christie (1980), we estimate bulk density assuming a shaly-sand composition that compacts with depth. We modify this density profile to accommodate the inclusion of a basalt-sediment mix. Firstly, an empirical porosity-depth relationship (Athy, 1930) is assumed:

$$\phi(z) = \phi_0 e^{-cz},$$

(4.3)

Where ϕ is porosity, ϕ_0 is surface porosity, c is the reciprocal of compaction length and z is the depth below the sediment surface (Sclater and Christie, 1980). This approximation leads to a bulk density relationship:

$$\rho = \phi\rho_w + (1-\phi)\rho_{mat},$$

(4.4)

where ρ_{mat} is the matrix density and ρ_w is pore fluid density (Chappell and Kusznir, 2008b). Integration over depth gives average density as a function of depth:

$$\rho_{avg} = \rho_{mat} + \frac{\phi_0(\rho_{mat} - \rho_w)(e^{-cz} - 1)}{cz},$$

(4.5)

Alteration of equation (4.5) to include the presence of a layer of mixed basalt and sedimentary material then gives the following density-depth relationship:

$$\rho_{avg} = (1 - BF)\left[\rho_{mat} + \frac{\phi_0(\rho_{mat} - \rho_w)(e^{-cz} - 1)}{cz}\right] + BF.\rho_b ,$$

(4.6)

in which *BF* is the basalt fraction and ρ_b is the density of basalt.

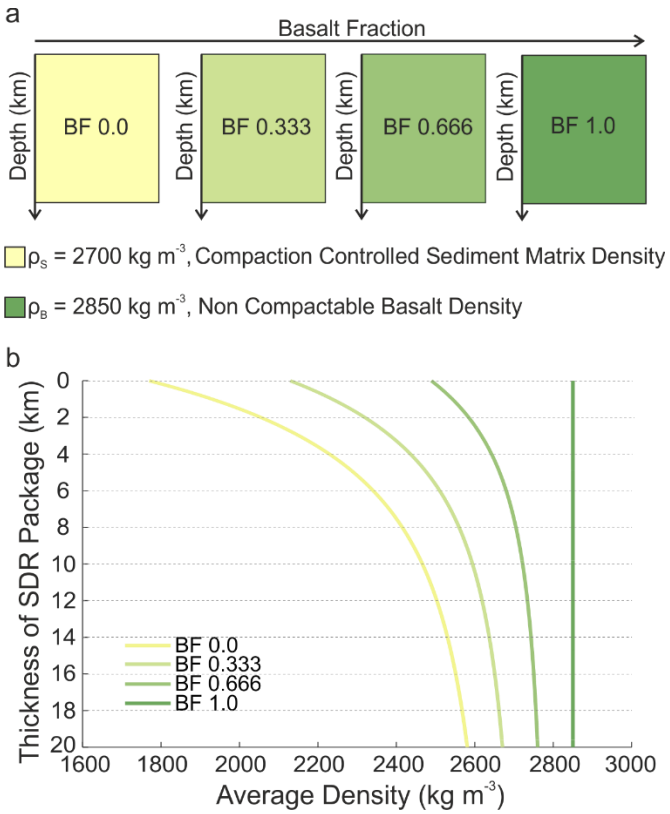

Figure 4.5. The basalt fraction. a) Schematic diagram illustrating the principle of the basalt fraction where a darkening in the colour of the box represents an increase in the proportion of basaltic material (i.e. bulk density). The proportion of sedimentary material to basaltic material is kept constant over all depths. b) Average density of SDR package over entire package thickness, given for each basalt fraction used within the gravity inversion, BF0.0, BF0.333, BF0.666, BF1.0. Densities are displayed for the case where top of SDR package (0 km) is at the seabed.

We assume that the density of basalt is 2850 kg m^{-3} (Moore, 2001) with 0% porosity, i.e. it is non-compactable. For the sedimentary material all compaction parameters follow those detailed in Sclater & Christie (1980), where for shaly-sand sediments, matrix density is given as 2680 kg m^{-3} (rounded here to 2700 kg m^{-3}), surface porosity is 56% and c is 0.39 km^{-1}.

A change in basalt fraction suggests a change in the proportion of basalt to volcaniclastic/sedimentary material, a low basalt fraction suggests there is more material with a lower density such as volcaniclastics/sediments within the SDR package, while a high basalt fraction implies the presence of high-density material such as igneous rocks. SDRs are believed to predominantly contain tholeiitic basalts, which would be represented by a high basalt fraction, i.e. BF 1.0. A low basalt fraction could imply a different mechanism, other than eruptive processes, are at play, in order to form the volcaniclastics/sediments.

4.4 Moho depths from gravity inversion with sensitivity to basalt fraction

The proportion of sedimentary to basaltic material has been investigated using a range of basalt fraction values. Figure 4.6a shows Moho depths calculated from gravity inversion for basalt fractions from 0 to 1, with a 0.333 interval, overlain onto the seismic depth section. An increase in basalt fraction within the gravity inversion, analogous to an increase in bulk density of the SDR package, results in an increase in Moho depth.

As part of this analysis we converted our Moho depth results from the depth domain to the time domain using a basement velocity of 6.31 km s^{-1}, corresponding to a basement density of 2850 kg m^{-3} (Ludwig et al., 1970), in order to account for potential uncertainties in the basement velocity model. Figure 4.6b shows Mohos calculated from the basalt fraction gravity inversions overlain on the pre-stack time-migrated (PSTM) seismic profile together with both shallow and deep seismic Moho candidates.

The shallow seismic Moho candidate lies within the range of the four Moho profiles calculated by the basalt-fraction gravity inversion. This is not the case with the deep seismic Moho candidate, which is too deep to match any of the basalt-fraction gravity inversion Mohos between a line-distance of 50 km and 210 km. Additionally, the deep seismic Moho candidate reaches a maximum TWTT of ~14 s (Fig. 4.5b) which is substantially beyond Warner's Moho guide of ~10 s TWTT (Warner, 1987). As a consequence, the shallow seismic Moho candidate is more realistic and is our preferred seismic Moho interpretation, while the "deep Moho" is likely to be reflectivity from within the mantle. This interpretation is discussed further in Section 4.7.4.

An oceanwards traverse of the time-section (Fig. 4.6b) shows the shallow seismic Moho matches with different basalt-fraction gravity inversion Mohos along the section. At the proximal margin the shallow seismic Moho best fits with a high basalt fraction of 1.0, whereas at the distal margin the shallow seismic Moho best corresponds with a low basalt fraction of 0.333. This implies a changing lithological composition across the SDR package, where basalt fraction (bulk density) decreases oceanward.

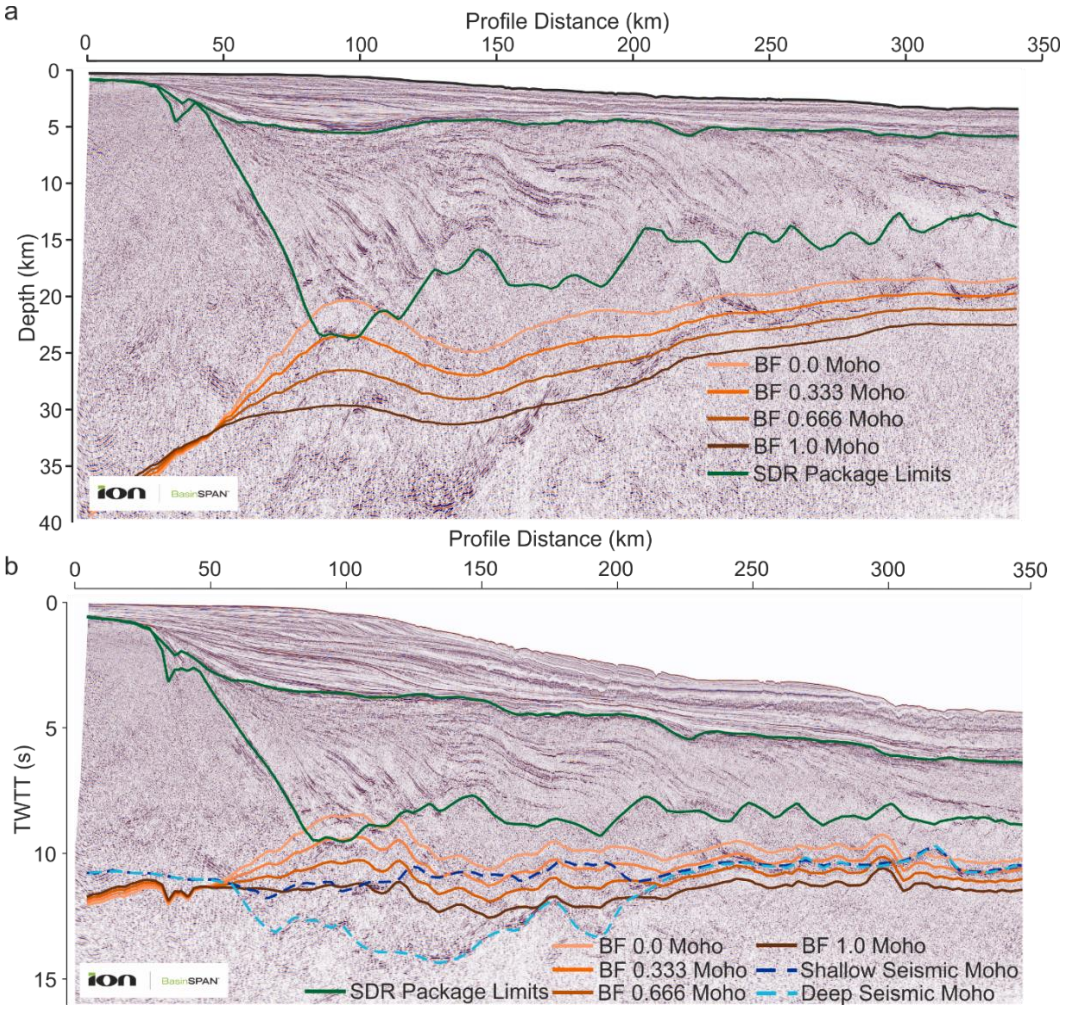

Figure 4.6. a) Basalt fraction gravity inversion Mohos overlain on PSDM seismic reflection profile. SDR package limits shown in green. b) Basalt fraction gravity inversion Mohos and seismic Mohos, converted into TWTT (6.31 km s^{-1} equivalent to 2850 kg m^{-3} basement density), overlain on PSTM seismic reflection profile with seismic Mohos. SDR package boundaries shown in green.

4.5 Lateral variation in SDR package composition from basalt fraction and seismic observations

In order to interpret the composition of the SDR package in more detail we have combined our seismic observations with our basalt fraction results to determine how the composition varies laterally (Fig. 4.7). Based on the changing seismic character of the SDR package,

alongside the potential lateral variation in basalt fraction, the SDR package can be split into three distinct sub-packages (Fig. 4.7a) that are roughly consistent with those made in the interpretation of McDermott et al. (2018). The first (oldest and innermost) sub-package consists of reflectors originating from a single source (in 2D) on the proximal margin. The second sub-package also shows reflectors originating from a single source on the proximal margin but extending across a larger horizontal distance (~150 km). The third sub-package has reflectors that progressively offlap one another in an eastwards direction. These sub-packages, interpreted initially from seismic character, are further delineated by quantifying the lateral variation in basalt fraction.

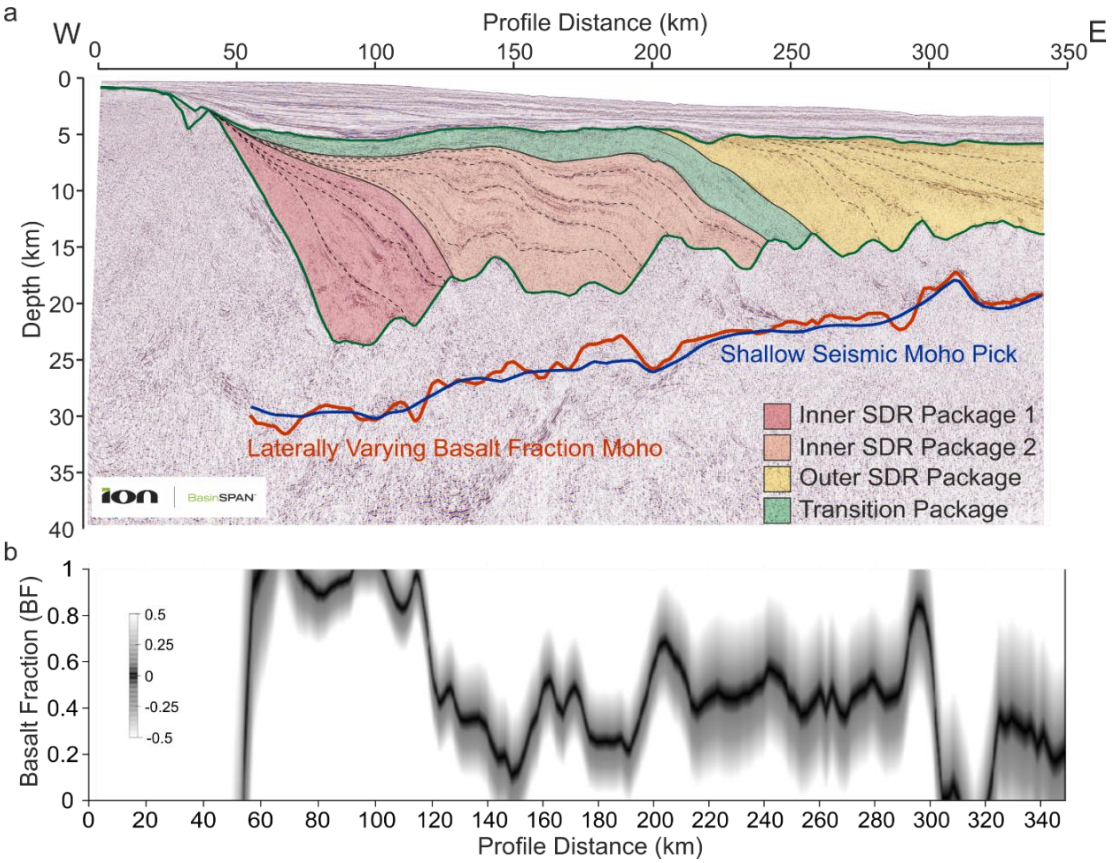

Figure 4.7. a) PSDM showing SDR boundaries (green), sub-package boundaries (solid black), SDR tracings (black, dashed), shallow seismic Moho (dark blue) and laterally varying basalt fraction Moho converted from the time domain (red) by assuming a basement density of 2850 kg m^{-3} and velocity of 6.31 km s^{-1}. b) Lateral variation in basalt fraction calculated by minimising the difference between the basalt fraction Mohos and the shallow seismic Moho in the time domain to avoid depth conversion uncertainties. Black is a difference of zero between the two Mohos, dark grey represents a misfit up to 0.25 s and white areas are a difference of 0.5 s and above.

The lateral variation in basalt fraction is calculated by minimising the difference between the shallow seismic Moho and basalt fraction Mohos in the time domain (Fig. 4.7b), giving the average basalt fraction of the SDR package at that point. The lateral variation in basalt

fraction suggests the presence of three sub-packages within the SDR package, similar to the seismic observations. The first sub-package lies between a line-distance of 55 km and 115 km, with an average basalt fraction approaching 1.0. SDR reflector geometries show a single-point source at ~50 km before fanning out to form a growth wedge. The second sub-package lies immediately outboard of this, with its origin at ~60 km and notably thick flows between 115 km to 210 km, with an average basalt fraction of ~0.45. Within this package, reflectors appear to originate from a single point, similar to inner SDR package 1, but reflectors are more laterally extensive, extending ~150km across the section. The third sub-package is located from ~210 km to the end of the profile and has an average basalt fraction of ~0.55. We have termed these packages, inner SDR package 1, inner SDR package 2 and outer SDR package respectively (Fig. 4.7a). Between inner SDR package 2 and the outer SDR package there is a seismic package that exhibits weak reflectivity and contains no reflectors representative of lava flows. This transitional package (Fig. 4.7a) marks a time gap between the inner and outer SDRs. Conversely, in the outer SDR package, reflectors progressively offlap towards the oceanic domain giving the appearance of lateral migration. Flows are mostly sub-parallel to each other with a slight thickening down dip, similar in appearance to SDRs described by Bodvarsson and Walker (1964). Overall the basalt fraction across the SDR package decreases oceanwards from a maximum of 1.0 in the west to ~0.2 in the east (Fig. 4.7b).

4.6 An alternative test of SDR package density using joint inversion of gravity and seismic Mohos

Our analysis of the lateral variation in SDR package density and basalt fraction using gravity inversion assumes a constant basement density. Here we test the robustness of this assumption using an alternative approach. To achieve this, we use joint inversion of the gravity Moho and the time seismic-reflection Moho (Cowie et al., 2016; Harkin et al., 2019). By comparing the gravity inversion Moho and the seismic Moho in the time domain (Fig. 4.8a), we can calculate the implied lateral variations in the average density of the basement. For the purposes of this test we include the SDRs within the basement (this is equivalent to the case of Fig. 4.4d). Further discussion of the dependency of basement vs. SDR density can be found in the supplementary information.

To achieve the joint inversion, we solve for the density and seismic velocity of the basement, allowing for their lateral variation that results in the gravity Moho matching the seismic Moho in the time domain. We use a linearised Nafe-Drake relationship (Ludwig et al. 1970, V_p =

3.49ρ – 3.46) to link basement density and seismic velocity together as it fits with average oceanic crust seismic velocity and density measurements (Carlson and Herrick, 1990). The lateral variation of basement density affects the depth of the Moho predicted from gravity inversion, while the lateral variation of basement seismic velocity affects the conversion of the gravity inversion Moho from the depth to the time domain. The joint inversion requires an iterative adjustment of both basement density and seismic velocity until convergence is achieved. The advantage of this approach is that it avoids the seismic velocity uncertainties from the basement in the depth seismic reflection section.

The lateral variation in combined basement and SDR density is shown in Figure 4.8. This density, calculated from joint inversion, is the vertically averaged density between top SDRs and seismic Moho. Figure 4.8 shows a significant lateral variation in this density and a

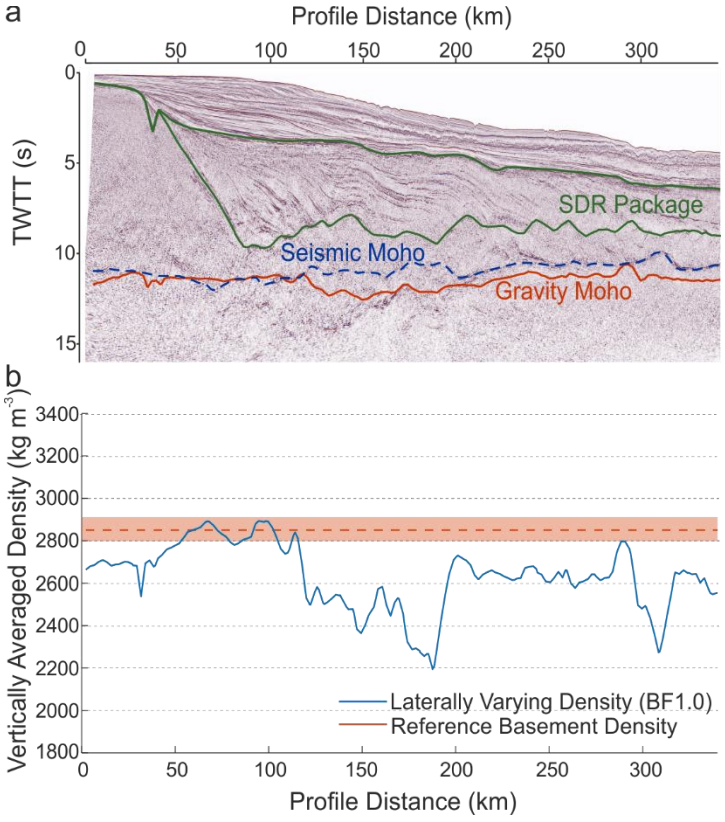

Figure 4.8. Joint inversion of seismic and gravity Mohos, providing an independent test of combined SDR and basement density. a) TWTT seismic section with shallow seismic Moho (blue) and BF1.0 gravity inversion Moho (red) used in the joint inversion. Gravity inversion Moho of BF1.0 is equivalent to top basement located at the top of the SDR package. b) Lateral variation in average basement density resulting from joint inversion using gravity inversion Moho BF1.0 (blue), compared against the initial basement density of 2850 kg m^{-3} (orange), with upper and lower bounds for typical crustal basement also shown (2800-2900 kg m^{-3}).

deviation from 2850 kg m^{-3}, which is the initial density assumed for basement in the gravity inversion. Changing this initial basement density affects the absolute value of the joint inversion densities but does not change the pattern seen in the lateral variation. Further discussion of absolute densities in the joint inversion can be found in the supplementary information.

Between a line-distance of 60 and 120 km, the density between top SDRs and seismic Moho from the joint inversion is high and similar to the initial density of 2850 kg m^{-3} assumed for basement. Further outboard, between 120 and 190 km, this density decreases substantially. At 190 km the density increases but does not reach the assumed value for basement. We interpret this lateral variation in the vertically averaged density between top SDRs and seismic Moho as indicating a lateral variation in the density of the SDR package. We believe this is more likely than the alternative, which is significant lateral variation in the density of the basement. When compared against the lateral variation in basalt fraction (section 4.5, Fig. 4.7) the results are consistent demonstrating that the variation is repeatable and robust. Both techniques display a laterally changing bulk density of the SDR package and the changes within the joint inversion density-profile correspond with the changes shown by the laterally-varying basalt fraction (Fig. 4.7).

4.7 Discussion

Integration of the quantitative analysis, seismic observations and regional context enables us to infer the possible composition of the various SDR sub-packages, as well as the origin and the timing of each package relative to breakup (Fig. 4.9).

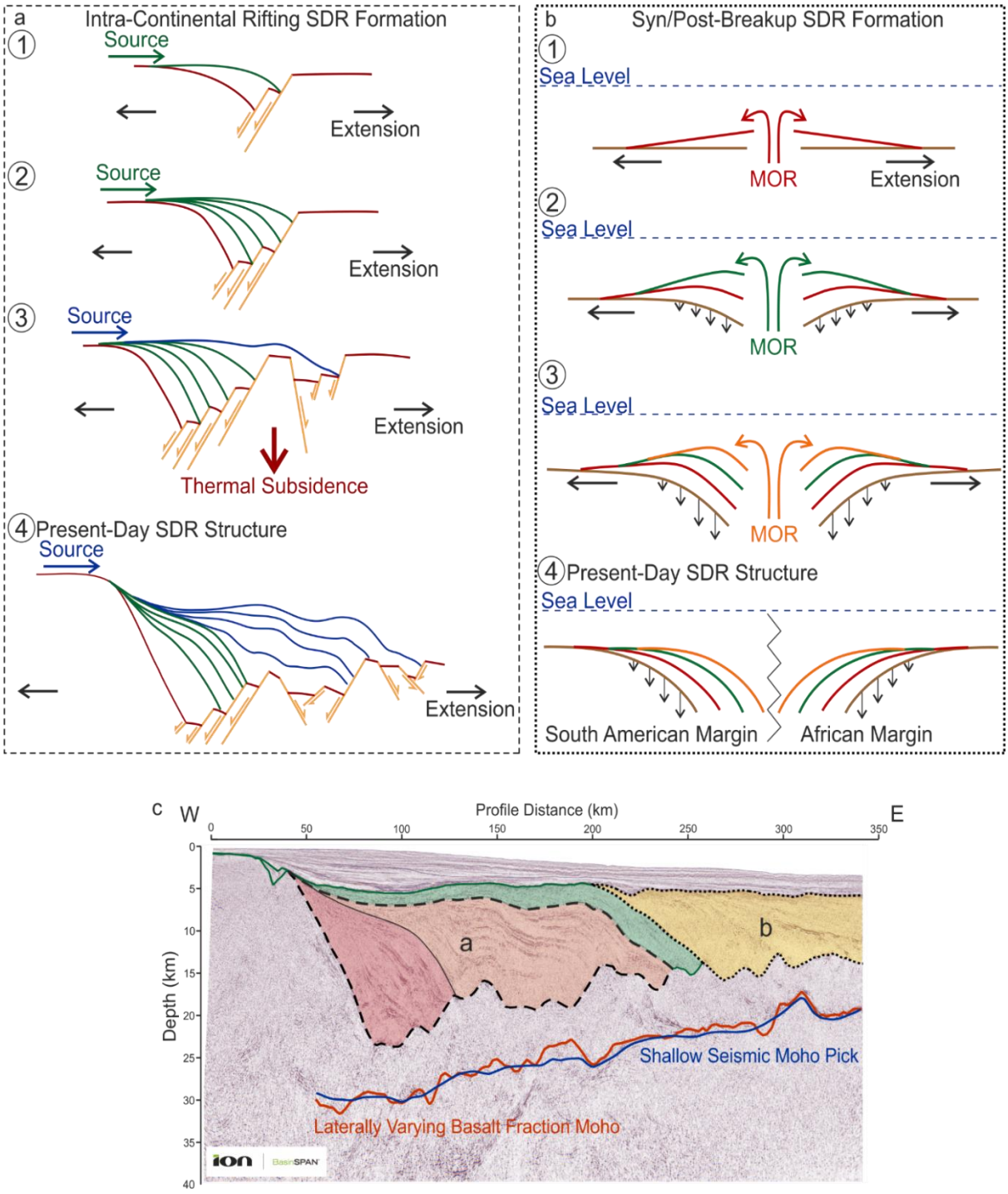

Figure 4.9. SDR formation models for SDR packages on the Pelotas rifted margin. a) Formation of intra-continental rifting SDRs (inner packages). 1) Half graben formation with first extrusive basalt flows infilling accommodation space. 2) Extension continues, and half-graben grows increasing accommodation space. Extrusive material continues to fill accommodation space. 3) Extension forms a horst and graben sequence increasing accommodation space. Thermal subsidence occurs, further increasing accommodation space. b) Syn/post-breakup SDR formation (outer package). 1) Lava flows erupt below sea level from migrating Mid-Ocean Ridge (MOR). 2) MOR migrates due to sea-floor spreading, stopping flows travelling as far, resulting in progressive offlapping. Tectonic flexure from weight of lava flows begins. 3) Flows from MOR form high next to eruption source, with progressive offlapping continuing in the direction of divergence. 4) Present day SDR structure after tectonic and thermal subsidence has occurred. c) PSDM seismic reflection profile with SDR packages, shallow seismic Moho and laterally varying gravity inversion Moho. Intra-continental rifting SDRs denoted by dashed line (a) and post-breakup SDRs shown by dotted line (b).

4.7.1 Inner SDR package 1

Inner SDR package 1 (Fig. 4.7a) has the highest average basalt fraction (approaching 1.0) of the SDR sub-packages identified in this study. This suggests that its composition is 100% basaltic, possibly indicative of subaerial extrusive basaltic lava flows. Seismic reflectors within the package originate (in 2D) from a single-point source at the proximal limit of the package. Downwards termination of the reflectors occurs against a series of landward-dipping normal faults forming a horst and graben structure at the top of basement. The lack of clear internal reflections within the underlying basement, which could be indicative of large magmatic intrusions, suggests that the SDRs are formed by an extrusive process instead of forming via feeder dykes within the basement. Dykes are notoriously difficult to seismically image due to their vertical nature, however any dykes would likely follow the dipping nature of the faults within the basement making them sub-vertical and easier to image. If the source of the SDRs is an extrusive lava flow, then the SDR reflectors might be expected to extend further west instead of pinching out at the edge of the package. A 2 km layer situated at the top of the proximal basement displays different reflectivity to the rest of the basement with some slight layering (Fig. 4.3), suggesting a different material which could be a remnant of the SDR source. The seismic reflection profile is located in the only part of the Pelotas Basin where deposits from the Paraná LIP reach the coastline (Fig. 4.2a), implying a potential continuation of the onshore LIP volcanics offshore into the Pelotas Basin. The majority of the onshore Paraná LIP deposits consist of tholeiitic basalts which can range in density from 2700 kg m^{-3} to 2950 kg m^{-3} (Peate et al., 1992). With a basalt fraction of 1.0 (ρ_{mat}=2850 kg m^{-3}) it is therefore plausible that the dense material of inner SDR package 1 also comprises similar tholeiitic basalts. If inner SDR package 1 is composed of the same material as the erupting Paraná LIP then it is reasonable to assume that they formed contemporaneously, with lava flows from the Paraná extending eastwards into the available accommodation space within active rift basins resulting from extensional faulting. As the formation of the Paraná LIP itself is believed to be associated with regional extension (Hawkesworth et al., 2000), this contemporaneous eruption supports the conclusion from seismic observations that inner SDR package 1 was formed during intra-continental rifting prior to breakup (Fig. 4.9a).

4.7.2 Inner SDR package 2

Inner SDR package 2 (Fig. 4.7a) shows a sharp change in basalt fraction from inner SDR package 1, with an average basalt fraction of 0.45 indicating a higher proportion of less dense material, most probably sedimentary or volcano-sedimentary in origin. One possible source for this could be eroded material from the Paraná LIP interbedded with basalts still erupting

from the onshore Paraná source. Alternatively, the entire package could consist of volcaniclastic sediments (rather than a mix of sediments and lavas) derived from the same active Paraná source as inner SDR package 1. There is evidence of erosion across the seismic reflection profile (Fig. 4.3), however there are no large-scale truncation surfaces suggesting that a mixture of sediments and lavas may be the most reasonable source. Inner SDR package 2 is thought to have been contemporaneous with continued rift-related extension along normal faults which formed additional horst and graben structures outboard of inner SDR package 1 and provided the accommodation space that was filled by an interbedded mix of eroded material and fresh basalts (Fig. 4.9a). As with inner SDR package 1, there are no significant intrusions visible on the seismic reflection profile which might support a dyke-fed origin from directly below, rather than the preferred interpretation of a laterally-extrusive source to the west.

4.7.3 Outer SDR package

The outer SDR package (Fig. 4.7a) has an average basalt fraction of ~0.55 with individual reflectors extending for ~75-100 km. Overall the basalt fraction decreases distally which requires a change in the proportion of basalt to volcaniclastics/sediments to a more volcaniclastic/sediment rich environment which is discussed here. The individual layers within the SDR package thicken down-dip and offlap progressively to the east, suggesting a source from an eastwards-migrating ocean ridge (Palmason and Saemundsson, 1974), i.e. the newly formed Mid-Atlantic Ridge, which, at the time of outer SDR formation, would have been at an embryonic stage and located a short distance to the east of the profile (Fig. 4.9b). A migrating oceanic ridge typically produces MORB-type basalt with an average density of 2850 kg m^{-3} and a thickness of 7km (White et al., 1992). An average basalt fraction of 0.55 implies a bulk density within the SDR package of ~2700 kg m^{-3}. This could be indicative of a mix of basaltic (ρ=2850 kg m^{-3}) and volcaniclastic material, both sourced from the nearby ridge. In particular it could be attributed to the presence of hyaloclastites that have a low density ranging from 2300-2700 kg m^{-3}, with an average density of 2500 kg m^{-3} (Moore, 2001). The presence of hyaloclastites interbedded within SDR flows was recorded on the southeast Greenland margin (Larsen and Saunders, 1998). Formation of hyaloclastites occurs in aquatic environments, where the eruption of magmatic material into water, or flowing laterally into water, results in instantaneous cooling and fragmentation (White et al., 2015). If hyaloclastites are present then this would mean that formation of the outer SDR package had to occur, at least in part, below sea-level, rather than entirely subaerially. Alternatively, the outer SDR package could be formed of basalt flows sourced from the ridge and sediments

from onshore sources. However, on the seismic reflection profile (Fig. 4.3) all flows in the outer SDR package are truncated with no evidence of sediment transportation from the west.

Flows within this package would have erupted from the embryonic Mid-Atlantic ridge, stacking on top of each other and causing a thickening of the flows closest to the spreading centre (Fig. 4.9b, Pindell et al., 2014 fig. 9f). Migration of the spreading centre would result in new flows offlapping the older flows in the direction of migration (Fig. 4.9b). Eruption from an embryonic Mid-Atlantic ridge implies syn-breakup formation of the outer SDR package.

4.7.4 Nature of the crustal basement, the deep reflector and the transition package

The techniques used within this study are not able to define the nature of the basement underlying the SDR package (continental, oceanic or transitional). Rather they provide constraints on the thickness and density of the basement, which can then be interpreted in terms of crustal type. Interpretations can also be made based on our understanding of the geometry and formation of the SDR package. If the inner SDR packages were formed by syn-rift volcanism this would imply the presence of underlying continental crust. Our gravity Moho indicates a maximum basement thickness of 10 km below the inner SDR packages, which has been defined as the upper limit of hyper-extended continental crustal thickness (Pérez-Gussinyé et al., 2006). This is consistent with the inner SDR packages forming on continental crust that has undergone extension and thinning during intra-continental rifting. The outer SDR package has been interpreted as syn-breakup, similar to SDRs described by Bodvarsson and Walker (1964) and others. Syn-breakup SDRs imply formation during, and perhaps immediately after, breakup meaning these SDRs must be emplaced over something other than continental basement, possibly magmatic or transitional basement. The seismic reflection profile does not display typical Penrose oceanic crust properties, i.e. distinct layers 2 and 3 (White et al., 1992), so we suggest that the outer SDR package has formed over transitional basement where continental crust has been heavily intruded by sills and dykes before transitioning eastwards into new oceanic basement.

The deep reflector visible on both PSTM and PSDM profiles (Figs. 4.3, 4.6, & 4.7) was initially interpreted as a possible seismic Moho (Fig. 4.3, Stica et al., 2014, fig. 7). We now consider it to be a possible reflection from within the mantle, below the actual Moho. In section 4.3.1, the deep reflector has been shown to be an unrealistic Moho candidate as it occurs at TWTTs approaching 14 s (Fig. 4.6). At line-distance ~210 km, however, the deep reflector joins the shallow seismic Moho, coincident with the location at which the inner SDR packages terminate. It is therefore possible that the deep reflector has a magmatic origin related to

the formation of the inner SDR packages and depicts the juxtaposition of two different mantles, one that is depleted and one that is more fertile, e.g. harzburgite and lherzolite (Picazo et al., 2016). The compositional differences between the two types of mantle would result in a density contrast allowing them to be visible on seismic sections. Similar deep mantle reflectors representing palaeo-melt channels/fronts have been noted elsewhere, for example offshore Tanzania (Sauter et al., 2016).

The transition package (Fig. 4.7a), marks a time gap between the inner and outer SDR packages. No reflectivity indicative of SDR flows is visible within the package and reflectors marking the top of the package are discontinuous. The transition package thickens eastwards and pinches out towards the west, similar to the origin of both inner SDR packages. Stratigraphically, the transition package lies above inner SDR package 2 and is included within the basalt fraction calculation. This could affect the basalt fraction results for the sub-packages in particular inner SDR package 2. However, the discontinuous reflectors that depict the top of the package, alongside the geometry of the package can be interpreted as an extrusive lava flow which would be from the same source as the inner SDR packages. Composition of the transition package is therefore assumed to be similar to the inner packages.

4.8 Summary

Using bulk-density determined from gravity inversion and interpreted seismic characteristics the SDR package in the Pelotas Basin has been shown to contain two distinct sub-packages; the inner SDR package and the outer SDR package. The inner SDR package can be further divided into an inner SDR package 1 (older) and inner SDR package 2. Average basalt fraction results for each package are used as a proxy for composition, representing the proportional mix of basaltic and sedimentary/volcaniclastic material. Inner SDR package 1 is considered to consist entirely of extrusive basaltic material. Inner SDR package 2 is considered to consist of extrusive basaltic material with a high proportion of sedimentary/volcaniclastic material. The outer SDR package may contain a high proportion of volcaniclastics with subsidiary basaltic material.

The composition of each individual package, together with their regional context on the Atlantic margin, is used to infer the origin of the evolving SDR sequence (Fig. 4.9). The location of the seismic profile adjacent to the onshore LIP of the Paraná, the growth structures seen within the inner SDR packages and the horst-graben structure of top basement suggests the origin for the inner SDR packages is similar to the syn-rift origin of the

onshore Paraná. The reflectors of the outer SDR package show progressive offlapping to the east and have an average basalt fraction of ~0.55. They are thought to have been sourced from an embryonic eastwards-migrating Mid Atlantic Ridge, lying immediately east of the profile at the time of their formation.

Finally, the timing of each package relative to breakup can be determined from the assumptions made about their origin. If the inner SDR packages are contemporaneous with the Paraná LIP and top basement displays horst-and-graben structures, then the inner SDRs would have formed during intra-continental rifting. In contrast, the outer SDR package, sourced from the embryonic Mid Atlantic ridge, will have formed during breakup and the initial stages of sea-floor spreading. Our results show that the SDRs imaged on the Pelotas profile record two different stages in the evolution of the South Atlantic margin, separated by the transitional package, from intra-continental rifting at the proximal margin through to breakup and subsequent sea-floor spreading at the distal margin. Symmetry of SDRs is only required after the formation of the transitional package, at which time breakup began. The extraordinary SDRs presented in this study are a result of their positioning, just offshore from the Paraná LIP, which has enabled the juxtaposition of the outer SDRs against the inner SDRs that are otherwise absent on the margin along strike (Stica et al., 2014).

Our results, gathered from seismic observations and quantitative techniques, lead to the conclusion that both mechanisms for SDR formation (Fig. 4.1) have operated in the Pelotas Basin (Fig. 4.9), indicating that the two mechanisms are not exclusive of each other. Instead, we have shown that SDRs produced by each mechanism were generated during different stages of continental rifting and breakup. Classification of similar SDR sequences worldwide could help develop our overall understanding of the evolution of magma rich margins.

Supplementary Information

Discussion of absolute densities from joint inversion of gravity and seismic data

For inner SDR package 2, the joint inversion of gravity and seismic data gives very low densities of ~2400 kg m^{-3} (Fig. 4.8), for the combined SDRs and basement. If we assume basement density remains constant at 2850 kg m^{-3} as average continental and oceanic crust have similar densities (Carlson and Herrick, 1990; Christensen and Mooney, 1995), then extremely low densities are required within the SDR package which could be considered unreasonable. As such, we discuss our assumption that basement composition remains

constant across the profile. Gravity inversion results suggest crustal thickness beneath the inner SDRs is <10 km. If the inner SDRs formed during intra-continental rifting this would suggest the basement is continental. Continental crust that is less than 10 km thickness is regarded as hyper-extended continental crust, which is typically embrittled and heavily faulted, often containing fluids (Pérez-Gussinyé et al., 2006). This would result in a lower basement density, which could contribute towards the low average density seen in the joint inversion.

Alternatively, the low densities could be a result of the density-velocity relationships used within the joint inversion, as they are derived for general bulk compositions of lower crustal and oceanic material (see Appendix A.4), which have different compositions to the upper crustal material interpreted on the Pelotas margin. The absolute values of density and velocity are therefore subject to uncertainty. Despite this uncertainty in the absolute values, the relative lateral change in density and velocity remains robust. The joint inversion calculates the average density and velocity of the material between top SDRs and seismic Moho by locally adjusting density and velocity along the profile. This produces profiles of laterally varying density and velocity where any lateral variations are relative to the surrounding area.

If the basement composition changes laterally, then the relative changes in average density within the joint inversion could pinpoint where the basement composition changes significantly. At a line-distance of ~200 km, the average density changes from very low to high, suggesting a significant change in composition of either the SDRs, basement or both. As this point corresponds with the end of inner SDR package 2 and the point at which the deep reflector joins the seismic Moho, it is likely that this density change represents the termination of continental crust and intra-continental forming SDRs and the onset of decompression melting associated with seafloor spreading.

Chapter 5

Palaeobathymetry and density analysis of the seaward dipping reflectors on the Pelotas rifted margin

This chapter is a manuscript currently under preparation for submission to Petroleum Geoscience. This study investigates the depositional environment of extrusive magmatism on the Pelotas margin. The authors of the manuscript are currently Caroline Harkin (first author), Christopher Cooper and Nick Kusznir. Data analysis and drafting of the manuscript was undertaken by Caroline Harkin, with discussion and interpretation of results done in collaboration with Christopher Cooper and Nick Kusznir.

Paper Abstract

The addition of large volumes of extrusive magma in the form of seaward dipping reflectors (SDRs) is a common feature observed at magma-rich rifted margins. Drill holes, potential field data, seismic reflection data, seismic refraction data and onshore analogues have all been used to further our understanding of the formation processes associated with seaward dipping reflectors. However, there is a difference between SDR formation models as some suggest subaerial formation while others suggest subaqueous formation. In this study we determine palaeobathymetries using 2D flexural backstripping, decompaction and reverse thermal subsidence modelling, average SDR density using joint inversion of seismic and gravity data, and the depositional environment of the SDRs using seismic observations. We examine two end-member compositions for the SDR package, sedimentary/volcaniclastic and volcanic, to provide constraints on our palaeobathymetry estimates. We additionally investigate the sensitivity to dynamic uplift as the Pelotas margin formed contemporaneously with the Tristan da Cunha mantle plume.

Our results suggest the SDRs on the Pelotas margin can be split into three distinct sub-packages, each with a different depositional environment. For each sub-package, the palaeobathymetry predictions differ. The innermost package has a palaeobathymetry prediction above sea level, the middle package palaeobathymetry predictions vary from above sea level to below sea level depending on the end-member compositions, and the outer package has a palaeobathymetry prediction that is below sea level. The average density of each package varies greatly, the highest average density is found in the innermost package,

the middle package has the lowest density and the outer package has an intermediate density. We interpret these results to indicate the innermost package was formed subaerially, the middle package formed within a temporally changing environment, from subaerial to subaqueous, and the outer package formed subaqueously. Combining gravity and seismic data can help determine sub-package composition alongside joint inversion densities, particularly for the outer package where the mid-range density is ambiguous. By calculating density profiles and matching them with our gravity, seismic and joint inversion results we propose that the outer package is composed of an equal mix of hyaloclastites and basalt flows.

5.1 Introduction

The extension of continental crust during rifting and breakup often causes decompression melting of underlying lithosphere producing extrusive volcanic material, commonly in the form of seaward dipping reflectors (SDRs). The depositional environment of SDRs is often disputed due to conflicting observational evidence. As such the majority of formation models suggest subaerial formation while a smaller minority suggest subaqueous formation. Knowing where SDR packages form, i.e. above sea level or below sea level, enables informed decisions to be made about potential hydrocarbons as well as using that knowledge to constrain the evolution of a margin during breakup.

In this study, we investigate the depositional environment of the Pelotas rifted margin SDRs, located in the South Atlantic. We use 2D flexural backstripping, decompaction and reverse thermal subsidence modelling to give predictions of palaeobathymetries during breakup. Here we use palaeobathymetries as an indicator of the depositional environment of the seaward dipping reflectors on the Pelotas rifted margin, i.e. a subaerial or a subaqueous environment. In addition to our palaeobathymetry predictions, we investigate the lateral density variations of the SDR package using the joint inversion of gravity and time seismic Moho data. By integrating both techniques we have established a set of conditions that when fulfilled suggest subaerial formation of SDRs. Identification of subaqueous SDR formation is difficult as densities of magmatic rocks formed underwater are more variable than those formed subaerially. To combat this we calculate density profiles of different combinations of subaqueous magmatic rocks and compare against our density analysis results to find a reasonable match.

5.1.1 The Pelotas Basin

Situated offshore southern Brazil is the Pelotas Basin (Fig. 5.1), previously classified as a magma-rich rifted margin due to the large volumes of magmatic material found there (Stica et al., 2014). The Pelotas Basin is part of the South Atlantic rifted margin that demonstrates both magma-poor and magma-rich characteristics. Immediately north of the Pelotas Basin is the Santos Basin, which also contains magmatic material, and further north of the Pelotas and Santos basins are the magma-poor basins of Esperito-Santos and Campos (Stica et al., 2014). East of the Pelotas Basin lies the Rio Grande Rise, an area of thickened crust composed predominantly of igneous material, formed during the breakup of Gondwana.

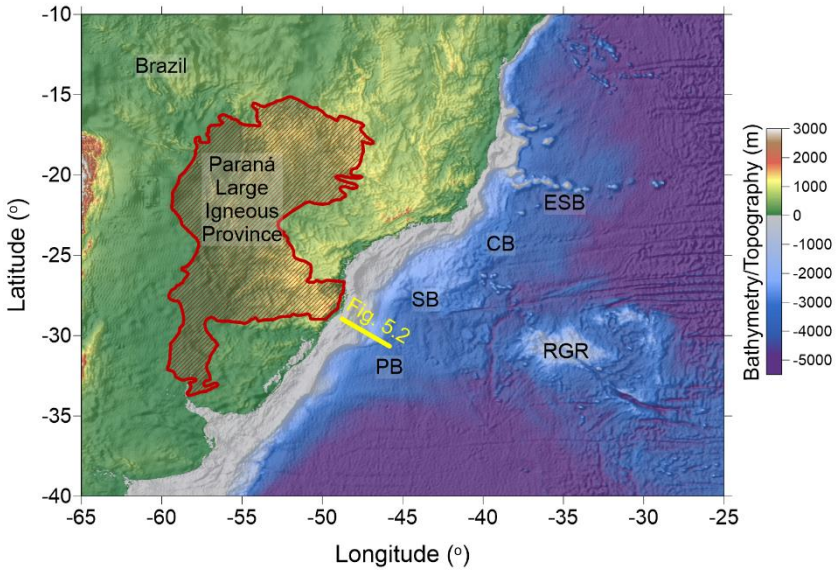

Fig. 5.1. Bathymetry/topography map of southern Brazilian rifted margin with free air gravity shaded relief overlain. CB: Campos Basin; ESP: Esperito-Santos Basin; PB: Pelotas Basin; RGR: Rio Grande Rise; SB: Santos Basin.

Formation of the southern Brazilian margin occurred during the Early Cretaceous with dated magnetic anomalies suggesting an age of 120-130 Ma (Granot and Dyment, 2015; Heine et al., 2013; Pérez-Diaz and Eagles, 2014). Immediately onshore of the Pelotas Basin and the seismic reflection profile, lies the Paraná Large Igneous Province (LIP), a large area of tholeiitic basalts covering 1.5×10^6 km^2 in South America (Hawkesworth et al., 1992). Additional deposits can be found in Africa as part of the Etendeka province (Paul R. Renne et al., 1996). Formation of the Paraná LIP was synchronous with the formation of the South Atlantic rifted margins, with the main eruptive phase occurring between 133 Ma to 130 Ma but related volcanism continued through to 124 Ma (Hawkesworth et al., 1992; Mantovani et al., 1988; Turner et al., 1994). Both the Paraná and Etendeka LIPs have been associated with the Tristian da Cunha plume, and subsequently the Walvis Ridge and Rio Grande Rise,

both of which are believed to be hotspot trails (Coffin and Eldholm, 1992; Connor and Duncan, 1990; Torsvik et al., 2009; White and McKenzie, 1989).

5.2 Seismic observations

The seismic line examined within this study is located within the Pelotas Basin along an anomalous bathymetric high known as the Arc de Torres, just offshore of the Paraná LIP deposits. Our interpretation of the depth seismic reflection section is shown in Figure 5.2a which has also previously been interpreted by Stica et al (2014). McDermott et al. (2018) also gave interpretations of other seismic lines within the Pelotas Basin. No seismic refraction data were available for analysis in this study.

A layer of post-rift sediments approximately 3 km thick, covers the entire seismic section. These post-rift sediments appear to downlap onto the underlying SDRs. Below the post-rift sediments and above top basement is the SDR package. Within the SDR package, individual reflectors are visible, all dipping towards the East and the distal area of the seismic section. There is a lateral variation in the geometry of the individual reflectors (black dashed lines, Fig. 5.2) and they can be grouped into three separate sub-packages based on those changes, highlighted in Figure 5.2a as dashed black lines. The first sub-package is the oldest and innermost package, with reflectors that appear to originate from a single westwards source. Compared with other sub-packages, the reflectors within this package are not laterally extensive at ~75 km wide but they are vertically extensive reaching depths of 23 km. The second sub-package also shows reflectors originating from a single westwards source, however, these reflectors extend much further laterally and the internal structure of the reflectors appear to imitate the underlying top basement surface giving it a hummocky appearance. The final sub-package is different from the previous two packages as the reflectors progressively offlap one another eastwards giving the package a migratory appearance.

The seismic Moho is well defined in the distal margin giving a basement thickness of ~6 km. Towards the proximal margin, the seismic Moho remains roughly parallel with top basement with a slight increase in basement thickness to 10 km under the most proximal SDRs.

As well as the lateral variations in SDR geometry, there is a lateral variation in SDR package thickness. Figure 5.2b shows how SDR thickness varies over the entire profile. The innermost package is the thickest with a maximum thickness of 16.5 km, while a minimum thickness of 6.5 km is seen within the outer package. The averages for the innermost package, the middle

package and the outer package are 14.5 km, 11 km and 7.75 km respectively. For comparison, SDR thickness on the Argentinian margin reaches a maximum of ~8.5 km (Paton et al., 2017).

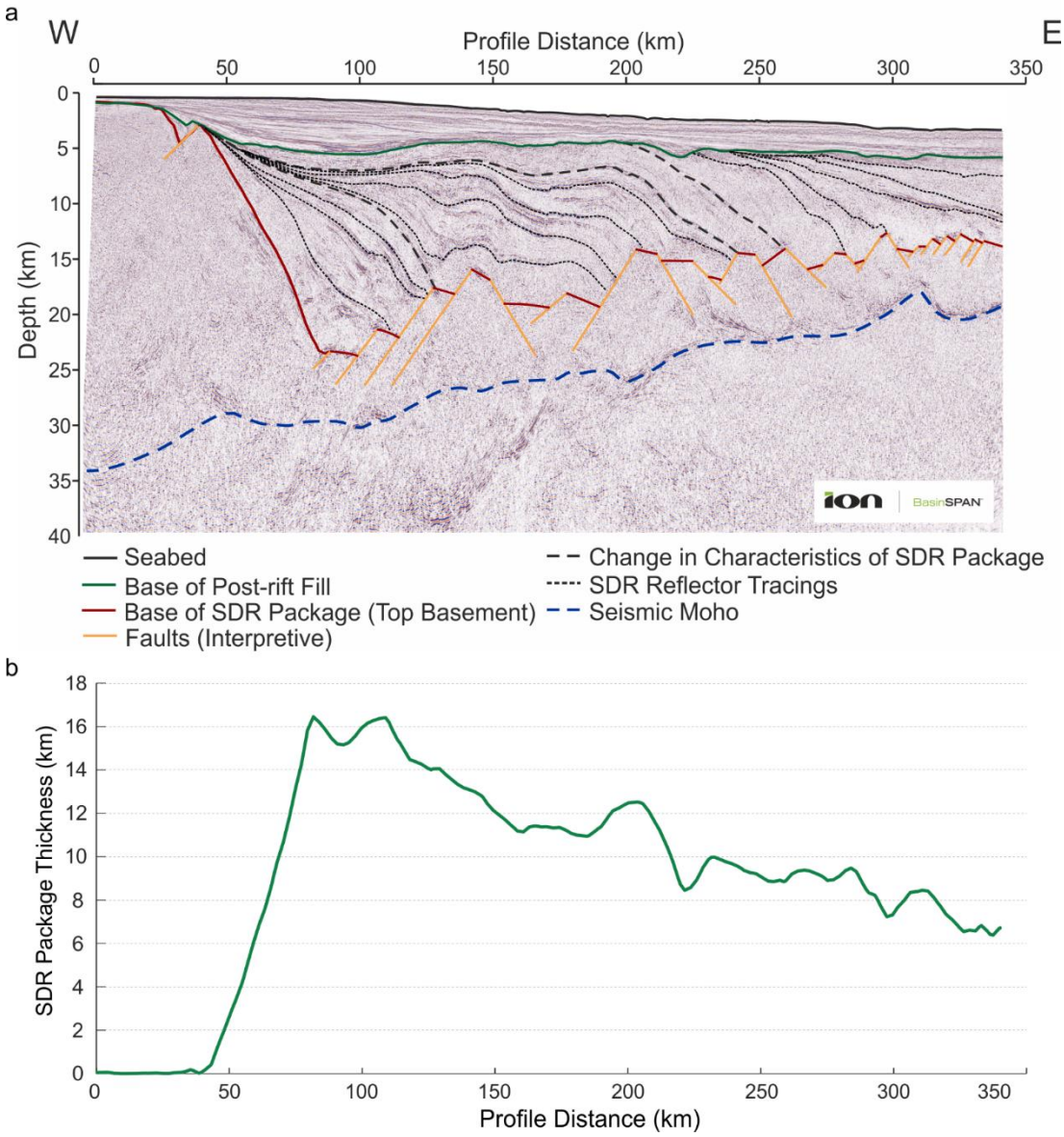

Figure 5.2. a) Seismic interpretation of seismic reflection line, location shown in Fig. 5.1. b) SDR package thickness, taken from base of post-rift sediments to top of basement across the entire profile.

5.3 Subaerial vs. subaqueous SDR formation

Previous models of SDR formation have suggested both subaerial and subaqueous formation with conflicting evidence from observational data such as drill holes and seismic reflection surveys. For example, along the Southeast Greenland rifted margin (Larsen, 1994b; Larsen and Saunders, 1998) and on the Vøring margin, offshore Norway (Sinton and Duncan, 1998), drilled SDR sequences display erosional tops of basalt lava flows suggesting subaerial exposure but they also contain volcaniclastic deposits such as hyaloclastites which require

subaqueous formation (Frolova, 2008). With volcaniclastic deposits often being minor within SDR wedges, the majority of SDR formation models favour subaerial formation in order to explain the larger proportion of drilled basalts in many SDR wedges.

Two commonly used SDR formation models are the volcanic faulting model and the volcanic loading model, summarised by Buck (2017), both of which favour subaerial formation but use different mechanisms to create packages of SDRs. In the volcanic faulting model (Gibson and Love, 1989; Quirk et al., 2013), large landward dipping faults in continental crust allow SDRs to form subaerially via feeder dykes. By contrast, in the volcanic loading model, first suggested by Bodvarsson and Walker (1964) and Palmason and Saemundsson (1974), dykes at a spreading centre feed the subaerial lava flows. Successive loading results in isostatic compensation and subsidence of the flows giving them their dipped appearance. These SDRs have the potential to be subaqueous as they are believed to form at the onset of seafloor spreading.

Some models combine subaerial and subaqueous formation to explain observations of basalts and subaqueous volcaniclastics. The volcanic loading model is similar to the SDR formation model proposed by Hinz (1981), however Hinz's model features both subaerial and subaqueous SDR formation. The oldest SDRs form subaerially while the younger SDRs form subaqueously as successive loading results in plate flexure similar to the volcanic loading model, pushing the flows underwater. Subsequent lava flows then form subaqueously. Skogseid and Eldholm (1987) show that unconformities and truncations exist within the SDRs on the Vøring Plateau as a result of changing subsidence rates, implying that the depositional environment of SDRs can change. McDermott et al. (2018) used velocity analysis to suggest the SDRs within the Pelotas Basin initially formed subaerially but had some interaction with water resulting in eventual subaqueous formation.

5.4 Methodology

5.4.1 Palaeobathymetry analysis

Palaeobathymetry predications are calculated through reverse post-rift thermal subsidence modelling that incorporates the flexural isostatic response to the removal of overlying sedimentary layers and decompaction of any underlying layers (Cowie et al., 2015a; Kusznir et al., 1995; Roberts et al., 1998).

The calculation of palaeobathymetries follows a set workflow defined by Roberts et al. (1998), which is as follows:

1. Removal of the water layer and calculation of the flexural isostatic response.
2. Removal of the top stratigraphic unit and decompaction of the underlying layers according to pre-set compaction parameters.
3. The flexural isostatic response to the removed layer is calculated.
4. Reversal of thermal subsidence in the form of thermal uplift, calculated using a 2D form of the McKenzie (1978) post-rift thermal subsidence model (Roberts et al., 1998). Within the 2D McKenzie model estimates of the stretching factor (β) are required which are calculated from the lithosphere thinning factor produced in the gravity inversion.
5. If needed, a correction is made for any long-term eustatic sea-level changes.
6. A cross section of the profile is produced that is isostatically balanced with the top stratigraphic unit removed.
7. Steps 1-6 are repeated for remaining stratigraphic units.

During decompaction, the density and porosity of layers are adjusted so that they correspond to the newly calculated depth. To do so we must know the compaction parameters which are surface porosity (ϕ_0), matrix density (ρ_{mat}) and compaction length (c). We derive these compaction parameters by integrating Athy's relationship (1930) and a bulk density-porosity relationship over depth (z) to give:

$$\rho_{avg}(z) = \rho_{mat} + \frac{\phi_0(\rho_{mat} - \rho_{water})(e^{-cz} - 1)}{cz} \quad (5.1)$$

We model the SDR package as two simple end-member compositions and calculate the palaeobathymetry estimates for both to give upper and lower bounds on our estimates. The first end-member assumes the entire SDR package is composed of shaly-sand sedimentary material whose compaction is depth-dependent. As the SDRs are extensive, it is possible that they constitute a large proportion of sedimentary material with minor volcanic deposits that produce the strong reflectivity. The second end-member assumes the entire SDR package is composed of basaltic material that is non-compactable. Each end-member composition requires certain compaction parameter values calculated using equation 5.1 and given in Table 5.1.

Composition	Surface Porosity	Matrix Density (kg m^{-3})	Compaction Length (km^{-1})
Sedimentary	0.56	2700	0.39
Basalt	0	2850	0.39

Table 5.1 – End-member compaction parameters.

Dynamic topography exists globally and as such, the cross section used as a starting point within the palaeobathymetry analysis is subject to said present day dynamic topography. Any palaeobathymetry restoration of the present day cross section will therefore contain a signal representative of present day dynamic topography. Not only does dynamic topography vary spatially, but it also varies temporally. In the past, dynamic topography may have been different to the present day dynamic topography, which can only be determined using additional information such as reliable palaeobathymetry observations. A discrepancy existed between the palaeobathymetry restoration and the palaeobathymetry observations could represent past dynamic topography, however, it is also possible that the discrepancy exists due to missing information such as syn-tectonic crustal thinning. Despite this uncertainty in determining dynamic topography, we can still investigate the effects of dynamic topography. Here we investigate the effect of a range of dynamic uplifts from 0 km to 1 km.

5.4.2 Density analysis using joint inversion of gravity and seismic Moho data

Gravity anomaly inversion (Alvey et al., 2008; Chappell and Kusznir, 2008a; Cowie et al., 2015b; Greenhalgh and Kusznir, 2007; Harkin et al., 2019; Kusznir et al., 2018) gives estimates of Moho depth using a 3D spectral inversion of free air gravity (Sandwell and Smith, 2009), bathymetry (Smith and Sandwell, 1997), ocean-age isochrons (Müller et al., 2008) and sediment thickness from seismic reflection data. Within the gravity anomaly inversion, lithosphere thermal effects are corrected for (Chappell and Kusznir, 2008a) and Smith's Theorem (Smith, 1961) is invoked to provide a unique solution for the chosen input parameters. To do so, constant densities are assumed for seawater (1039 kg m^{-3}), the basement (2850 kg m^{-3}, averaged from Carlson and Herrick, 1990; Christensen and Mooney, 1995) and the mantle (3300 kg m^{-3}, Jordan and Anderson, 1974). 2D sediment thickness is obtained using seismic reflection data and sediment density is compaction controlled assuming a shaly-sand composition using the compaction parameters determined by Sclater and Christie (1980).

Joint inversion of gravity inversion and time seismic reflection Moho data investigates lateral variations in combined basement and SDR density and seismic velocity. The joint inversion

works by comparing the seismic Moho and the Moho from gravity inversion in the time domain and assumes any differences between the two are due to heterogeneities within the combined basement and SDR package. Working in the time domain avoids uncertainties that may be present in the velocity model used for depth conversion. We solve for the difference between the two Mohos in the time domain by matching the gravity inversion Moho to the seismic Moho. For the conversion of the gravity inversion Moho from the depth domain to the time domain we assume that the sediment thickness derived from seismic reflection interpretation and depth conversion is correct. Crustal thickness is calculated using the distance between top basement and the gravity inversion Moho, converted into two-way travel time (TWTT) as an interval TWTT. This interval is added to the seismic interpretation of top basement in the time domain to give the gravity inversion Moho in TWTT. Seismic velocity and basement density are linked through a linearised Nafe-Drake relationship (Ludwig et al., 1970, $V_p = 3.49\rho - 3.46$). We adjust the density and seismic velocity of the combined basement and SDRs, which in turn affects the depth of the gravity inversion Moho and subsequent conversion from depth to two-way travel time. Iterative adjustment of seismic velocity and density will result in the convergence of the seismic Moho and gravity inversion Moho.

5.5 Results

5.5.1 Palaeobathymetry results

To predict palaeobathymetries at the time of SDR formation, post-rift sediments must be removed, decompacted and isostatically compensated for, while post-rift thermal subsidence is reversed. Figure 5.3 shows the stages involved when determining palaeobathymetry predictions for both end-member compositions.

First, seismic observations and gravity inversion results are used to produce a present-day crustal cross section (Fig. 5.3a). The next stage is the removal of post-rift sediments and decompaction of the underlying SDR package according to the compaction parameters for each end-member composition (Figs. 5.3b-c). Decompaction of the SDR package results in a palaeo-surface for the sedimentary end-member composition (Fig. 5.3b) that is ~1 km shallower than the palaeo-surface for the basalt end-member composition (Fig. 5.3c).

In order to reverse the thermal subsidence along the margin, knowledge of lithosphere thinning is required which is obtained using thinning factors from the gravity inversion (see section 5.4.2, Fig. 5.3d-e). Modelling the SDR package as sedimentary is equivalent to placing top basement at the base of the package while modelling the SDR package as basaltic is

equivalent to placing top basement at the top of the package. This affects the thinning factors as the basalt end-member (Fig. 5.3e) appears to have thicker crust due to the SDR package being combined with the underlying basement. For the sedimentary end-member composition (Fig. 5.3d), full stretching and thinning of initial crust so that it is removed (γ=1.0) occurs at line-distance 75 km and remains at one throughout the profile. For the basalt end-member composition (Fig. 5.3e), full stretching and thinning (γ=1.0) only occurs between a line-distance 75 km and 110 km. The thinning factor then varies between 0.6 and 0.9 across the rest of the profile, averaging 0.8 overall.

Reversing the thermal subsidence for each end-member composition using thinning factors from gravity inversion gives predictions of palaeobathymetry. For the sedimentary end-member composition (Fig. 5.3f), results show a positive palaeobathymetry of ~ 500 m up to a line-distance of 200 km, beyond which a negative palaeobathymetry of -500 m to -1500 m can be seen. For the basalt end-member composition (Fig. 5.3g) the prediction of palaeobathymetry is negative across the whole profile. For the proximal SDRs, an prediction of -500 m is given while a palaeobathymetry prediction of -1500 m to -2500 m is given for the most distal SDRs.

The palaoebathymetry methodology does not account for dynamic topography as it restores surfaces to a present day isostatic datum which may not be the same as when the margin formed. However, we can add dynamic topography to our palaeobathymetry predictions. The Pelotas margin evolved when the Tristan da Cunha mantle plume was active which could have resulted in a large amount of dynamic topography. We add 500 m and 1 km of dynamic topography to the margin for both end-member compositions (Fig. 5.3h-i). For the sedimentary end-member composition (Fig. 5.3h), dynamic topography of 500 m does not affect where the SDRs become subaqueous, but dynamic topography of 1 km means that the SDRs remain subaerial up to a line-distance of 275 km. For the basalt end-member composition (Fig. 5.3i), dynamic topography of 500 m makes the most proximal SDRs subaerial while 1 km of dynamic topography makes the SDRs subaerial up to a line-distance of 150 km.

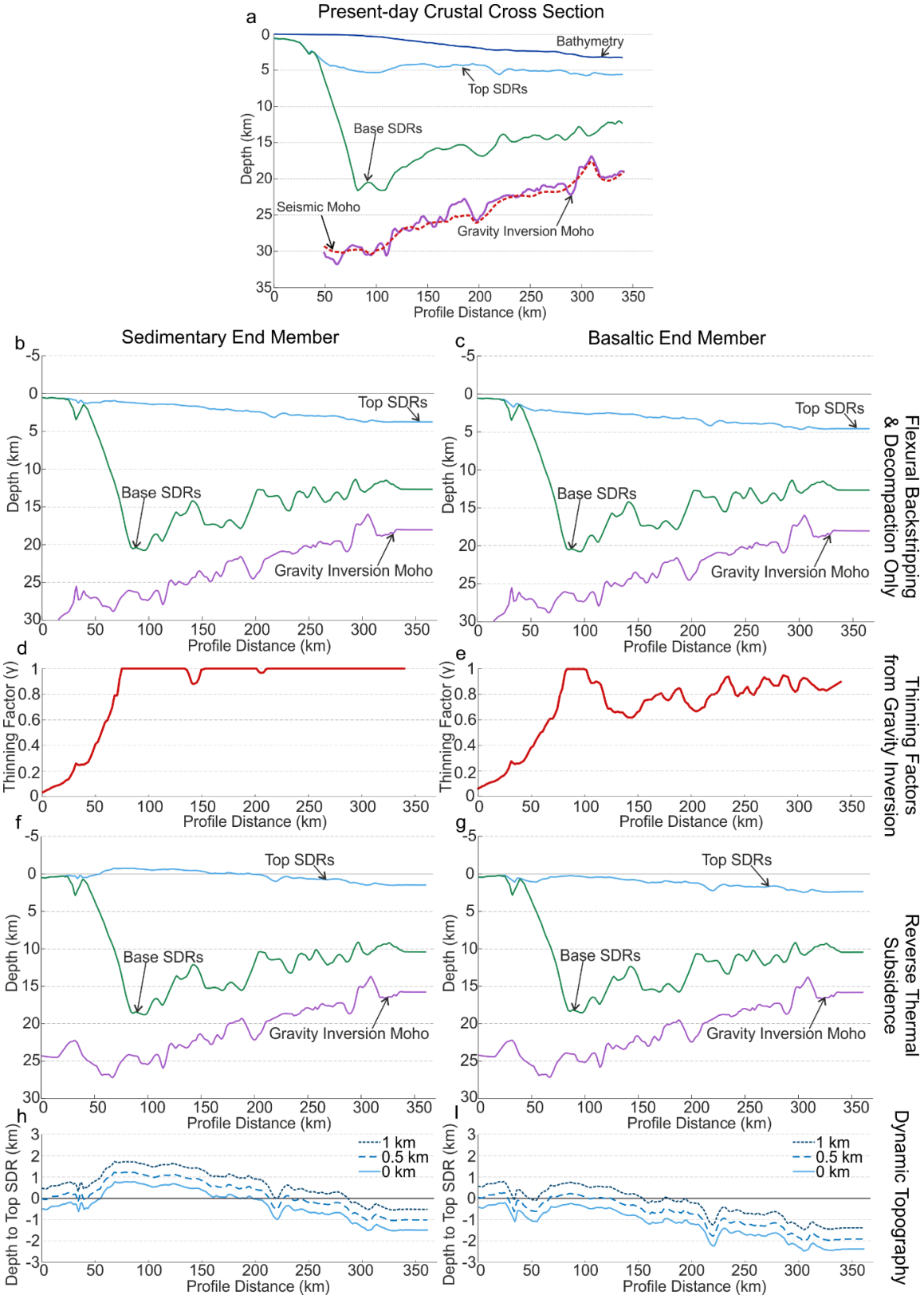

Figure 5.3. Palaeobathymetry analysis to top of SDR package. a) Present day crustal cross section. b) Flexural backstripping of post-rift sediments and decompaction of the SDR package using shaly-sand compaction parameters. c) Flexural backstripping of post-rift sediments and decompaction of the SDR package using basalt compaction parameters. d) Thinning factor from gravity inversion sedimentary end-member. e) Thinning factor from gravity inversion for basalt end-member. f) Palaeobathymetry estimate from reversal of thermal subsidence for sedimentary end-member using thinning factor in d). g) Palaeobathymetry estimate from reversal of thermal subsidence for basalt end-member using thinning factor in e). h) Addition of 500 m and 1 km of dynamic topography to sedimentary end-member SDR palaeobathymetry surface. i) Addition of 500 m and 1 km of dynamic topography to basalt end-member SDR palaeobathymetry surface.

5.5.2 SDR density analysis results

Previous studies of continental and oceanic crustal densities (Carlson and Herrick, 1990; Christensen and Mooney, 1995) show that the average densities are 2830 kg m^{-3} and 2860 kg m^{-3} respectively. Although there is some variation between the density of continental and oceanic crust, it is minimal and as such, we assume the basement density remains constant and we attribute any lateral changes in combined basement and SDR density to changes within the SDR package.

Seismic observations suggest the presence of three sub-packages within the main SDR package (Figs. 5.2a & 5.4a); inner SDR package 1, inner SDR package 2 and the outer SDR package. The seismic Moho (Fig. 5.2a) used within the joint inversion is also shown on Figure 5.4a.

Figure 5.4b shows a profile of lateral density variations across the seismic section produced using the joint inversion of gravity and time seismic Moho data. Inner SDR package 1, between a line-distance of ~50-120 km, predicts SDR bulk density to be 2850 kg m^{-3}, which is equivalent to extrusive basaltic material. Throughout the rest of the profile, SDR bulk density appears to be lower than expected for normal basaltic material (2800 – 2900 kg m^{-3}, Moore, 2001). SDR bulk density is lowest in inner SDR package 2, between a line-distance of 120 km and 200 km, with an average of 2400 kg m^{-3}, and in the outer SDR package, from a line-distance of 200 km to the end of the profile, SDR bulk density averages 2600 kg m^{-3}.

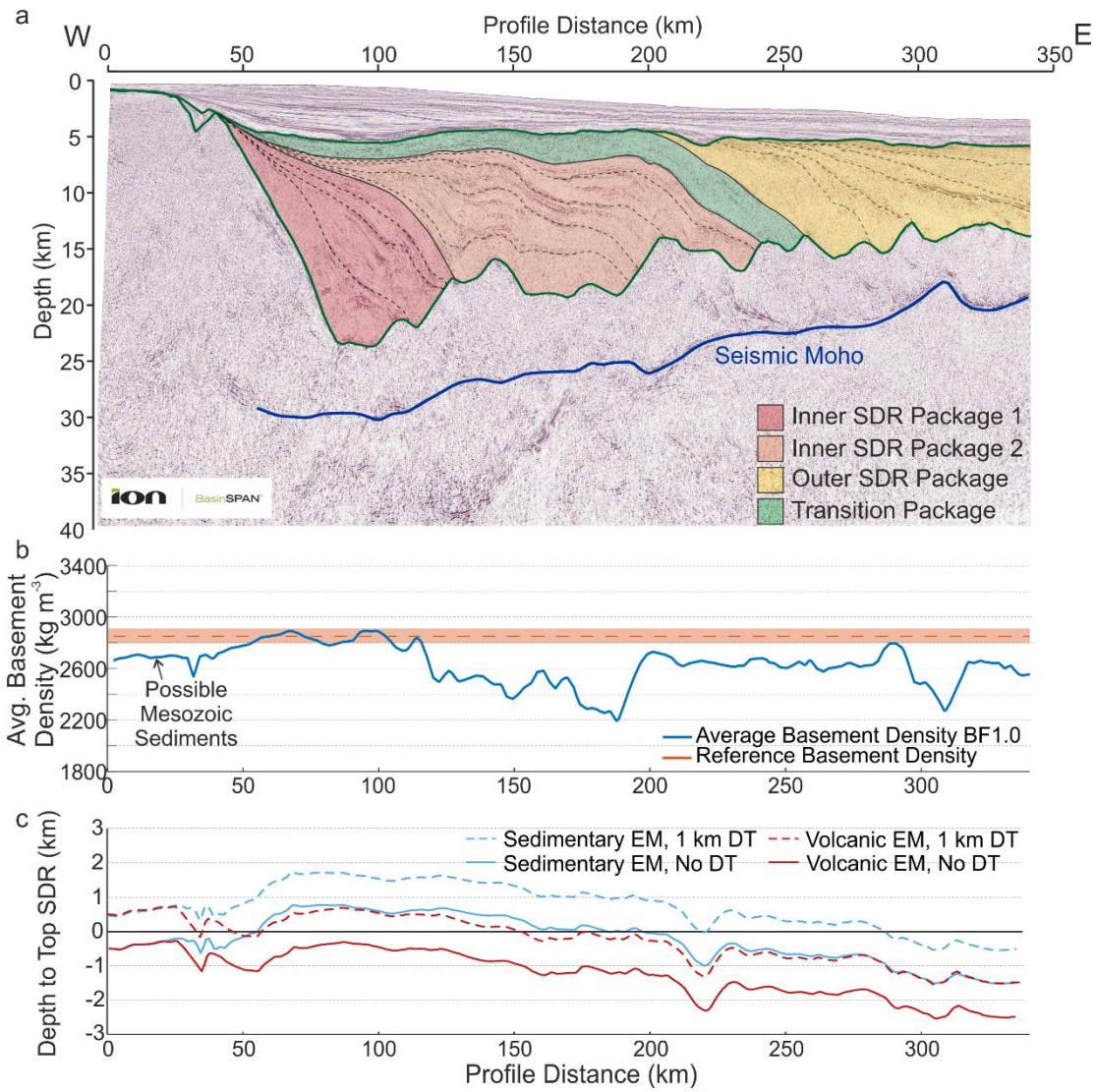

Figure 5.4. a) Seismic observations showing SDR sub-packages; inner SDR package 1, inner SDR package 2 and outer SDR package as well as Moho from gravity inversion and the seismic Moho. See Fig. 5.2 for more detail. b) Lateral variations in SDR package density from joint inversion of gravity and time seismic reflection Moho. c) Palaeobathymetry estimates to top of SDRs for sedimentary end member (EM), (blue) and volcanic end member (red) with no dynamic topography, DT, (solid lines) and 1 km of dynamic topography (dashed lines).

5.6 Discussion

Seismic observations show lateral changes in SDR geometry that have resulted in the SDR package being split into three separate sub-packages (Fig. 5.4a). From proximal to distal the packages are: inner SDR package 1, inner SDR package 2 and the outer SDR package with the average thickness for each package varying from 14.5 km, 11 km and 7.75 km respectively. Lateral density variations from joint inversion can also be split into three separate sub-packages that correspond to each SDR sub-package (Fig. 5.4b). Palaeobathymetry predictions for both end-members, with and without 1 km of dynamic topography; show a change in depositional environments between the inner and outer packages, with the inner packages

mostly subaerial while the outer package is subaqueous. Within this discussion, we integrate our seismic observations, joint inversion results and palaeobathymetry predictions to interpret the composition and depositional environment of each sub-package.

5.6.1 Inner SDR Package 1

Palaeobathymetry predictions for inner SDR package 1 (Fig. 5.4c) suggest subaerial formation for both end-member compositions when a minimal amount of dynamic topography (500 m) is included and the average density from joint inversion for the package is 2850 kg m^{-3}, a density that is equivalent to extrusive basaltic material. This density combined with seismic observations that show a single point source from the west, knowledge that the Paraná LIP is immediately to the west, onshore of the seismic line (Waichel et al., 2013) and *a priori* information that the majority of SDRs around the world consist of tholeiitic basalts, we assume that inner SDR package is composed of subaerial tholeiitic basalts sourced from the Paraná LIP. The presence of the Paraná LIP during margin formation is evidence of an active mantle plume, i.e. the Tristan da Cunha plume. Tristan da Cunha would have created uplift in the mantle, hence the application of 500 m dynamic topography. The exact magnitude of dynamic topography is not known; however, 500 m is a reasonable estimate based on other studies of plumes and resultant dynamic topography (Holbrook et al., 2001). The average thickness of the package is 14.5 km with maximum and minimum thicknesses of ~16-11 km respectively; suggesting that a thick pile of SDRs with at least 10 km thickness is required for subaerial formation.

5.6.2 Inner SDR Package 2

Palaeobathymetry analysis and joint inversion of gravity and seismic Moho data present conflicting results for inner SDR package 2. Palaeobathymetry predictions for the sedimentary end-member composition are above sea level while palaeobathymetry predictions for the volcanic end-member composition are below sea level. Joint inversion results for inner SDR package 2 give the lowest density of all the sub-packages at an average of ~2400 kg m^{-3}. The reflectors in inner SDR package 2 appear to grow from a single westwards source, similar to the reflectors in inner SDR package 1. An average low density coupled with the seismic character of the package is consistent with a mixed volcaniclastic and basalt composition or a larger proportion of sedimentary material. Proximity of the seismic line to the Paraná LIP means the Paraná's tholeiitic eruptions could create the basalt flows while the source of the volcaniclastics/sediments could be eroded material from Paraná onshore deposits. The contrasting palaeobathymetry results could be an indication of a changing environment, possibly from subaerial to subaqueous formation. Previous SDR

formation models, such as the formation model from Hinz (1981), display a temporally changing environment. Our results do not specify if subaerial or subaqueous formation occurred first, however, tectonic and thermal subsidence of the margin is likely to have occurred after initial formation as Paraná igneous activity would have reduced and extension of the margin continued. It should be noted that our results are for end-member compositions so alternatively, if inner SDR package 2 is composed of both sediments and basalt, then the palaeobathymetry prediction would be shallow subaqueous, <500 m.

5.6.3 Outer SDR Package

For the outer SDR package, palaeobathymetry predictions range from 2200-2500 m below sea level. Even with the addition of dynamic topography, the outer SDRs remain below sea level suggesting they formed subaqueously. It is likely that the outer SDRs underwent tectonic subsidence after formation, as the flexure of the flows would have created internal fractures and extension. However, this would not generate a palaeobathymetry ~2 km below sea level so subaqueous formation is needed. Joint inversion of seismic and gravity Moho data suggests the average density of the outer SDR package is ~2600 kg m^{-3}, which is considerably lower than the average density range of oceanic crust (Carlson and Herrick, 1990). Drilling of other offshore SDR packages from SE Greenland and the Vøring Plateau suggests that SDRs are often a mixture of tholeiitic basalts and lower density volcaniclastics (Larsen and Saunders, 1998; Mutter et al., 1982).

In a subaqueous environment, volcaniclastic rocks take the form of hyaloclastites (Frolova, 2008), which have been found in drilled SDR wedges (Larsen and Saunders, 1998). Hyaloclastite flows vary in structure vertically, at the base usually lies a massive jointed basalt and at the top lies fine grained hyaloclastites (Planke et al., 2000). This variation in vertical structure creates an impedance contrast visible on seismic reflection profiles. Hyaloclastite flows therefore appear as large bedded structures, similar to sediments on deltaic systems (Planke et al., 2000). Hyaloclastites form from the quenching of lava erupted into water resulting in glassy fragments that settle and form high-porosity layers (Bonatti, 1965; White et al., 2015). Hyaloclastites have the ability to travel long distances as evidenced in Sida, offshore Greenland, provided there is a high eruption rate (>1-2 m^3 s^{-1} m^{-1}) and low hydrostatic pressure during formation (Bergh and Sigvaldason, 1991). Compaction and burial of hyaloclastites first produces palagonite as the pyroclastic sediments are cemented and then smectite with other secondary minerals in the cement, such as zeolite and calcite, as the rock is slowly buried (Bonatti, 1965; Frolova et al., 2005). This change in hyaloclastite composition can result in a rapid decrease in porosity, from 50-60% in weakly consolidated

material, to 15-25% in rocks that have a mixed cement composition, but more often porosity remains at 30-40% in rocks with pore-type smectite cement (Frolova, 2008). A Hawai'ian drill core (see fig. 2a, Moore, 2001) shows the depth-dependent density variation in hyaloclastite samples. According to the samples from the Hawai'ian drill core, our palaeobathymetry prediction of 2200-2500 m for the outer SDRs suggests a hyaloclastite density range of 2200-2800 kg m^{-3}**.** This fits with our average density from joint inversion of 2600 kg m^{-3}, however, drilled SDR wedges show a mixed composition of volcaniclastics and basalt flows, so a singular composition of hyaloclastites is unlikely.

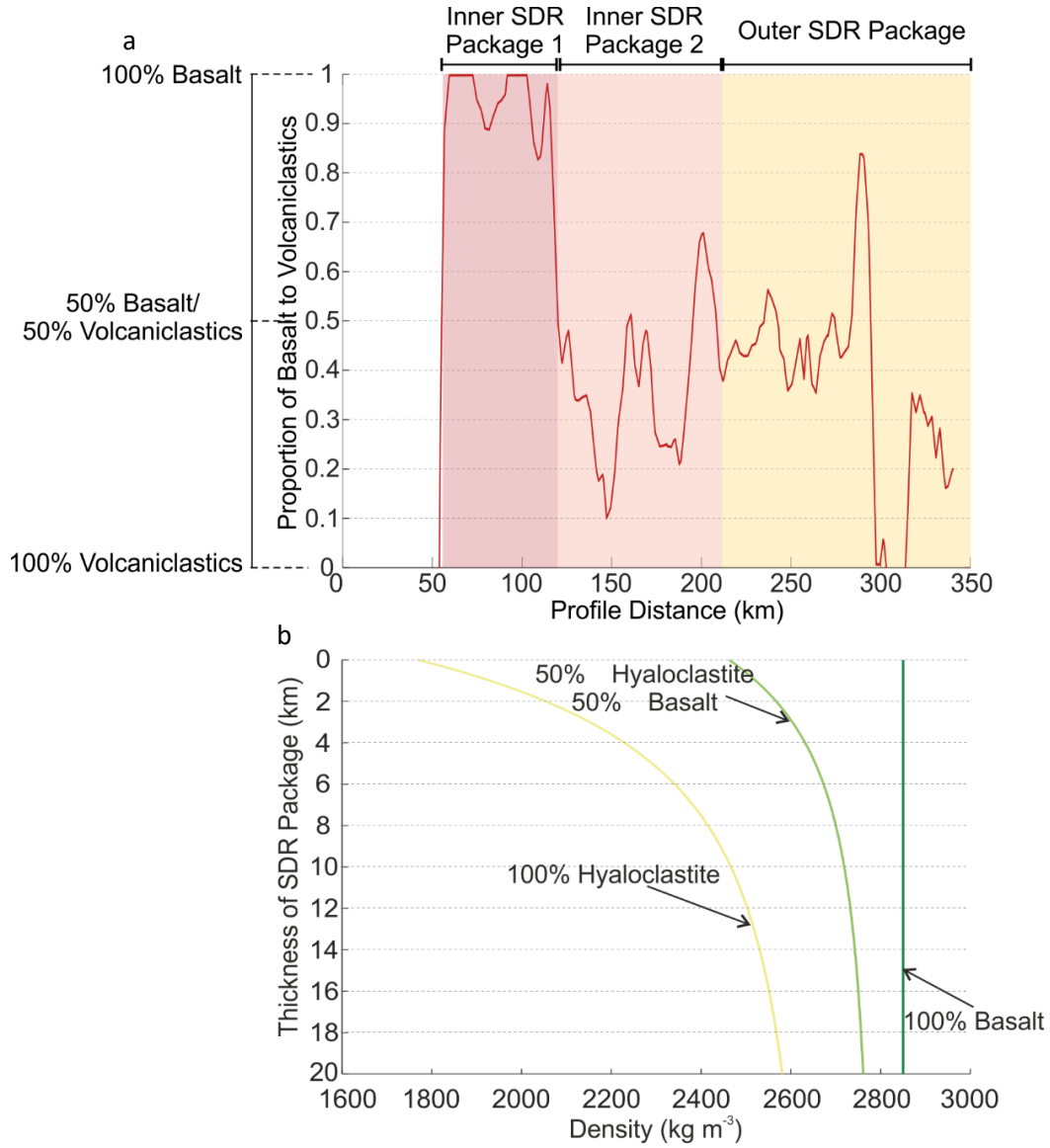

Figure 5.5. a) Comparison of seismic and gravity data for end-member compositions of volcaniclastic and basalt, to determine likely mixture of volcaniclastics and basalt. b) Density profiles for SDR package calculated for various compositions, entirely volcaniclastic (hyaloclastite), 50:50 mix of hyaloclastite and basalt and entirely basaltic.

We can estimate the proportion of hyaloclastites to basalt flows using gravity and seismic data. By modelling the SDR package as 100% volcaniclastic and 100% basaltic within a 3D gravity anomaly inversion, we can compare the results for each against our seismic observations. Where they agree is our best estimate of SDR composition. Figure 5.5a shows the likely mixture of volcaniclastics (i.e. hyaloclastites) and basalt within the SDR package. The average proportion of hyaloclastites: basalt for the outer SDR package area is ~50:50, for which we calculated a density profile assuming compaction-controlled hyaloclastites and non-compactable basalt (Fig. 5.5b). The average thickness of the outer SDR package is ~7 km, taken from Figure 5.2b, which gives an average density of ~2650 kg m^{-3} using the 50:50 density profile in Figure 5.5b. Gravity inversion and joint inversion produce similar average densities for the outer SDR package, suggesting a composition consisting of equal amounts of hyaloclastites and basalt flows is reasonable.

5.7 Summary

Combined palaeobathymetry analysis and joint inversion of seismic and gravity Moho data of the SDRs on the Pelotas rifted margin, give an insight into the depositional environment at the time of breakup. Lateral variations in both palaeobathymetry predictions and bulk density results show the SDR package can be split in three distinct sub-packages; inner SDR package 1, inner SDR package 2 and the outer SDR package.

Inner SDR package 1 exhibits subaerial palaeobathymetry predictions for both end-member compositions when dynamic topography is included. Internal SDR bulk densities are high, in excess of 2850 kg m^{-3} for the whole package and seismic observations show reflectors originating from a single point source to the west. Altogether, our results and observations favour subaerial deposition of inner SDR package 1.

Palaeobathymetry predictions and joint inversion results are conflicting for inner SDR package 2. Palaeobathymetry predictions once again suggest subaerial formation when minimal estimates of dynamic topography are included. However, densities from joint inversion are low for the whole package averaging ~2400 kg m^{-3}, which could be indicative of subaqueous formation. The difference between the two techniques could be the result of a multi-phase deposition where inner SDR package started forming subaerially and eventually changed to subaqueous formation.

For the outer package, palaeobathymetry predictions suggest subaqueous formation and the average density from joint inversion is low at ~2600 kg m^{-3}, which could indicate the presence

of volcaniclastics or sedimentary material. Drilled SDR sequences are often a mixture of basalt flows and hyaloclastites, which form subaqueously. A comparison of seismic data and end-member composition gravity data suggests the outer SDR package is composed of a 50:50 mixture of basalt and volcaniclastic material, which equates to an average density of 2650 kg m^{-3}, consistent with the average density from joint inversion.

This work demonstrates how using observations and quantitative results can determine the depositional environment of SDRs. For example, if an SDR package exceeds 10 km thickness and has positive palaeobathymetry predictions as well as average densities of ~2850 kg m^{-3}, then it is likely that the SDRs formed subaerially. When determining if SDRs formed subaqueously, our results are more ambiguous due to low densities attributed to water-forming volcaniclastics or a higher proportion of sedimentary material. However, if an SDR package is less than 10 km thick, has negative palaeobathymetry predictions and has a low average density then it is likely that the SDRs formed subaqueously.

Chapter 6

The formation of the Southeast Greenland rifted margin by distributed magma-rich plate divergence

This chapter is derived from a manuscript currently under preparation for submission to Earth, Planetary and Science Letters. The authors of this manuscript are Caroline Harkin (first author), Nick Kusznir and Hans Christian Larsen. The aim of this study was to investigate the asymmetry of the conjugate Southeast Greenland and Hatton Bank margins by determining basement composition along the Southeast Greenland margin. Caroline Harkin carried out data analysis and interpretation. Nick Kusznir and Hans Christian Larsen helped draft the manuscript and provided useful discussion, particularly with formation mechanisms. There are supplementary figures to accompany the manuscript, which can be found at the end of the chapter.

Paper Abstract

Formation of the conjugate rifted margins of Southeast (SE) Greenland and Hatton Bank in the North Atlantic occurred contemporaneously with the evolving North Atlantic Igneous Province, and as such are classified as magma-rich rifted margins. The SE Greenland margin ocean-continent transition (OCT) has a broad region (~150 km) of anomalously thick crust, previously interpreted as igneous crust, that is asymmetric when compared to its conjugate, the Hatton Bank margin. Explanations for this asymmetry have invoked asymmetric magma-rich sea-floor spreading. An alternative hypothesis is that the SE Greenland margin OCT consists of a wide region of hyper-extended continental crust sandwiched between extrusive and intrusive magmatic material, which is absent on the conjugate Hatton Bank margin. Using data from the SIGMA seismic survey, we investigate the OCT structure on the SE Greenland margin to determine if continental or igneous crust is present. We integrate gravity inversion, joint inversion of seismic and gravity data and seismic velocity analysis to determine crustal thickness, basement seismic velocity and basement density across the margin. Overall, our results favour the presence of thick igneous crust on the SE Greenland margin rather than thinned hyper-extended continental crust sandwiched between extrusive and magmatic material. We interpret this crust, with up to 15 km thickness, as very thick oceanic crust. This interpretation of the SE Greenland margin pushes the location of the continent-ocean

boundary inboard. Rather than invoking asymmetric sea-floor spreading to explain the asymmetry of the SE Greenland and Hatton Bank margins, we suggest that the asymmetry results from a two-stage process consisting of first, distributed magma-rich plate divergence and oceanic crustal accretion followed by plate boundary localization and more normal seafloor spreading.

6.1 Introduction

The opening of the Northeast (NE) Atlantic during the Paleogene formed the conjugate magma-rich rifted margins of Southeast (SE) Greenland and Hatton Bank (Fig. 6.1). These margins exhibit strong asymmetry with a ~150 km wide region of 10-15 km thick crust between characteristic continental and oceanic crust on the SE Greenland margin that is absent on the Hatton Bank margin. The presence of seaward dipping reflectors (SDRs), onshore flood basalts and the nearby Iceland plume, all suggest the 10-15 km thick crust is igneous. However, previous velocity analyses conducted on the SE Greenland margin (White & Smith, 2009) have suggested the presence of thinned continental crust within the thick magmatic crust. In addition, SE Greenland and Hatton Bank display asymmetry that is similar to conjugate magma-poor rifted margins such as Iberia-Newfoundland (Sutra et al., 2013). This suggests that SE Greenland could have undergone a similar evolution, whereby the thick magmatic crust is composed of hyper-extended continental crust sandwiched by extrusive and intrusive magmatic material as a result of the interplay between tectonic and magmatic processes.

In this study we investigate the structure and composition of the thick magmatic crust on the SE Greenland margin using data from the SIGMA seismic survey (Hopper et al., 2003; Korenaga et al., 2000). We apply gravity anomaly inversion, joint inversion of gravity and seismic data and basement seismic velocity analysis to the SIGMA dataset, in particular to seismic line SIGMA III, to ascertain the likely composition of the crust on the SE Greenland margin and we discuss a potential formation model.

6.1.1 Geological setting

Breakup of Avalonia, Baltica and Laurentia during the Palaeogene led to the formation of the NE Atlantic Ocean and its rifted margins. Magmatism associated with the North Atlantic Igneous Province (NAIP) accompanied breakup at 55 Ma, with the first phase of volcanism occurring at 61 Ma beneath Greenland as a low volume mantle plume (Hopper et al., 2003). This activity is documented throughout West and East Greenland (Sinton and Duncan, 1998), as well as offshore SE Greenland, in the area being analysed in this study. NAIP productivity

increased at 56 Ma during breakup resulting in an estimated 10^7 km^3 of new crust in just 3 Myr (Storey et al., 2007). This magmatism resulted in the formation of magma-rich rifted margins on both sides of the NE Atlantic Ocean, extending for over 2000 km displaying typical features such as seaward dipping reflectors, flood basalts, sill intrusions and volcanoes (Funck et al., 2017).

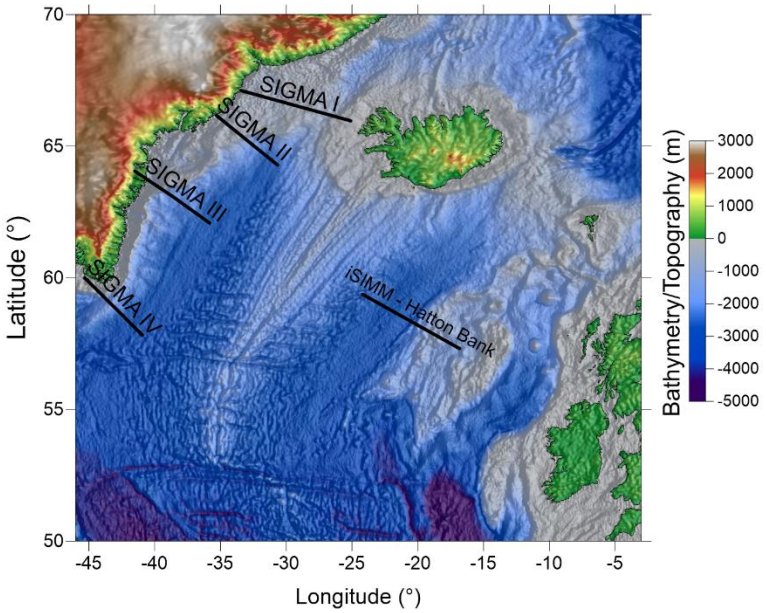

Fig. 6.1. Bathymetry/topography map of the Northeast Atlantic with free air gravity shaded relief overlain. The locations of seismic lines from the SIGMA survey and iSIMM are shown.

6.1.2 SIGMA III seismic data and ODP Sites 917-919 data

The SE Greenland margin, in particular the area sampled by SIGMA III, a seismic line from the SIGMA seismic survey (Fig. 6.1., Dahl-Jensen et al., 1998; Holbrook et al., 2001; Hopper et al., 2003; Korenaga et al., 2001, 2000), lies in the distal zone of the NAIP hotspot. In the distal zone the mantle thermal anomaly is predicted to be relatively small, resulting in less magmatic addition to the margin (Holbrook et al., 2001). The seismic reflection and refraction data from the SIGMA seismic survey (Dahl-Jensen et al., 1998), acquired in 1996, sampled the length of the SE Greenland margin as well as the Greenland-Iceland ridge. The study collected multi-channel seismic and wide-angle data allowing for seismic interpretation and velocity modelling of the margin (Holbrook et al., 2001; Hopper et al., 2003; Korenaga et al., 2000). In this study we focus on seismic line SIGMA III as seismic data from the conjugate margin, Hatton Bank, is also available to study.

We interpret seismic line SIGMA III following on from previous seismic interpretations from Dahl-Jensen et al. (1998), Holbrook et al. (2001) and Hopper et al. (2003). Using the two-way travel time (TWTT) seismic reflection data (Fig. 6.2a-b) we identified several surfaces and

layers consistent with previous interpretations. A layer of post-rift sediments is visible over the entire section with a relatively constant thickness below the seabed (bathymetry). Between the post-rift sediments and basement is a layer of extrusive volcanic material, predominantly made up of seaward dipping reflectors (SDRs). Within the extrusive volcanic layer, an area of incoherent reflectors is visible separating the well-defined SDR sequences.

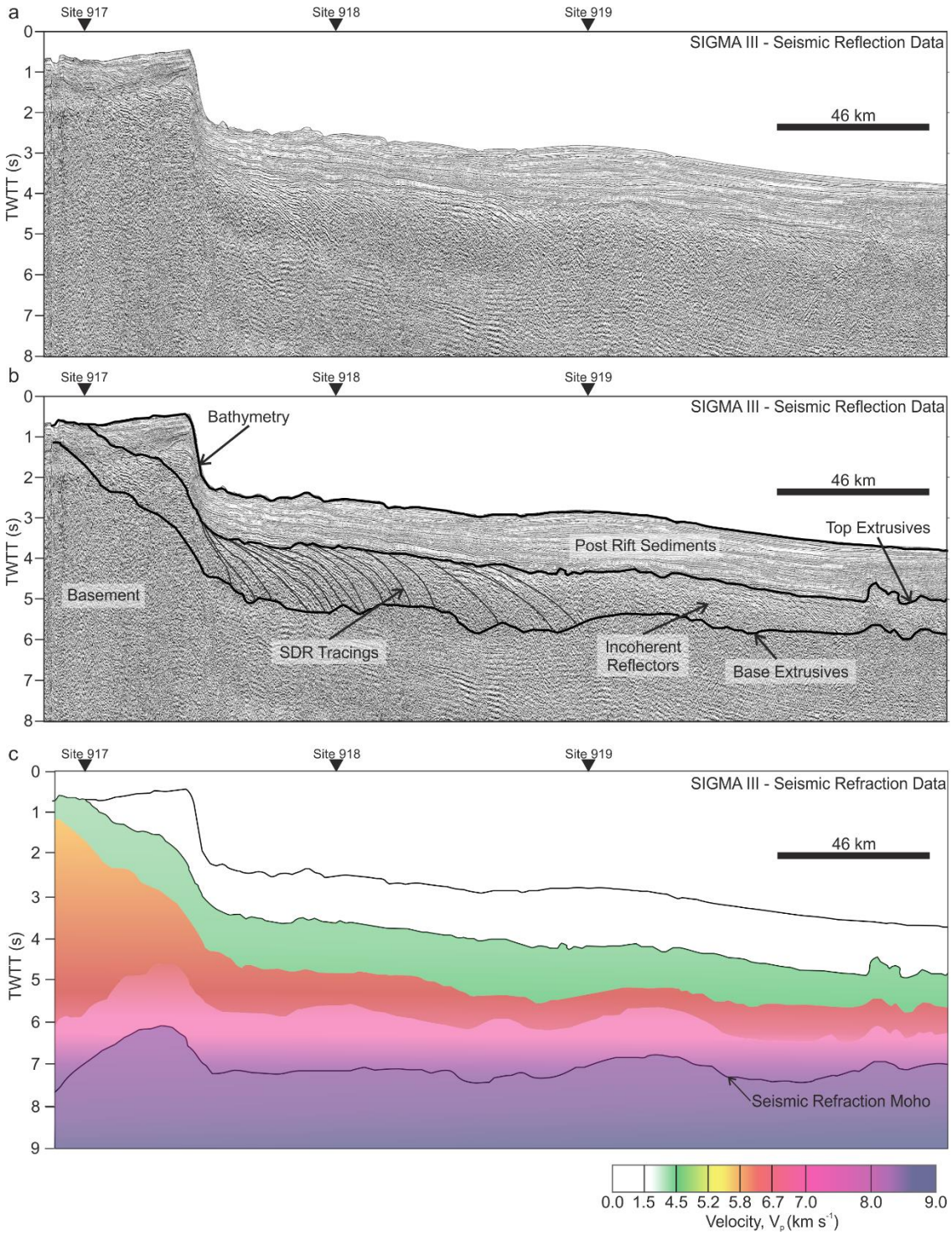

Figure. 6.2. Seismic reflection and refraction data for SIGMA III (location in Fig. 6.1.). a) Un-interpreted time seismic reflection data from www-udc.ig.utexas.edu. Location of ODP sites 917-919 also shown. b) Interpreted time seismic reflection data. c) Refraction model after Hopper et al. (2003). Seismic refraction Moho is highlighted.

On the conjugate margin, Hatton Bank, the SDRs also become less clear and more incoherent oceanwards (R S White et al., 2008). We interpret the incoherent area of reflectivity within the extrusive volcanic layer to be more laterally extensive than the interpretation given by Hopper et al. (2004). Below the extrusive volcanic layer is the basement with no clear internal reflections that could represent layering or a series of intrusions. No seismic Moho is imaged on the reflection data, however, seismic refraction data (Fig. 6.2c, modified after Hopper et al. (2003)) clearly shows a seismic refraction Moho, known as the seismic Moho in this paper hereafter. Overall, the seismic Moho averages 7.5s TWTT, which is quite shallow when compared to Warner's (1987) Moho guide, but the nearby Iceland plume probably maintains a present-day thermal anomaly on the SE Greenland margin resulting in dynamic uplift.

In addition to the seismic reflection and refraction data from the SIGMA survey, several ODP cores were retrieved along the margin that sample pre-breakup volcanic activity as well as volcanism that is synchronous with breakup (Larsen and Saunders, 1998). The lower series of lava flows at the base of the SDR wedge are unconformably situated above pre-breakup sediments, and consist of picrites and basalts (Larsen and Saunders, 1998). Geochemistry of these flows indicates crustal contamination, but this contamination is only present at the base of the flows suggesting later flows had no interaction with continental crust. As a result, later flows were likely sourced directly from the mantle. Stratigraphically above is the middle lava series, formed of more evolved tholeiitic basalts and dacites. Both the lower and middle series have ^{40}Ar-^{39}Ar ages of 62-60 Ma. Unconformably above the middle series is the upper series, dated at 55.8-54 Ma over two ODP sites, again consisting of more evolved Icelandic tholeiites.

Previous interpretations of the SE Greenland margin range from thickened oceanic crust formed via asymmetric seafloor spreading (Larsen & Saunders, 1998; Hopper et al. 2003), to hyper-extended continental crust sandwiched by extrusive and intrusive magmatic material (White & Smith, 2009). Asymmetric seafloor spreading of the SE Greenland and Hatton Bank margins requires a spreading rate that is three times faster for the SE Greenland margin than for the Hatton Bank margin. Formation of sandwiched hyper-extended continental crust occurs as a result of the interaction between tectonic and magmatic processes. Where tectonic processes are initially dominant during breakup, continental crust deforms and thins predominantly through faulting. A gradual increase in melt production as breakup progresses would result magmatic processes becoming dominant and a sandwich of hyper-extended continental crust surrounded by magmatic material, which increases in volume distally towards the point of breakup. The extreme requirements for each interpretation makes both

unlikely. Although asymmetric sea floor spreading is observed elsewhere, e.g. the South Atlantic, the difference in the spreading rates for the SE Greenland and Hatton Bank margins has not been observed elsewhere. Similarly, for the hyper-extension sandwich interpretation, the volume of magmatism produced at the SE Greenland alongside hyper-extension has never been observed globally.

6.2 Gravity inversion to determine Moho depth

Gravity anomaly inversion incorporating a correction for lithosphere thermal gravity anomalies as well as a parameterisation of decompression melting to give a magmatic addition prediction, is used to estimate Moho depth, crustal thickness and lithosphere thinning factor (Alvey et al., 2008; Chappell and Kusznir, 2008a; Cowie et al., 2015b; Greenhalgh and Kusznir, 2007; Harkin et al., 2019; Kusznir et al., 2018).

Satellite-derived free air gravity (Sandwell and Smith, 2009), bathymetry (Smith and Sandwell, 1997), ocean-age isochrons (Müller et al., 2008) and sediment thickness from 2D seismic reflection data are the required inputs for the gravity inversion. Together, these inputs calculate the mantle residual gravity anomaly which is inverted to give Moho topography. We filter the mantle residual gravity anomaly using a Butterworth filter with a 100 km cut off to remove short wavelengths that are associated with shallow features within the crust. We invert the mantle residual gravity anomaly using a 3D spectral inversion (Parker, 1972) and we invoke Smith's Theorem (Smith, 1961) so that the solution for Moho depth is unique for the given input parameters. We assume constant densities for seawater (1039 kg m^{-3}, Nayar et al., 2016), the mantle (3300 kg m^{-3}, Jordan and Anderson, 1974) and the basement (2850 kg m^{-3}, Carlson and Herrick, 1990; Christensen and Mooney, 1995). In addition a reference Moho depth and breakup age are required, both of which are discussed in Section 6.2.2.

6.2.1 Decompression melting parameterisation to predict thickness of magmatic addition

At rifted margins, thinning of crustal material can lead to the decompression melting of mantle material and the addition of magmatic material to the margin. The volume of magmatic material generated is therefore dependent on the amount of continental lithosphere thinning. The thinning factor (γ) is defined as:

$$\gamma = 1 - \frac{1}{\beta}$$

(6.1)

Where β is the lithosphere stretching factor (McKenzie 1978), given as the ratio between initial crustal thickness and present day crustal thickness which is calculated in the gravity inversion.

We parameterise the melting model of White & McKenzie (1989) according to different rifted margin types, using the thinning factor to determine the thickness of magmatic addition. A higher thinning factor implies a higher degree of stretching and thinning which results in a larger perturbation of the geotherm and an increase in decompression melting. Melt thickness is therefore expected to increase with an increase in thinning factor, the magnitude of which is controlled by mantle temperature and lithosphere thickness (Chappell and Kusznir, 2008a; Mckenzie and Bickle, 1988; White and McKenzie, 1989). The presence of the North Atlantic Igneous Province during breakup lead to the production of many magmatic features such as SDRs and onshore flood basalts, resulting in the classification of the SE Greenland margin as a magma-rich rifted margin. As such, we use a magma-rich decompression melting parameterisation within the gravity inversion (Chappell and Kusznir, 2008a), based on the melting model of McKenzie and Bickle (1988), where we assume decompression melting begins when thinning reaches γ = 0.5, with a maximum magmatic addition of 10 km when full thinning is reached. Seismic observations of oceanic crustal thickness and the melting model of White and McKenzie (1989) are also used to constrain the thickness of magmatic addition (Chappell and Kusznir, 2008a). For the SE Greenland margin estimates of oceanic crustal thickness range from 8-12 km (Holbrook et al., 2001; Hopper et al., 2003; Korenaga et al., 2000), which is 1-5 km thicker than average oceanic crust at 7 km (White et al., 1992), possibly due to the presence of the nearby NAIP which would increase mantle temperature and result in excess decompression melting. We varied the decompression melting parameterisation within the gravity inversion so that the maximum magmatic addition reflects the thickened oceanic crust resulting in solutions with 10 km, 12.5 km and 15 km of maximum magmatic addition (Fig. 6.3).

We split the maximum magmatic addition into extrusives and intrusives to present a more geologically realistic cross section (Fig 6.3). To do we use the interpretation of Hopper et al. (2003) to determine extrusive thickness and calculate intrusive thickness by subtracting the extrusive thickness from the total magmatic thickness given in the gravity inversion.

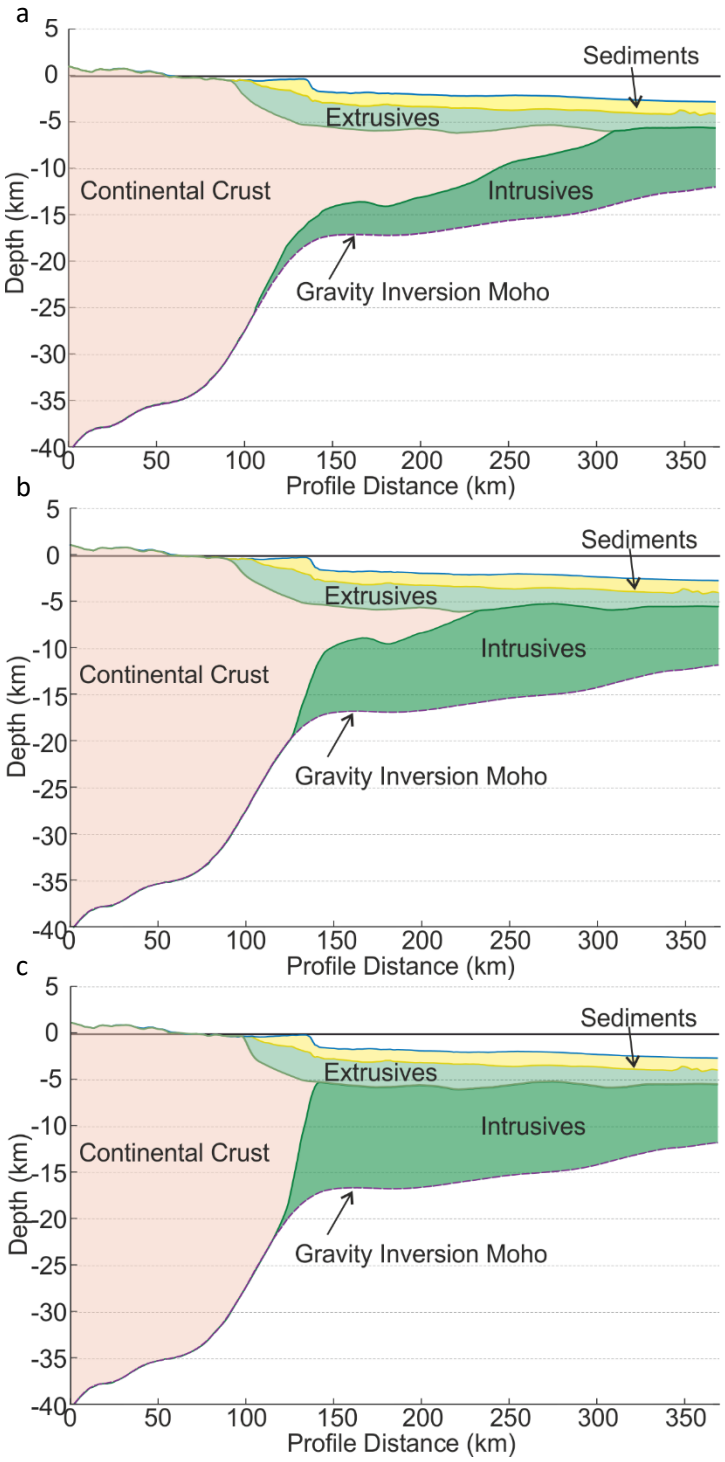

Figure. 6.3. Gravity inversion crustal cross section with varying amounts of maximum magmatic addition divided into intrusives and extrusives. Extrusive thickness taken from Hopper et al. (2003) and intrusive thickness is total magmatic addition minus observed extrusive thickness from Hopper et al. (2003). a) Maximum magmatic addition of 10 km. b) Maximum magmatic addition of 12.5 km. c) Maximum magmatic addition of 15 km.

Crustal thickness is the area between top basement and the gravity inversion Moho. Decompression melting parameterisations determine if basement is magmatic or continental. Within the gravity inversion, a maximum magmatic addition of 10 km produces continental crust that extends over 150 km and ranges from 1-7 km thickness (Fig. 6.3a). In association with the continental crust is magmatic material that ranges from 6-10 km thickness, split between extrusives and intrusives that surround the continental crust. Gravity inversion using 12.5 km of maximum magmatic addition also produces an area of thin continental crust, but it only extends for 50 km and is much thinner with a maximum thickness of 4.5 km (Fig. 6.3b). A maximum magmatic thickness of 15 km produces no continental crust, instead suggesting the thick crust is entirely igneous making the ocean-continent transition very sharp (Fig. 6.3c), similar to the ocean-continent transition on Hatton Bank.

6.2.2 Sensitivity to reference Moho depth and breakup age

Gravity inversion gives depth to the Moho (Fig. 6.3), using bathymetry and sediment thickness data from Hopper et al. (2003), a breakup age of 55 Ma (Funck et al., 2016; Holbrook et al., 2001; Korenaga et al., 2001; Müller et al., 2008; Skogseid et al., 2000) and a reference Moho depth of 36 km (see supplementary information). Moho depth in the distal domain is ~12 km, which gives a crustal thickness of ~8 km. Depth to the Moho increases inboard, to a maximum depth of 17.5 km giving a crustal thickness of ~14 km.

We tested Moho depth sensitivity to breakup age using a range of breakup ages of 51, 53, 55 and 57 Ma (see supplementary information) and only a slight variation is apparent between the results. In addition, we calibrated the reference Moho depth in the gravity inversion by comparing Mohos computed using various reference depths against the seismic refraction Moho from Hopper et al (2003) in the distal domain (see supplementary information). The gravity inversion Moho using a reference Moho depth of 36 km had minimal misfit with the time seismic refraction Moho in the distal domain, so is used within our results.

6.3 Joint inversion of seismic and gravity data to investigate basement density and velocity

Lateral variations in basement density and seismic velocity are calculated using the joint inversion of gravity and time domain seismic reflection data (Cowie et al., 2015b; Harkin et al., 2019). Within the initial gravity inversion, basement density is assumed to be homogenous with a constant density of 2850 kg m^{-3}, however lateral heterogeneities may

exist. By using the joint inversion technique, we are able to identify deviations from the reference basement density and seismic velocity. The densities calculated by the joint inversion technique can be used to identify if the SE Greenland margin is more likely to be composed of hyper-extended continental crust or magmatic crust.

We solve for the lateral variation of the density and seismic velocity of the basement by matching the gravity inversion Moho with the seismic Moho in the time domain. To do so we use a linear Nafe-Drake relationship (Brocher, 2005; Ludwig et al., 1970) to link seismic velocity to basement density. This empirical linear relationship, $V_p = 3.49\rho - 3.46$, gives a seismic velocity of ~6.31 km s^{-1} for an equivalent basement density of 2850 kg m^{-3}, used as the initial constant basement density in the gravity inversion.

The methodology, previously described by Cowie et al. (2016) and Harkin et al. (2019), begins with the conversion of the gravity inversion Moho in depth, into two-way travel time. For the conversion of the gravity inversion Moho we assume that the sediment thickness (depth to top basement), derived from seismic reflection interpretation and depth conversion is correct. We calculate crustal thickness using the distance between top basement, which is taken as the top of the SDRs, and the gravity inversion Moho, which we convert into two-way travel time (TWTT) as an interval TWTT. This interval is added to the seismic interpretation of top basement in the time domain to give the gravity inversion Moho in TWTT.

We compare the gravity inversion Moho and a seismic interpretation of the Moho taken from seismic refraction data (Fig. 6.2), where any differences between the two in the time domain are attributed to lateral heterogeneities within the basement. Adjustment of the seismic Moho minimises the difference between the two Mohos and is achieved by altering the seismic velocity and equivalent basement density across the profile. Adjustment of the basement density affects the Moho depth from gravity inversion, while adjustment of seismic velocity affects the conversion of the Moho from gravity inversion into the time domain. We iteratively adjust both seismic velocity and basement density until the gravity inversion Moho fits the observed seismic Moho, i.e. convergence (Fig. 6.4a).

Performing the joint inversion of gravity and seismic data in the time domain avoids uncertainties associated with velocity models in the depth domain, and can be used to validate seismic interpretations.

Joint inversion of gravity and seismic Moho data produces profiles of lateral basement density and seismic velocity variations for the area between top SDRs and seismic Moho (Fig. 6.4b-c). No offshore seismic data is available for joint inversion in the area between line-distances of 0-100 km. Overall, the density and velocity estimations are within the reference

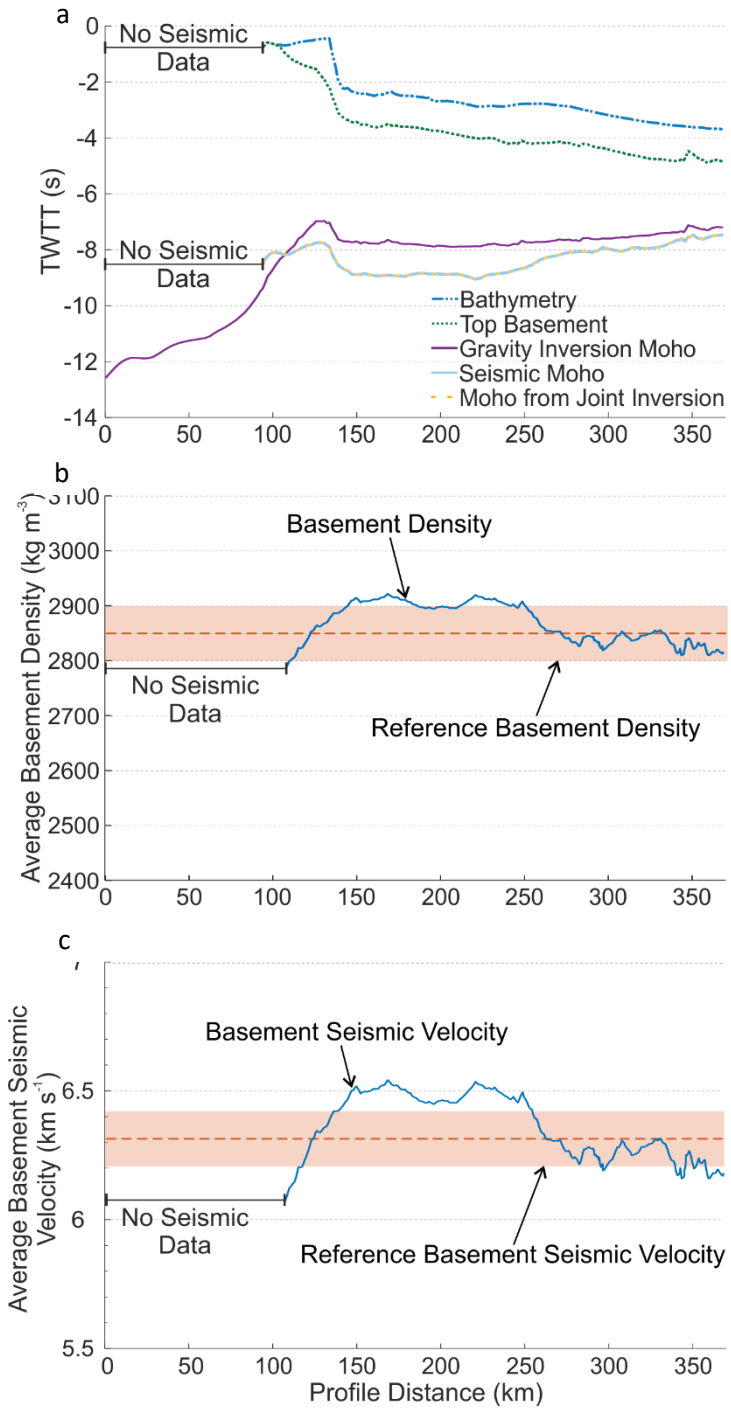

Figure. 6.4. Joint inversion of gravity and seismic Moho data. a) Crustal cross section in the time domain with the Moho from gravity inversion, seismic Moho and Moho from joint inversion. b) Lateral variation in average basement seismic velocity across the profile (blue). Reference basement velocity shown in orange. c) Lateral variation in average basement density across the profile (blue). Reference basement density shown in orange.

range for normal oceanic crust of 2800-2900 kg m^{-3} and 6.1-6.5 km s^{-1} respectively, with the reference range taken from White et al. (1992) and Christiansen and Mooney (1995). Laterally there are variations in basement density and seismic velocity with a clear division at a line-distance of ~270 km, splitting the basement into two distinct areas. Between a line-distance of 100 and 270 km, basement density and seismic velocity remain steady with little variation averaging of 2900 kg m^{-3} and 6.5 km s^{-1} respectively. At a line-distance of 270 km, there is a decrease in the basement density and seismic velocity trends, to 2850 kg m^{-3} and 6.2 km s^{-1} respectively, which continues to the end of the profile again with little variation.

6.4 Basement seismic velocity analysis

Estimates of basement velocity can be obtained using seismic observations and the velocity-distance-time relationship. In the time domain, we calculate the time between our seismic interpretation of top basement, which is also the top of the SDRs, and seismic Moho. Similarly, in the depth domain, we calculate the distance between top basement and seismic Moho. As per the velocity-distance-time relationship, we divide the distance between top basement and seismic Moho by the equivalent in time to give the velocity of the combined SDRs and basement. Calculating the basement seismic velocity across the seismic profile can reveal any lateral changes that may relate to composition.

The relationship between seismic velocity (V_p) and basement thickness (H), H-V_p, corrected for pressure and temperature, can be used to indicate bulk crustal composition and the degree of mixing within igneous melt (Holbrook and Kelemen, 1993; Hopper et al., 2003; Korenaga et al., 2002; White and Smith, 2009). In this study, we use our calculated seismic velocity and observed basement thickness from our seismic analysis to approximate a H-V_p relationship. We do not correct for a reference pressure and temperature due to the ambiguity of choosing a reference pressure and temperature. Using this relationship, we can make interpretations regarding mantle temperature and mantle upwelling. For example, thicker crust formed from a melt originating from deep within the mantle will have seen higher temperatures, and so will have a higher magnesium content resulting in a higher seismic velocity. If active upwelling has taken place, it will allow for the production of thicker crust from a shallower depth due to the regular movement of material across the solidus without needing an increased velocity.

Previous studies replace upper crustal velocities with a set velocity to avoid low velocities associated with alteration. We do not set an upper crustal velocity when calculating estimates of basement velocity to avoid any ambiguity in choosing a velocity. Nor do we

separate out the SDRs and basement due to uncertainty of the boundary between the two. In addition, there is no seismic data available for analysis between a line-distance of 0 and 100 km and a 25 km moving average is utilised within the analysis to smooth the data and make any general trends clear.

Overall, seismic velocities for the combined SDRs and basement average ~6.27 km s^{-1} (Fig. 6.5a). Between a line-distance of 100 and 250 km, seismic velocities are higher with an average of ~6.46 km s^{-1} compared to an average seismic velocity of ~6.11 km s^{-1} between a line-distance of 250 km and the end of the profile, splitting the combined basement and SDRs into two distinct areas.

Overall, the relationship between basement thickness and seismic velocity (Fig. 6.5b) shows thicker crust has a higher seismic velocity, although the absolute seismic velocity is low when compared with values expected from melt produced by high mantle temperatures. This could

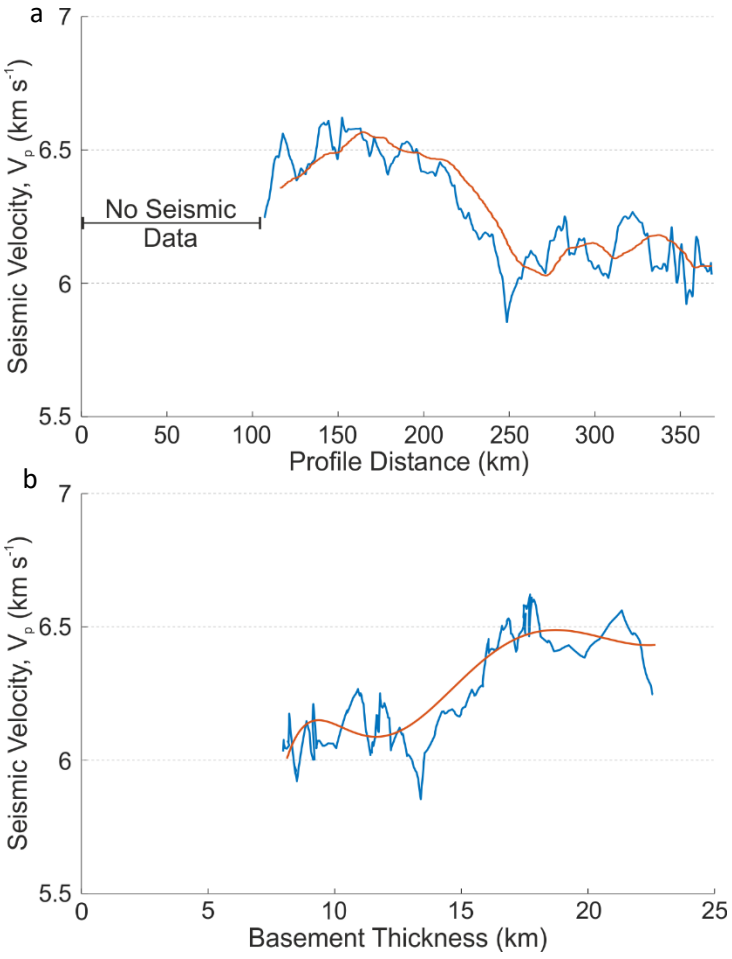

Figure. 6.5. Basement seismic velocity analysis of SIGMA III seismic reflection data. a) Seismic velocity between top SDRs and seismic Moho as defined by Hopper et al. (2003) across the profile. 25 km moving average shown in orange. b) Seismic velocity vs. basement thickness across the profile. 25 km moving average shown in orange.

be a result of including the SDRs within the analysis. At a basement thickness of ~15 km, there is an inflection point about which two trends are visible. Areas with a thicker basement, ~15-23 km thickness, appear to have a constant seismic velocity of ~6.5 km s^{-1} while thinner basement (<15 km) has a more variable seismic velocity with an average of ~6.1 km s^{-1}.

6.5 Discussion

Average basement densities and seismic velocities from joint inversion of gravity and seismic data are 2807 kg m^{-3} and 6.4 km s^{-1} respectively while seismic velocities calculated from seismic velocity analysis are slightly lower, with an overall average of ~6.3 km s^{-1}. These results are greater than the density and velocity of average oceanic crust (Carlson and Herrick, 1990), suggesting the crust on the SE Greenland margin is composed of thick, dense igneous material rather than hyper-extended continental crust. In addition, there are no reflectors on the seismic reflection profile that would suggest the presence of hyper-extended continental crust sandwiched between denser magmatic material, however poor sub-basalt imaging reduces visibility making this interpretation uncertain. Here we discuss the possible origin and formation of thick igneous crust.

There exists a slight discrepancy between the results from joint inversion of gravity and seismic data and seismic velocity analysis. Within the joint inversion, the gravity inversion Moho is converted from depth to time and a linear Nafe-Drake relationship (Brocher, 2005; Ludwig et al., 1970) is used to convert between density and velocity. The seismic velocity analysis uses the velocity-distance-time relationship, which needs no conversion from depth to time, nor density into velocity, which could the cause the slight different in results between the two methods. Additionally, both methods include any extrusive volcanics, such as SDRs, as part of the basement, which would lower the overall densities and velocities due to the volcaniclastic/sedimentary component.

Within our seismic velocity analysis, the inclusion of SDRs and upper crustal velocities resulted in an average basement velocity of ~6.3 km s^{-1} (Fig. 6.5a), which is consistent with the average velocity calculated for oceanic layers 2 and 3, ~6.1 km s^{-1}, using velocity profiles from White et al. (1992).

Our H-V_p profile (Fig. 6.5b) shows that seismic velocity remains constant (~6.5 km s^{-1}) while basement thickness increases from 15 km to 23 km. Our interpretation is that this implies active upwelling took place (Holbrook and Kelemen, 1993; Hopper et al., 2003; Korenaga et al., 2002), which could produce a large volume of low density melt accounting for the low

average velocity we see on the H-V_p profile. Alternatively, the source of the melt could have been continental lithosphere inherited from rifting which would be depleted compared to fertile mantle resulting in more silicic and less dense melts (Picazo et al., 2016).

For the SE Greenland margin to be composed entirely of igneous crust a large amount of magma is required. We can estimate the volume of magma added to a margin through a parameterisation of decompression melting models within the gravity inversion. The amount of magma added depends on the amount of thinning the crust has undergone, with full thinning of the crust producing the maximum thickness of magma chosen in the gravity inversion. Inversions with a maximum of 10 km, 12.5 km and 15 km magmatic addition investigate how much magma is required for the basement to be igneous. Solutions using 10 km (Fig. 6.3a) and 12.5 km (Fig. 6.3b) magmatic addition predict the presence of continental crust <10 km thick and wide ocean-continent transition zones. Our solution using 15 km magmatic addition (Fig. 6.3c) predicts a sharp ocean-continent transition followed by 15 km thick oceanic crust, consistent with our joint inversion and seismic velocity results that predict igneous crust (see supplementary figure for conjugate cross section).

Asymmetric seafloor spreading has previously been invoked to explain the broad region of thick crust on the SE Greenland margin, which requires spreading rates to be three times faster on the SE Greenland margin than the Hatton Bank margin (Larsen and Saunders, 1998). During early spreading in the North Atlantic Larsen and Saunders (1998) show that the sum of the Hatton Bank and SE Greenland spreading rates is significantly higher than the subsequent spreading history, however when looking at the individual spreading rates they would not produce the present day asymmetry. Presently, no other areas worldwide display such a high spreading rate asymmetry as required for the SE Greenland and Hatton Bank margins. Although asymmetric magma-rich margins are suggested occur in the South Atlantic from fast spreading rates, the rates required to create this asymmetry are not as extreme as those required for the North Atlantic margins (Brune et al., 2014). Alternatively, White and Smith (2009) suggest the cause of the asymmetry is due to asymmetric continental rifting and breakup. Within this model, an initial stage of rifting is suggested to occur prior to the addition of magma, possibly during earlier rifting events recorded in the Mesozoic. Later magmatism then buried and surrounded the stretched continental crust giving the appearance of a sandwich effect. In this interpretation, hyper-extended continental crust is predicted to exist on the SE Greenland margin, which is not compatible with our seismic observations and quantitative analysis.

With previous hypotheses unlikely and incompatible with our analysis, an alternative hypothesis to explain the broad region of igneous crust on the SE Greenland is required. We propose a new mechanism whereby the thick igneous crust forms via distributed plate divergence and oceanic crustal accretion (Fig. 6.6). Initially, thinning and rupturing of continental crust results in as lithospheric breakup (Fig. 6.6a, Minshull et al., 2001; Tugend et al., 2018). The presence of a mantle thermal anomaly means the asthenosphere temperature is increased beyond normal temperatures (Holbrook et al., 2001). This results in excessive and distributed decompression melting of the asthenosphere where new over-thickened oceanic crust is accreted over a broad region (Fig. 6.6b-c). At this point, there is no localisation of decompression melting so plate divergence is distributed and symmetric. Within the extrusive volcanic layer visible on seismic reflection data (Fig. 6.2) there exists an area of incoherent reflectors, outboard of clear SDR reflections that are associated with continental crust (Hopper et al., 2003). The area of incoherent reflectors is consistent with magmatism that would form via distributed deformation. Eventually, as the asthenosphere temperature decreases formation of oceanic crust via distributed decompression melting stops. Instead, decompression melting localises creating a defined plate boundary allowing for the production of normal oceanic crust (Fig. 6.6d). Localisation of the plate boundary and decompression melting could have occurred at the edge of the over-thickened oceanic crust (i.e. adjacent to Hatton Bank) which would then give way to asymmetric spreading and the present-day conjugate margin structure. This theory could also explain other areas that display anomalous thick crust, for example the Limpopo Plains, Mozambique (Mueller et al., 2016) where there is no clear spreading centre but large volumes of magma exist.

Larsen and Jakobsdottir (1988) interpret the presence of crytochrons immediately offshore SE Greenland which would suggest organised seafloor spreading occurred instead of distributed plate divergence. However, White and Smith (2009) interpret the anomalies to represent subaerial basalt flow fronts on the basis of the subsidence history, and analogues on the Faroes shelf. Despite this, both interpretations suggest magmatism was focused at this point, however, seismic observations show the flows only extend for 100 km offshore. It is also worth considering the source of the flows, as it is possible the basalt flows travelled from an onshore source such as a fissure (Larsen and Saunders, 1998), in which case they would not necessarily be directly related to the rifting. Outboard of the clear SDR flows reflectors become incoherent, more consistent with formation by dstributed divergence. It is possible that a change from focused, to distributed back to focused divergence occurred, which would require rapid changes in underlying mantle conditions.

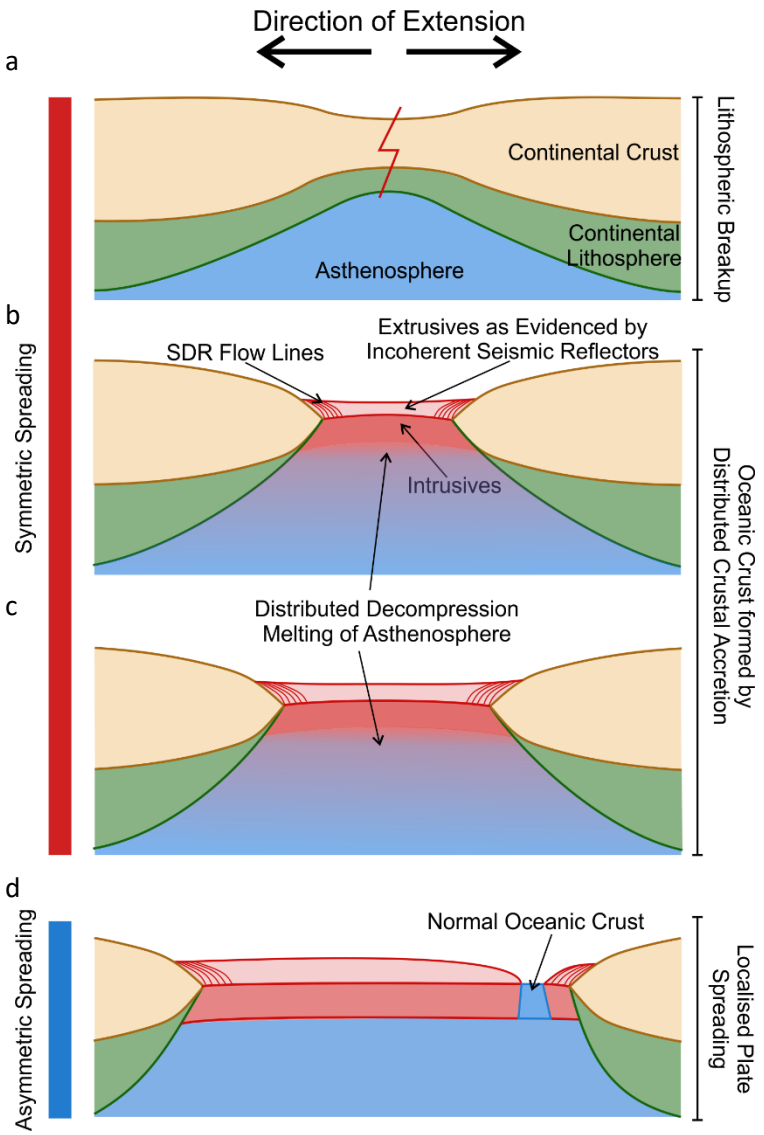

Figure. 6.6. Cartoon of distributed plate divergence theory. a) Breakup of continental crust but not the underlying continental lithosphere. b) Upwelling of underlying continental lithosphere as extension continues leads to decompression melting and the accretion of oceanic crust over the entire area of extension. c) Continuation of extension and distributed oceanic crustal accretion. d) Breakup of continental lithosphere leads to the localisation of extension. The plate boundary is now localised and normal oceanic crust is produced from the new spreading centre.

6.6 Summary

The magma-rich rifted margins of the NE Atlantic display asymmetry whereby the SE Greenland margin exhibits broad region of 15 km thick crust, commonly interpreted as igneous crust, that is absent on the conjugate Hatton Bank margin. Such asymmetry is similar to classic magma-poor margins Iberia-Newfoundland leading to the hypothesis that the thick crust is cored with hyper-extended continental crust. Our analysis, consisting of gravity anomaly inversion, joint inversion of seismic and gravity data and basement seismic velocity

analysis, suggests the 15 km thick crust has a density and velocity consistent with oceanic crust. Within both the joint inversion and basement seismic velocity analysis, denser/seismically faster basement is visible inboard while outboard basement has a lower density and velocity, implying a change in composition oceanwards. To explain these results we suggest a new formation mechanism whereby the NE Atlantic conjugate margins between SE Greenland and Hatton Bank are formed by a two-stage process. First, an increased mantle temperature leads to symmetric distributed plate divergence and oceanic crustal accretion. Then, localisation of decompression melting concentrates plate divergence at the Hatton Bank margin leading to normal oceanic crustal accretion and an asymmetric system.

Supplementary Information

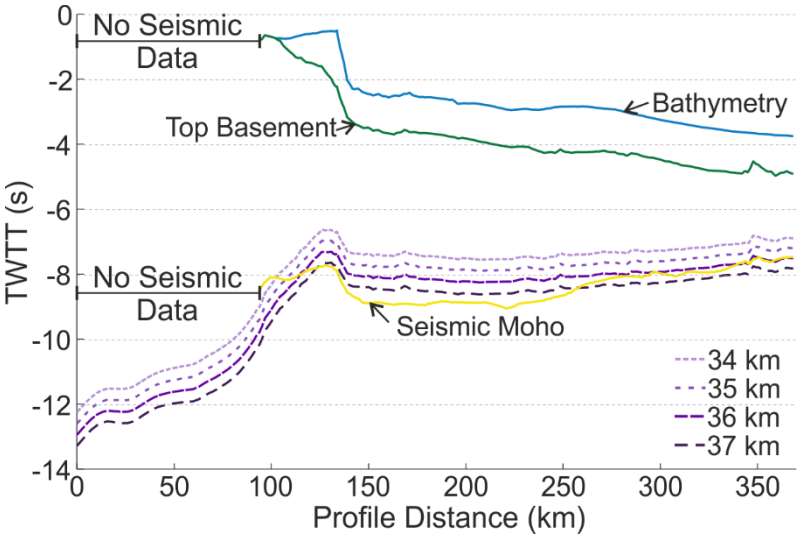

Fig. 6.S1. Calibration of reference Moho depth for use in the gravity inversion. In purple, gravity inversion Mohos using different reference Moho depths (see key). In yellow, is the seismic Moho taken from seismic refraction data. In the oceanic domain, the seismic Moho closely matches the gravity inversion using a reference Moho depth of 36 km.

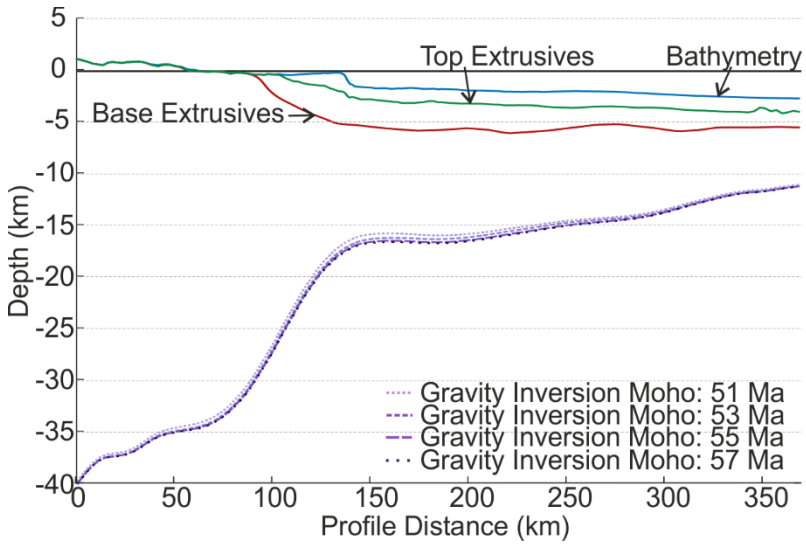

Fig. 6.S1. Sensitivity of gravity inversion Moho to breakup age.

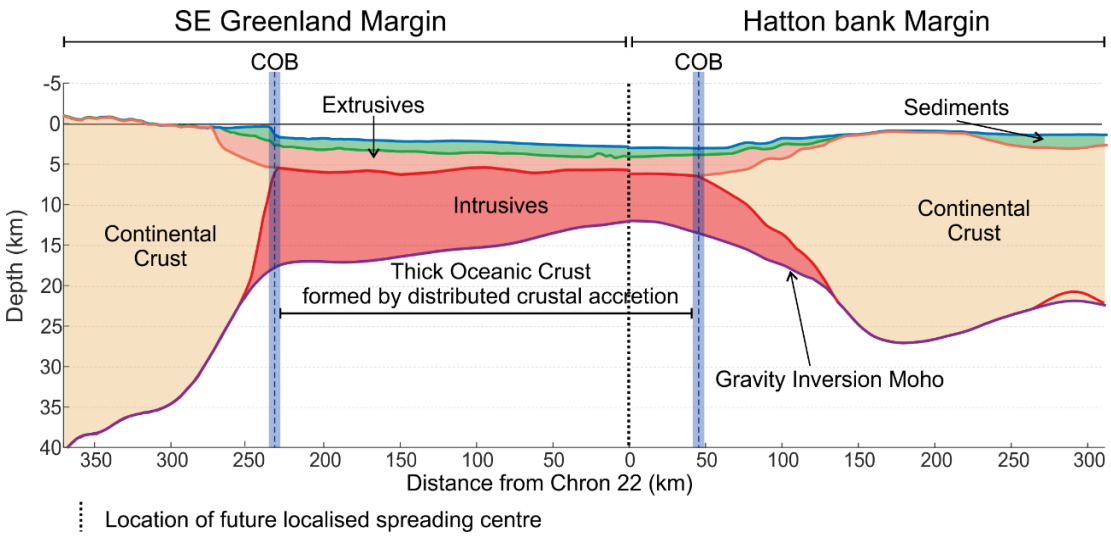

Figure. 6.S3. Crustal cross section of conjugate SE Greenland and Hatton Bank margins restored to magnetic anomaly chron 22. Public domain bathymetry, sediment thickness from seismic reflection profiles (SIGMA III and iSIMM Hatton Bank) and Moho from gravity inversion. Limits of continental crust given by decompression melting parameterisations in the gravity inversion. Continent-ocean boundary (COB) shown at the limit of continental crust. Outboard of the COB the crust is igneous, averaging 10 km thickness. Future localised seafloor spreading shown by vertical black dotted line.

Chapter 7

Discussion and Summary

Within this thesis, three rifted margins have been studied in order to investigate different aspects of magmatism relative to breakup at a rifted margin. Each chapter contains a discussion of that chapter's findings and wider context, which are summarised below. This chapter is therefore a discussion of the thesis as a whole.

First, the East Indian margin was investigated to address the use of end-member terminology when classifying margins as magma-rich or magma-poor. Second, the Pelotas margin in the South Atlantic exhibits an extraordinary seaward dipping reflector (SDR) sequence, which was examined to better understand the composition and timing of extrusive magmatism relative to breakup. The depositional environment of these SDRs was also investigated to further our understanding of the relationship between magmatism and breakup. Finally, the conjugate margins of Southeast (SE) Greenland and Hatton Bank in the Northeast (NE) Atlantic were examined to see how large volumes of magma affects breakup and conjugate margin structure. Altogether, the in depth analysis of the characteristics of each margin and their relationship to breakup can be used to redefine margin classification. In addition, the results of each margin can be used to provide an insight into the controls on magmatism, whether it is elevated mantle temperatures or active upwelling both of which can be attributed to the presence of mantle plumes. Mantle plumes are often credited with having a strong influence on rifted margin formation, I use the margins studied here to discuss the effect of mantle plumes on rifting.

7.1 Rifted margin classification

The three margins presented within this thesis demonstrate the large variability of rifted margins despite each being categorised as typical end member margins. The features present at each margin vary in terms of scale, geometry and origin, for example, the inner SDRs at the Pelotas margin are extensively larger than those on the SE Greenland margin and are linked to LIP magmatism rather than ocean-ridge formation which is believed to be the origin for the SE Greenland SDRs. Characterising these margins using the standard magma-poor and magma-rich classifications is ambiguous as it implies a certain volume of magmatic material. Here I discuss an alternative way of classifying margins using the timing of magmatism relative to breakup.

Generally, rifted margins are classified as either magma-poor or magma-rich based on their magmatic budget (Doré and Lundin, 2015; Franke, 2013; Geoffroy, 2005; Menzies et al., 2002; Reston and Manatschal, 2011; Sawyer et al., 2007). However, using these terms can be misleading as they imply a certain amount of magmatic addition for the margin, which is often difficult to resolve. Interpreting an incorrect magmatic budget could result in a misunderstanding of formation processes as the parameters that control decompression melting can influence breakup (Armitage et al., 2009; Fletcher et al., 2009; Hawkesworth et al., 2000; Tugend et al., 2018). Instead of classifying margins based on the volume of magmatic addition alone, it may be more informative to examine the timing of decompression melting relative to crustal thinning and breakup. Davis and Lavier (2017) and Tugend et al. (2018) both suggest that when decompression melting occurs early relative to breakup, large volumes of magma may be produced quickly resulting in thick magmatic crust which is often regarded as a typical magma-rich characteristic. When decompression melting occurs later relative to breakup, tectonic processes are more dominant allowing for the extreme thinning of the crust and sometimes the exhumation of serpentinised mantle, which are typical magma-poor features.

In Chapter 3, a geophysical study of the East Indian margin revealed the presence of both magma-poor and magma-rich characteristics, despite numerous classifications of the East Indian margin as a typical magma-poor rifted margin. Our analysis showed that a two-phase breakup resulted in the present-day configuration. The occurrence of two different breakups on a single margin demonstrates the importance of the relative timing of magmatism. In the first breakup, magmatism was delayed, allowing for extreme crustal thinning and exhumed serpentinised mantle to form, while the second breakup resulted from a ridge jump and was accompanied by a large volume of magmatism that formed 9 km thick magmatic crust. Although the East Indian margin is a hybrid of both magma-poor and magma-rich margins, it demonstrates how the timing of magmatism relative to breakup influences the final structure of a margin.

Chapters 4 and 5 investigated the magmatism on the Pelotas margin located in the South Atlantic. In both chapters, three distinct SDR sub-packages are recognised due to varying average densities and basalt fractions. These packages, from the most proximal oceanwards are, inner SDR package 1, inner SDR package 2 and the outer SDR package. The two inner SDR packages are interpreted to have formed subaerially during intra-continental rifting, while the outer SDR package is interpreted to have formed subaqueously during breakup. The onset of magmatism on the Pelotas margin occurred prior to breakup and extreme crustal

thinning, implying the magmatic processes preceded the tectonic processes during margin formation.

In Chapter 6, a broad region of 15 km thick crust on the Southeast (SE) Greenland margin that is absent on the conjugate Hatton Bank margin has resulted in asymmetry analogous to the asymmetry seen on magma-poor margins. To investigate this asymmetry, two different hypotheses were examined for the composition of the 15 km thick crust, first that the crust was entirely magmatic and second that the crust contained a core of hyper-extended continental crust. The analysis of the SE Greenland margin indicated that the broad region of thick crust situated between continental crust and oceanic crust, is likely to consist entirely of magmatic material. This interpretation implies a sharp ocean-continent boundary, suggesting that the magmatic processes occurred prior to the tectonic processes in the formation of the margin. The apparent asymmetry of the SE Greenland margin and the Hatton Bank margin is interpreted to be a product of the localisation of plate divergence at the ocean-continent boundary of the Hatton Bank margin, after distributed symmetric plate divergence and magmatic crustal accretion.

Across all three margins, the timing of magmatism relative to breakup was a major contributor to the differences in the final structure of each margin. Where magmatism occurred early, margins exhibit magma-rich characteristics while later magmatism allowed tectonic processes to determine the final structure. Using the timing of magmatism as an additional tool to classify margins reduces ambiguity and makes the implied formation processes clear.

7.2 Ocean-continent transitions: Narrow and Magmatic?

The ocean-continent transition (OCT) zone, defined here as the area between unequivocal continental and oceanic crust, is often interpreted to be narrow at magma-rich margins and has since become a common characteristic of magma-rich margins. Explanations include elevated mantle temperatures (White and McKenzie, 1989), and small-scale convection resulting from rapid extension (Mutter et al., 1988), both of which focus extension over a small area. Using the margins investigated in this thesis, I discuss whether there is a relationship between narrow and magmatic margins.

On the SE Greenland margin, quantitative results suggests the OCT is sharp, <50 km wide, while results on the Pelotas margin suggest the OCT is ~100 km when basement formed by intra-continental rifting is removed. Finally, the OCT at the East Indian margin is the widest

at ~150 km wide. A margin is considered narrow when the transition from continental to oceanic crust occurs over a distance of 100 km or less (Brun, 1999). Using this definition the East Indian margin would not be classed as a narrow margin while the Pelotas and SE Greenland margins would be classed as narrow. Taking previous classifications of these margins, the East Indian margin is classed as a magma-poor margin while the Pelotas and SE Greenland margins are considered to be magma-rich margins. This would suggest that magmatic margins are also narrow margins. Where it is difficult to quantify the width of a margin, the presence of magmatic features could be an indicator that a margin is narrow.

A narrow margin usually has a narrow continental shelf and shallow onshore sedimentary basins, which provide favourable conditions for hydrocarbon reserves (Brun, 1999). If the relationship between magmatic and narrow margins holds true, this would indicate that magmatic margins also have the potential for hydrocarbon reserves.

7.3 Controls on magmatism

Several parameters contribute towards the onset of decompression melting such as mantle temperature, mantle fertility and active upwelling. Mantle temperature is often considered as a controlling factor in the production of magma (White, 1992; White and McKenzie, 1989, 1995). An increase in mantle temperature of 100-150°C above normal, often associated with the presence of mantle plumes, will produce large volumes of melt in excess of normal volumes that generate 7 km of oceanic crust (Holbrook et al., 2001; Mckenzie and Bickle, 1988; Skogseid et al., 2000; R. S. White et al., 2008; White and McKenzie, 1989). Melt formed from a higher mantle temperature will be magnesium and iron rich meaning it will be seismically faster and denser than normal oceanic crust (White and McKenzie, 1989). Where stretching and thinning of the lithosphere occurs abruptly, small-scale convection is induced due to lateral thermal gradients within the mantle (Buck, 1986; Mutter et al., 1988; Zehnder et al., 1990). Active upwelling produces larger volumes of melt than those produced by high mantle temperatures. (Korenaga et al., 2002; Zehnder et al., 1990). With a similar composition to normal oceanic crust, the resultant seismic velocities and densities will also be similar to normal oceanic crust. The composition of the mantle also affects the onset of decompression melting. A more fertile mantle, constituting depleted mantle and recycled oceanic crust, would lower the solidus producing more melt at lower temperatures. This melt would be full of volatiles and lower density minerals resulting in a relatively low seismic velocity and density (Korenaga et al., 2002; Niu et al., 2001; Sallarès et al., 2005).

Within this thesis, investigations of the Pelotas margin in the South Atlantic and the SE Greenland margin in the NE Atlantic both revealed lateral changes in magmatism oceanwards, which could represent a change in the parameters controlling decompression melting during rifting and breakup. The Pelotas margin demonstrates a decrease in basalt fraction and bulk density oceanwards, a result that is reflected on the SE Greenland margin, which shows a decrease in seismic velocity oceanwards. In addition, there is a change in the thickness of magmatic addition before and after breakup. On the Pelotas margin, the inner SDR packages are considerably larger than the outer SDR package, in terms of thickness and lateral extent. The inner SDR packages average ~9.5 km thickness over 200 km while the outer SDR package averages ~6 km thickness over 100 km. On the SE Greenland margin, combined extrusives and basement inboard of breakup is very thick, ~15 km, when compared to 8-10 km crustal thickness in the oceanic domain. Although these values are taken from single 2D seismic profiles, I assume they are still representative of the entire margin when other studies of the same margins are considered (Hopper et al., 2003; Korenaga et al., 2001; McDermott et al., 2018; Stica et al., 2014). Therefore, these margins effectively demonstrate the relative differences in petrological properties, thickness and lateral extent of magmatic features before and after breakup.

Although the pre-breakup magmatic material has higher densities and velocities than the post-breakup magmatic material on both margins, they are much lower than the velocity and density of magmatic crust produced by high mantle temperatures (see fig. 3d in White et al., 2008). Instead, the thickness of magmatic material and associated velocities and densities imply that active upwelling is the dominant parameter controlling melt production. Active upwelling requires lateral thermal gradients, which often occur from sharp crustal stretching and thinning. On both the Pelotas and SE Greenland margins sharp transitions in basement thickness are visible. The Pelotas margin displays a change from 25 km thick basement to 10 km thick basement over a narrow region (~50 km) while the SE Greenland margin shows a transition from 25 km thick continental crust to magmatic basement over ~30 km, both of which would produce large thermal gradients in the underlying mantle.

However, some studies have suggested an interplay of all the parameters during decompression melting (Davis and Lavier, 2017; Holbrook et al., 2001; Tugend et al., 2018). During formation, all three margins studied within this thesis were in proximity to a mantle plume (East India: Kerguelen, Pelotas margin: Tristan da Cunha, SE Greenland margin: North Atlantic Igneous Province), so an associated thermal anomaly could be expected which would have an effect on the melt production. On the SE Greenland margin, seismic velocities appear

to be relatively low when compared against igneous basement thickness suggesting active upwelling was also present during formation. However, the seismic densities and velocities calculated for each margin include extrusive material, which is usually excluded when determining the igneous thickness-seismic velocity relationships. The presence of extrusive material lowers the overall density and seismic velocity. Accounting for this it is therefore possible that the calculated densities and seismic velocities are large enough to be associated with a high mantle temperature source rather than active upwelling. To fully understand what controls decompression melting at each margin a comprehensive geochemical study is required.

7.4 Rifted margins and mantle plumes

Elevated mantle temperatures are often the result of mantle plumes, defined here as the upwelling of hot material originating within the mantle. First described by Wilson (1963, 1973) and Morgan (1971), mantle plumes have been identified globally underneath and at the edge of tectonic plates. They are commonly associated with large igneous provinces (LIPs) with some examples including the Tristan da Cunha plume and the Paranà-Etendeka LIP (Ernesto et al., 2002; Harry and Sawyer, 1992), the Réunion plume and the Deccan traps (Coffin and Eldholm, 1994) and the Kerguelen plume and the Kerguelen Plateau (Olierook et al., 2016).

Many studies have discussed the relationship between mantle plumes, LIPs and rifted margins (Coffin and Eldholm, 1992; Courtillot et al., 1999; Franke, 2013; Harry and Sawyer, 1992; Hill, 1991; Menzies et al., 2002; Renne et al., 1992; Richards et al., 1989; Storey, 1995; White and McKenzie, 1995), with most studies often stating the large volumes of melt that form LIPs require an increase in mantle temperature by ~100-200 ℃ (White and McKenzie, 1989), usually explained by the presence of a mantle plume. Magmatism found at rifted margins has been geochemically linked to LIP magmatism. Evidence from drilled SDR wedges at a variety of magma-rich margins shows they largely consist of tholeiitic basalts (e.g. Larsen and Saunders, 1998), as do the majority of LIPs (Hawkesworth et al., 2000). Onshore analogues of lower crustal bodies that form the lower parts of magma rich margins have been shown to have chemical signatures consistent with mantle derived melts. These lower crustal bodies are commonly believed to form from elevated mantle temperatures often the result of a mantle plume (R. S. White et al., 2008).

At each of the rifted margins discussed within this thesis a mantle plume has been present during formation. At the East Indian margin, surface volcanism associated with the Kerguelen

plume was active as early as ~130 Ma (Olierook et al., 2016) through to the present day, spanning the duration of rifting and breakup on the margin. The formation of the Paraná LIP was contemporaneous with the Pelotas margin and was likely sourced from the nearby Tristan da Cunha plume (Ernesto et al., 2002). And finally at the SE Greenland margin, the Iceland plume is known to have contributed heavily towards the formation of the surrounding rifted margins (Holbrook et al., 2001). It is often stated that the presence of a mantle plume during rifted margin development results in the formation of a magma rich margin. Both the Pelotas and SE Greenland margins are classified as magma-rich margins (Holbrook et al., 2001; Stica et al., 2014), however, the East Indian margin has been previously classified as a magma-poor margin (Haupert et al., 2016) despite forming contemporaneously with plume related volcanism and being shown to have magmatic crust within the ocean-continent transition (See Chapter 3, Harkin et al., 2019). The inconsistency in the classification of these margins could be due to the magnitude of plume influence as a result of distance between the margin and mantle plume. The East Indian margin, despite forming at the same time as plume related volcanism, was not as close in proximity to the Kerguelen plume (Coffin et al., 2002; Coffin and Eldholm, 1994) when compared to the distance between the Pelotas margin and the Tristan da Cunha plume (Harry and Sawyer, 1992), and the distance between the SE Greenland margin and the Iceland plume (Holbrook et al., 2001). In addition, the main eruptive phase of the Kerguelen plume occurred much later than the formation of the East Indian margin. At the time of formation, there were smaller scale early surface expressions such as the Rajmahal traps, but the main eruptive phase began approximately 10 Ma after breakup (Olierook et al., 2016). It is therefore likely that a trade-off exists between plume proximity and magma rich margin formation.

The close association of mantle plumes and rifted margins as discussed above suggests that plumes may play a part in initiating rifts. At the margins discussed in this thesis, continental and lithospheric breakup tend to occur where a plume is established, and volcanism is present. However, despite many rifted margins appearing to form in association with large igneous provinces and mantle plumes there also exists obvious exceptions, such as the Iberia-Newfoundland margins (Sutra and Manatschal, 2012), and the Australia-Antarctica margins (Gillard et al., 2016). The existence of these margins suggests mantle plumes are not essential for rifted margin formation nor do they initiate all rifts. The role of mantle plumes within rifting could be dependent on the size of continental block undergoing breakup. Storey et al., (1995) state that mantle plumes are only a controlling factor when smaller continental blocks break up, while in the case of larger continental blocks such as Gondwana, mantle plumes

only assist in determining the location of breakup. The Pelotas and East Indian margins once formed parts of Gondwana while the SE Greenland margin once formed part of the amalgamated North America-Greenland-Europe plates, all considered to be large continental blocks which would imply the associated mantle plumes did not control the onset of rifting. The location of breakup at each margin appears to plume dependent. At the East Indian margin, a ridge jump coinciding with surface volcanism and a potential thermal anomaly within the mantle, concentrated breakup to between Elan Bank and India (Harkin et al., 2019). At the SE Greenland margin breakup occurred at the edge of the Iceland plume where a change in mantle temperature occurred (Holbrook et al., 2001). Finally, at the Pelotas margin breakup corresponded to the position of the underlying Tristan da Cunha plume (Hawkesworth et al., 2000).

Laboratory studies of fluid dynamic analogues also state that mantle plumes are incapable of initiating rifting but may provide extra deviatoric stresses leading to local reorganisation of tectonics, i.e. magma assisted rifting (Hill, 1991). Magma-assisted rifting is where large scale dykes >20 km long and >1 m wide, which commonly form in association with mantle plumes and LIPs, accommodate large amounts of extension (Bastow et al., 2010; Kendall et al., 2005; Rowland et al., 2010). Seismic observations of the Pelotas margin (Fig. 4.3., Chapter 4) suggest a lack of dykes, which would not imply magma-assisted rifting. However, further inland there exists the large Ponta Grossa dyke swarm, which trends northwest following the orientation of rifting and extension (P.R. Renne et al., 1996). At the SE Greenland margin, there is also large dyke swarm that stretches from the south-eastern margin to the eastern margin covering a distance over 780 km (Larsen, 1978; Wager and Deer, 1938). Once again, this dyke swarm is orientated in the same direction as extension and rifting and is associated with the opening of the North Atlantic Ocean and the formation of the rifted margins (Larsen, 1978).

Findings from the Pelotas, SE Greenland and East Indian margin all suggest mantle plumes play an important role in the formation of rifted margins. It is likely that mantle plumes control the location of breakup and provide large amounts of extension, assisting rifting rather than initiating rifting and breakup.

7.5 Potential future work

Rifted margins are the dominant tectonic setting for giant hydrocarbon reserves, accounting for 35% of the world's current total (Mann et al., 2005), however limited knowledge of magma-rich margins means the majority of reserves are found elsewhere. There is great

potential for hydrocarbons on magma-rich margins provided we further our understanding of the relationship between magmatism and breakup. Additional work on subsidence histories, thermal calibration and high-quality seismic interpretations of margins could useful in discovering potential hydrocarbons at rifted margins, particularly if combined with the techniques presented within this thesis. The basalt fraction within the gravity inversion can be used to infer SDR composition (Chapter 4), which can be used in margin restorations as shown in Chapter 5, determining depositional environments during breakup and providing an additional constraint on potential hydrocarbon reserves.

A re-evaluation of margin classification is advised, where margins are defined using the timing of magmatism relative to breakup rather than the apparent volume of magma. To do so I recommend the integration of both qualitative and quantitative techniques to provide robust interpretations. This work has highlighted the importance of incorporating a variety of quantitative techniques alongside qualitative interpretations when analysing the magmatic features of a margin and in margin classification.

Using these quantitative methods, further study of the along strike variations of the margins presented in this thesis using would be useful. Drill hole data along each of the margins could provide information on the thermal history, subsidence history, and geochemistry of the sediments, volcanics and basement. If seismic refraction data became available to study on the Pelotas and East Indian margins, then it could provide a detailed analysis of the velocity structure of the magmatic features, which could test the interpretations presented within this thesis.

Further analysis of additional rifted margins is needed to understand formation of the different types of magmatism found at rifted margins. The existence of high-quality seismic reflection data on the southern South Atlantic margins make them a good candidate for future study. Within the North Atlantic, the variety of previous studies and datasets, including refraction and drill hole data, allow for a comprehensive study of magmatism and breakup at rifted margins. Where possible, conjugate margins should be investigated so that we gain a complete understanding of breakup and the distribution of magmatism.

Appendix A

Summary of quantitative methods

Within this appendix, I provide a summary of the methods used throughout this thesis. Each chapter stands alone as independent journal articles, so some of the material within this appendix may overlap each chapter.

A.1. Gravity anomaly inversion

Gravity anomaly inversion (also known as the gravity inversion) predicts Moho depth, crustal thickness, lithosphere thinning and thickness of magmatic addition. Figure A.1 describes the gravity inversion methodology which follows previous publications (Alvey et al., 2008; Chappell and Kusznir, 2008a; Cowie et al., 2015b, 2016; Cowie and Kusznir, 2012; Fletcher et al., 2013; Greenhalgh and Kusznir, 2007; Harkin et al., 2019; Kusznir et al., 2018; Nirrengarten et al., 2016; Roberts et al., 2013; Stanton et al., 2019; Tugend et al., 2014a).

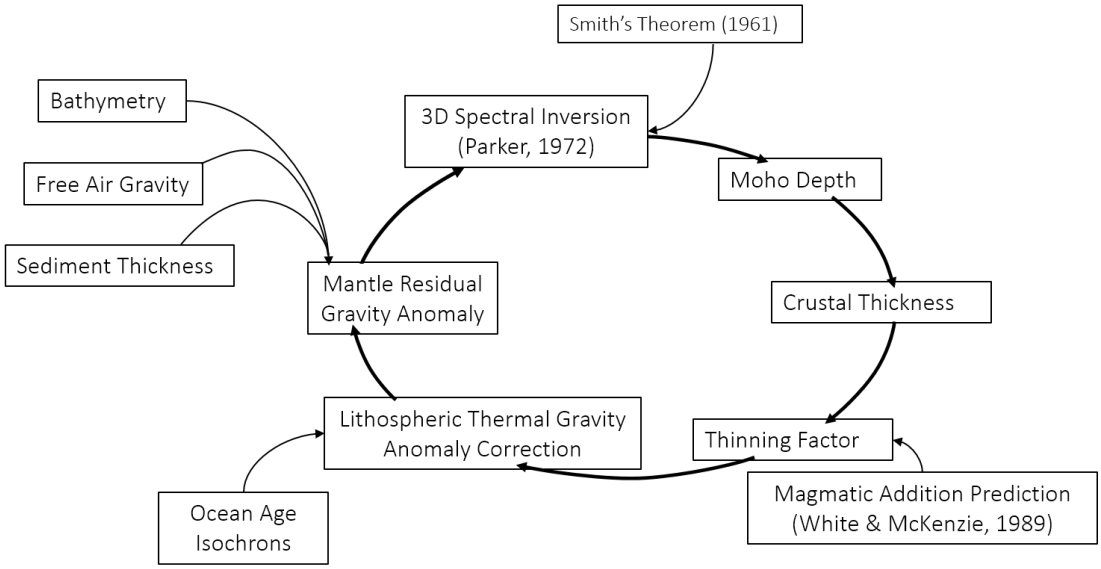

Fig. A.1. Gravity inversion workflow, modified after Alvey et al. (2008).

The inputs for the gravity inversion are satellite-derived free-air gravity (Fig. A.2a, Sandwell and Smith, 2009), bathymetry (Fig. A.2b, Smith and Sandwell, 1997), ocean-age isochrons (Fig. A.2c, Müller et al., 1997) and 2D sediment thickness (Fig. A.2d), taken from pre-stacked depth-migrated seismic reflection data or open-access data sources (Laske and Masters, 1997; Whittaker et al., 2013).

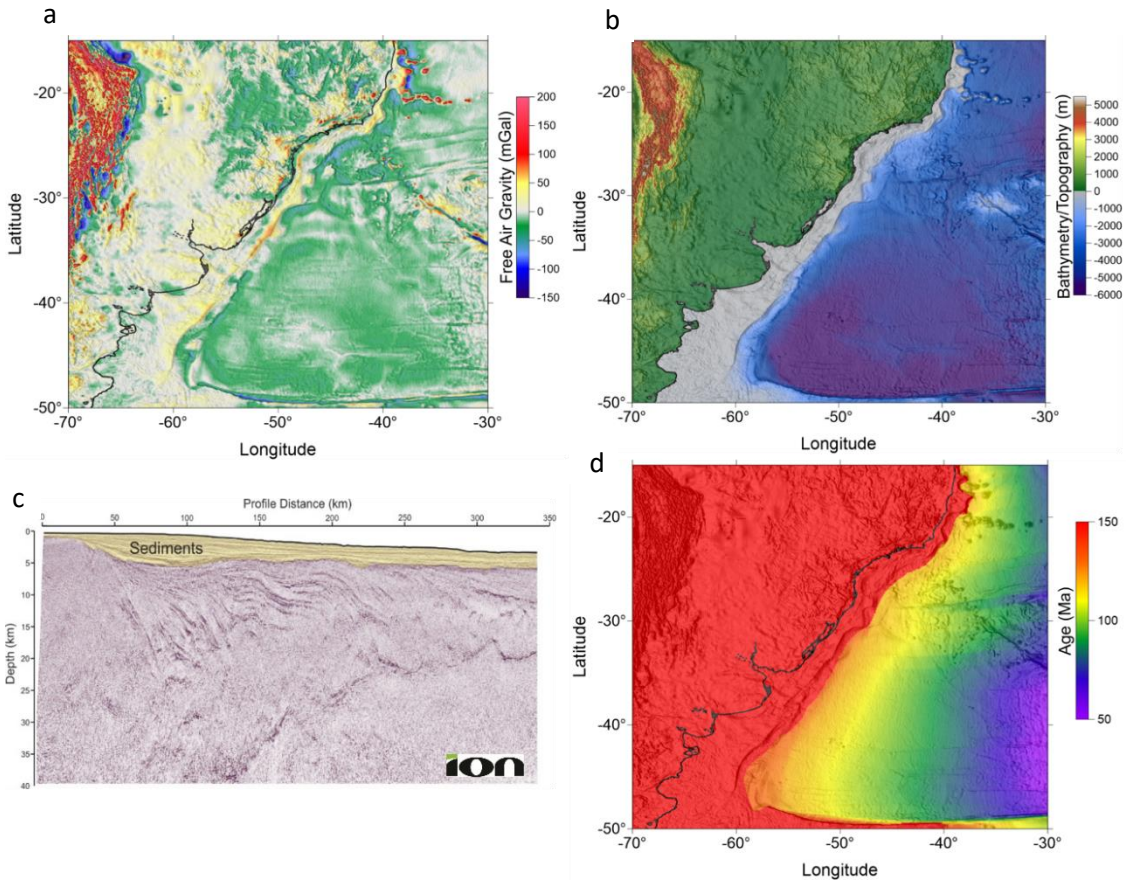

Fig. A.2. Gravity inversion inputs. a) Free air gravity derived from Sandwell and Smith (2009). b) Bathymetry derived from Smith and Sandwell (1997). c) 2D Sediment thickness taken from seismic reflection data. d) Ocean age isochrons taken from Müller et al. (1997).

The gravity inversion starts with the calculation of the mantle residual gravity anomaly (g_{mra}) in equation A.1, which uses free air gravity (g_{fag}) corrected for the effects of bathymetry (g_b), sedimentary material (g_s) and lithosphere thermal effects (g_t).

$$g_{mra} = g_{fag} - g_b - g_s - g_t$$

(A.1)

Using the method of Parker (1972), equation A.2, the mantle residual gravity anomaly is inverted in the 3D spectral domain, which requires assumptions of constant seawater, sediment, basement and mantle densities.

$$F[\Delta g_{mra}] = 2\pi G \Delta\rho e^{-|k|z_0} - \sum_{n=1}^{\infty} \frac{|k|^{n-1}}{n!} F[\Delta r^n]$$

(A.2)

For seawater I assume a constant density of 1030 kg m^{-3} (Nayar et al., 2016; Sharqawy et al., 2010). Sediment density is compaction controlled according to the shaly-sand compaction

parameters from Sclater and Christie (1980). Basement density is taken as 2850 kg m^{-3}, based on seismic velocity analysis, drilling results and laboratory experiments from Carlson and Herrick (1990) and Christensen and Mooney (1995). Joint inversion of seismic and gravity data (Appendix A, Section A.4) tests the assumption of constant basement density by calculating any lateral variations in basement density. A constant density of 3300 kg m^{-3} is assumed for the mantle (Jordan and Anderson, 1974). A Butterworth filter with a cut-off of 100 km and pole-number n=2, is applied to the mantle residual gravity anomaly to remove high frequency components associated with crustal variations. Assuming that the remaining gravity anomaly comes from variations in Moho depth, I invert for Moho relief, Δr, from which the absolute Moho depth is calculated using a reference datum, which is the reference Moho depth, tc_{ref}, (Fig. A.3).

From Moho depth, crustal thickness is calculated by subtracting bathymetry taken from Smith and Sandwell (1997). Using this prediction of crustal thickness and assuming that lithosphere thinning is equal to crustal thinning, the stretching factor, β, can be estimated (McKenzie, 1978), where β is equal to ratio of present-day crustal thickness to initial crustal thickness and ranges from zero to infinity. Lithosphere thinning is directly related to the stretching factor and is defined as γ=1-1/β (Cowie et al., 2015b).

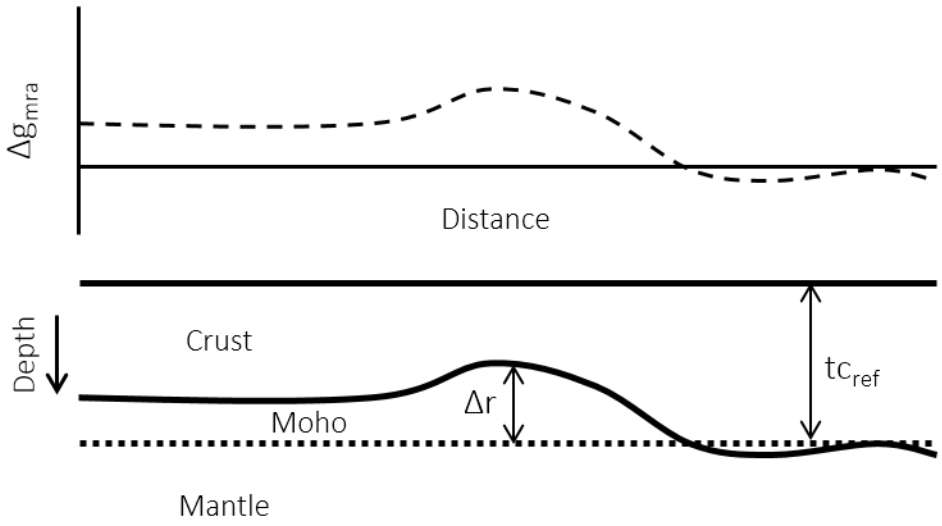

Fig. A.3. Sketch showing how the mantle residual gravity anomaly relates to Moho depth.

The addition of magmatic material to a rifted margin increases crustal thickness, which reduces the lithosphere thinning factor. Parameterisations of the decompression melting models of McKenzie and Bickle (1988) and White and McKenzie (1989) are used to correct for magmatic addition on a rifted margin. Different parameterisations correspond with different types of rifted margins, i.e. magma-poor, magma-rich, 'normal' magmatic and serpentinised mantle. For example, the parameterisation for a 'normal' magmatic rifted predicts a maximum of 7 km magmatic crust (consistent with average oceanic crustal thickness), when full thinning (γ=1.0) is reached, with decompression melting starting when thinning reaches 0.7 (critical thinning factor). Figure A.4 and Table A.1 show the critical thinning factors and maximum magmatic addition for each decompression melting parameterisation.

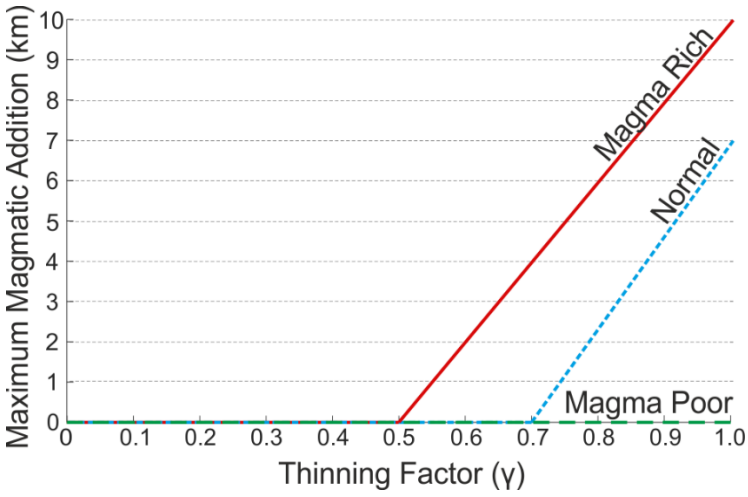

Fig. A.4. End-member decompression melting parameterisations for magma-rich, magma-poor and 'normal' magmatic margins showing critical thinning factor (onset of decompression melting) and maximum magmatic thickness.

Margin Type	Critical Thinning Factor (γ)	Max. Oceanic Crustal Thickness (km)
'Normal' Magmatic	0.7	7.0
Magma-Poor	0.7	0.0
Magma-Rich	0.5	10.0
Serpentinised Mantle	0.7	3.1

Table A.1. Parameters for magmatic addition correction used within the gravity inversion.

At rifted margins and within oceanic lithosphere, the geotherm is elevated due to the stretching and thinning of the crust in continental lithosphere resulting in a large mass deficiency and the lithosphere thermal gravity anomaly. To correct for the lithosphere thermal gravity anomaly a 3D lithosphere thermal model is calculated using present-day

lithosphere temperatures (Chappell and Kusznir, 2008a). Cooling times for oceanic lithosphere are derived from ocean isochrons, while cooling times for rifted continental margin lithosphere uses the breakup age (Chappell and Kusznir, 2008a). Initial estimates of the lithosphere thinning factor in the gravity inversion are used to determine the initial thermal perturbation of continental lithosphere, while in oceanic lithosphere thinning is 1.0 due to the absence of continental crust.

A.1.1. Reference Moho depth calibration

Reference Moho depth is used to convert between inverted Moho relief and absolute Moho depth (Fig. A.3). Dependent on the long wavelength gravity field and controlled by deep mantle processes, the reference Moho depth varies globally. Calibration of the reference Moho depth should be determined by seismic refraction data where possible (Cowie et al., 2015b; Cowie and Kusznir, 2012). In the absence of seismic refraction data, calibration of the seismic Moho in the seismic time domain against various gravity inversion Mohos using different reference depths can be used (Harkin et al., 2019).

A.1.2. Smith's Theorem

Smith's theorem (Smith, 1961), is invoked to overcome the non-uniqueness of general mass systems and their associated gravitational fields. Smith's theorem provides a set of conditions that allow a potential field anomaly and a source distribution to be uniquely associated. These conditions are that the density of the source must remain constant, it must be of finite extent and any vertical line must pass through the body no more than once. To fulfil these conditions, assumptions must be made regarding basement density, the shape of the upper portion of the body (top basement) and the reference plane from which deviations are calculated (reference Moho depth). Within the gravity inversion, Smith's theorem is applied to 3D geometries. To do so an appropriately large grid is selected and all values are tapered to zero at the edge of the grid so that edge effects do not affect the chosen area. The resultant solution is therefore considered unique for that given set of assumptions. If a different set of parameters were chosen then a different solution would be produced. Careful consideration of assumptions is required so that they are realistic. Unreasonable assumptions will still produce a unique mathematical solution however, said solution is likely to be geologically implausible.

A.1.3. Sensitivity to basalt fraction

To investigate the composition of extrusive magmatism on seismic reflection data, I use the sensitivity of Moho depth to varying proportions of basalt to sedimentary/volcaniclastic

material. The proportion of basaltic material to sedimentary/volcaniclastic material is defined as the basalt fraction (BF) and is given as a fraction ranging from 0 to 1, where a basalt fraction of 0.333 represents a mix of 33% basalt to 66% sediments/volcaniclastics.

To calculate the combined density of both basalt and sediments/volcaniclastics I modify the density profile of compaction-controlled shaly-sand material (Sclater and Christie, 1980) to accommodate the inclusion of a basalt-sediment mix. To do so I first assume an empirical porosity-depth relationship (Athy, 1930):

$$\phi(z) = \phi_0 e^{-cz},$$

(A.3)

Where ϕ is porosity, ϕ_0 is surface porosity, c is the reciprocal of compaction length and z is the depth below the sediment surface (Sclater and Christie, 1980). This approximation leads to a bulk density relationship:

$$\rho = \phi\rho_w + (1-\phi)\rho_{mat}\ ,$$

(A.4)

where ρ_{mat} is the matrix density and ρ_w is pore fluid density (Chappell and Kusznir, 2008b). Integration over depth gives average density as a function of depth:

$$\rho_{avg} = \rho_{mat} + \frac{\phi_0(\rho_{mat} - \rho_w)(e^{-cz}-1)}{cz},$$

(A.5)

Alteration of equation (A.5) to include the presence of a layer of mixed basalt and sedimentary material then gives the following density-depth relationship:

$$\rho_{avg} = (1-BF)\left[\rho_{mat} + \frac{\phi_0(\rho_{mat} - \rho_w)(e^{-cz}-1)}{cz}\right] + BF.\rho_b\ ,$$

(A.6)

in which *BF* is the basalt fraction and ρ_b is the density of basalt. When the basalt fraction is 1.0, i.e. a full basaltic scenario is considered, then the sediment component becomes zero and only the non-compactable basalt density is considered.

I assume that the density of basalt is 2850 kg m^{-3} (Moore, 2001) and that it is non-compactable with 0% porosity. For the sedimentary material, all compaction parameters follow those detailed in Sclater & Christie (1980), where for shaly-sand sediment matrix

density is given as 2680 kg m^{-3} (rounded here to 2700 kg m^{-3}), surface porosity is 56% and c is 0.39 km^{-1}.

A.1.4. Lateral variation in basalt fraction

Basalt fraction is analogous to bulk density and used as a proxy for interpretation of composition. Lateral variations in basalt fraction, and therefore composition, can be quantified by combining seismic observations with basalt fraction results. Different basalt fractions used within the gravity inversion will produce Mohos that vary in depth. Minimising the difference between the gravity inversion Mohos that use basalt fraction and the observed interpretation of seismic Moho gives the average basalt fraction across the profile.

A.2. Residual depth anomaly analysis

The residual depth anomaly (RDA) analysis identifies anomalous bathymetries compared against expected bathymetric anomalies, calculated using thermal plate model predictions from Crosby & McKenzie (2009). In order to calculate the RDA, the difference between the observed bathymetry (b_{obs}) and predicted bathymetry (b_{pre}) is taken:

$$RDA = b_{obs} - b_{pre} \quad (A.7)$$

Sensitivities to alternative thermal plate model predictions of b_{pre} have been discussed in Cowie et al., (2015) and are shown to have little variation.

A negative RDA is indicative of crust thinner than the global average of 7 km (White et al., 1992), while a positive RDA indicates that the crust is thicker than the global average of 7 km.

The use of sediment corrected bathymetry to calculate a sediment corrected RDA is important as it removes the effect of sediment loading on the basement. Sediment corrected bathymetries are calculated using 2D flexural backstripping of post-rift sediments (Kusznir et al., 1995) and decompaction of any underlying layers (except basement) assuming shaly-sand compaction parameters (Sclater and Christie, 1980). Removal of post-rift sediments in the calculation of sediment corrected bathymetries requires knowledge of the effective elastic thickness (T_e). Due to the longer wavelength of post-rift sediment loading compared to syn-rift sediment loading, the post-rift isostatic flexural response is insensitive to changes in T_e (Cowie et al., 2015b; Harkin et al., 2019).

The RDA component from crustal basement thickness variations (RDA_{CT}) (Cowie et al., 2015b) is used to investigate anomalous crustal thickness and subsequently, dynamic topography on the margin. The RDA_{CT} is calculated using the difference between crustal basement thickness predicted by the gravity inversion and average global oceanic crustal thickness (White et al., 1992) together using Airy isostasy. By then observing the difference between the sediment corrected RDA and the RDA_{CT}, the effect of present-day mantle dynamic topography can be quantified, where a positive difference is representative of mantle dynamic uplift and a negative difference implies mantle dynamic subsidence.

A.3. Subsidence analysis

Subsidence analysis calculates lithosphere thinning factors independent of the thinning factors calculated in the gravity inversion.

Subsidence analysis begins with the calculation of the sediment-corrected bathymetry, which is an estimation of bathymetry prior to the addition of any post-rift sediments. Post-rift sedimentary layers are removed, the flexural isostatic response is calculated and any underlying layers are decompacted if need be (Roberts et al., 2013). Calculation of sediment-corrected bathymetry assumes shaly-sand compaction parameters (Sclater and Christie, 1980). Sediment corrected bathymetry approximates water-loaded subsidence if the top of the pre-rift sequence is assumed to have been at sea level prior to rifting.

Water-loaded subsidence is assumed to be a combination of initial (S_i) and thermal subsidence (S_t) (McKenzie, 1978). Water-loaded subsidence is converted into thinning factors with a correction for the addition of new magmatic material from decompression melting using a parameterisation melt model of White and McKenzie (1989). Decompression melting is parameterised using the same method as in the gravity inversion (Chappell and Kusznir, 2008a). An example of the relationship between water-loaded subsidence and thinning factor is shown in Figure A.5 for 'normal' decompression melting which produces 7 km thick oceanic crust. As with the gravity inversion, depth-uniform thinning is assumed where the crust and lithosphere are stretched and thinned by the same amount.

The lithosphere thinning factor can be used to establish the oceanward boundary of continental crust and therefore the location of the continent-ocean boundary. A thinning factor of 1.0 suggests complete thinning of continental crust to the point where no continental crust remains, while a low thinning factor of 0.0 suggests no thinning has taken place and the thickness of the continental crust is the initial amount.

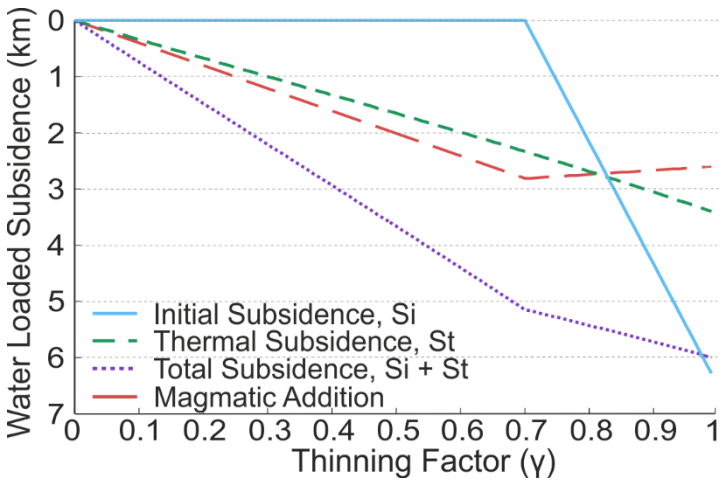

Fig. A.5. Water-loaded subsidence as a function of thinning factor for a 'normal' magmatic solution.

A.1.5. Sensitivity to magmatic addition

As mentioned previously, different parameterisations of decompression melting can be applied within the subsidence analysis. These parameterisations cover different rifted margin end-members, magma-poor, magma-rich, and 'normal' magmatic, details of which are given in Section A.1. For the same water-loaded subsidence, the greater the magmatic addition the higher the thinning factor, as magmatic addition results in thicker crust that isostatically reduces the initial subsidence.

A parameterisation for serpentinised mantle can also be used within the subsidence analysis. The mass deficiency of serpentinised mantle has the same mass deficiency as 3 km thick crustal basement (Cooper, 2010; Cowie et al., 2015b). This mass deficiency is used in the calculation of the isostatic response of the lithosphere within the subsidence analysis. The detailed explanation of how this can be used for subsidence analysis over serpentinised mantle is given in Cowie et al. (2015).

A.3.1. Sensitivity to present-day dynamic topography

Subsidence analysis is an independent way of calculating the lithosphere thinning factor from the gravity inversion but does not directly compensate for mantle dynamic topography. If a margin is experiencing mantle dynamic topography, then thinning factors calculated using subsidence analysis will be underestimated and less than those from gravity inversion. If present-day dynamic topography is known then a correction for it may be applied to the water-loaded subsidence from flexural backstripping, prior to conversion into lithosphere thinning factors.

A.4. Joint inversion of seismic and gravity data

Within the gravity inversion, a constant basement density of 2850 kg m^{-3} is assumed, taken from average continental and oceanic crustal densities (Carlson and Herrick, 1990; Christensen and Mooney, 1995), however global basement composition is known to vary greatly so lateral heterogeneities may exist. The joint inversion can test for any lateral heterogeneities within the basement and calculate the associated density and velocity variations.

Allowing for any lateral variations, I solve for the density and seismic velocity of the basement by matching the gravity inversion Moho with the seismic Moho in the time domain. To do so I use a linear Nafe-Drake relationship (Brocher, 2005; Ludwig et al., 1970) to link seismic velocity to basement density. This empirical linear relationship, defined as $V_p = 3.49.\rho - 3.46$, gives a seismic velocity of 6.31 km s^{-1} for an equivalent basement density of 2850 kg m^{-3}, which is used as the constant basement density in the gravity inversion.

The methodology is described by Cowie et al. (2016) and Harkin et al. (2019), and begins with the conversion of the gravity inversion Moho in depth into two-way travel time. For the conversion of the gravity inversion Moho we assume that the sediment thickness derived from seismic reflection interpretation and depth conversion is correct. Crustal thickness is calculated using the distance between top basement and the gravity inversion Moho, converted into two-way travel time (TWTT) as an interval TWTT. This interval is added to the seismic interpretation of top basement in the time domain to give the gravity inversion Moho in TWTT.

When comparing the gravity inversion Moho and a seismic interpretation of the Moho, any differences between the two in the time domain are assumed to be due to lateral heterogeneities within the basement. By adjusting the seismic velocity and basement density across the profile the difference between the two Mohos is minimised. When adjusting the basement density, depth to the gravity inversion Moho is affected, while adjustment of seismic velocity affects the conversion of the Moho from gravity inversion into the time domain. Both seismic velocity and basement density are iteratively adjusted until the gravity inversion Moho converges with the observed seismic Moho. Working in the time domain avoids uncertainties associated with velocity models in the depth domain.

A.4.1. Density-velocity relationships

Within the joint inversion of seismic and gravity data a linear Nafe-Drake relationship (Brocher, 2005; Ludwig et al., 1970) is used to convert between density and velocity. Other

density-velocity relationships exist (Fig. A.6.), including a non-linear Nafe-Drake relationship (Ludwig et al., 1970), the Carlson-Herrick solution (Carlson and Herrick, 1990) and those by Birch (Birch, 1961, 1964). When comparing relationships I used average densities and velocities of oceanic crust as a measure of the accuracy of each relationship. For average oceanic crust consisting of layers 2 and 3 that have average thicknesses of 2 km and 5 km respectively with corresponding seismic velocities of ~5 km s^{-1} and 6.7 km s^{-1} respectively (Carlson and Herrick, 1990; White et al., 1992), the average seismic velocity is ~6.1 km s^{-1}. The average density of oceanic crust is given as 2860 kg m^{-3} (Carlson and Herrick, 1990). Both the linear Nafe-Drake relationship (Ludwig et al., 1970) and the Carlson-Herrick relationship (Carlson and Herrick, 1990) fit with these average density-velocity measurements. However, at low densities the Carlson-Herrick solution becomes unstable so the linear Nafe-Drake relationship is preferred.

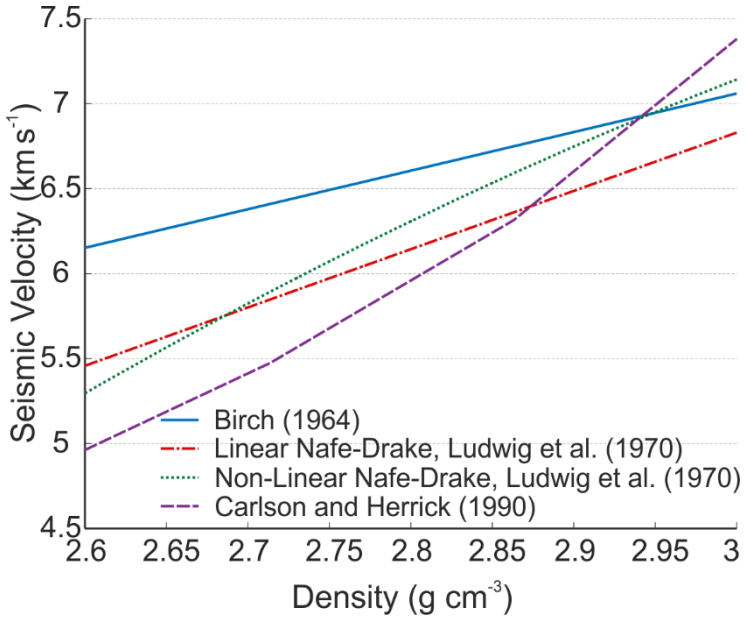

Fig. A.6. Density-velocity relationships.

A.5. Palaeobathymetry analysis

Palaeobathymetry predications are calculated through reverse post-rift thermal subsidence modelling that incorporates the flexural isostatic response to the removal of overlying sedimentary layers and decompaction of any underlying layers (Cowie et al., 2015a; Kusznir et al., 1995; Roberts et al., 1998).

The calculation of palaeobathymetries follows a set workflow defined by Roberts et al. (1998), which is as follows:

1. Removal of the water layer and calculation of the flexural isostatic response.
2. Removal of the top stratigraphic unit and decompaction of the underlying layers according to pre-set compaction parameters.
3. The flexural isostatic response to the removed layer is calculated.
4. Reversal of thermal subsidence in the form of thermal uplift, calculated using a 2D form of the McKenzie (1978) post-rift thermal subsidence model (Roberts et al., 1998). Within the 2D McKenzie model estimates of the stretching factor (β) are required which are calculated from the lithosphere thinning factor produced in the gravity inversion.
5. If needed, a correction is made for any long-term eustatic sea-level changes.
6. A cross section of the profile is produced that is isostatically balanced with the top stratigraphic unit removed.
7. Steps 1-6 are repeated for remaining stratigraphic units.

During decompaction, the density and porosity of layers are adjusted so that they correspond to the newly calculated depth. To do so we must know the compaction parameters which are surface porosity (ϕ_0), matrix density (ρ_{mat}) and compaction length (c). We derive these compaction parameters by integrating Athy's relationship (1930) and a bulk density-porosity relationship over depth (z) to give:

$$\rho_{avg}(z) = \rho_{mat} + \frac{\phi_0(\rho_{mat} - \rho_{water})(e^{-cz} - 1)}{cz} \quad (A.5)$$

Within our palaeobathymetry analysis, sections are restored to a present day isostatic datum meaning that past dynamic topography is not accounted for. Without other evidence for thermal calibration, such as well data, we cannot make accurate predictions of dynamic topography at the time of margin formation. However, dynamic topography should still be

considered within the results, so the sensitivity to dynamic topography is investigated by exploring a range of uplifts up to 1 km.

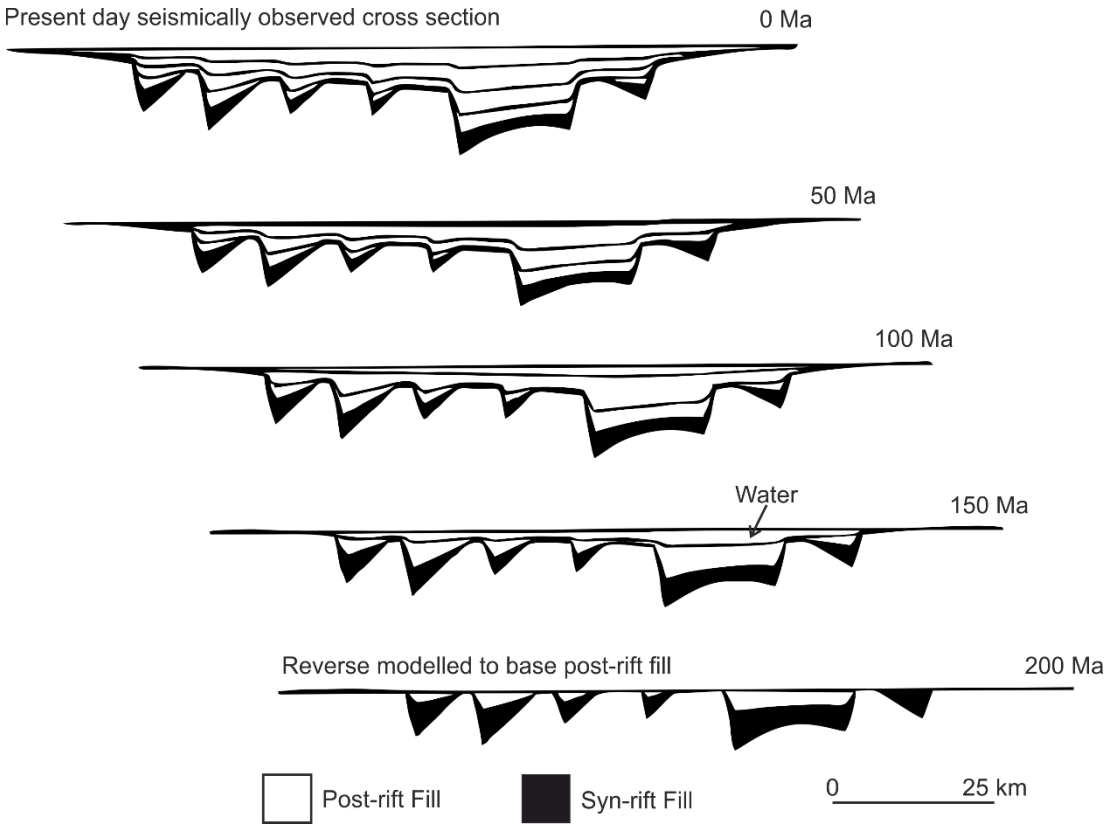

Fig. A.7. Schematic illustration of 2D post-rift thermal subsidence modelling incorporating flexural backstripping and decompaction after Roberts et al. (1998)

A.6. Seismic velocity analysis

Basement velocity is calculated using seismic observations to obtain travel times and distances, which are related to velocity using the velocity-time-distance relationship where velocity = distance/time.

In the time domain, the travel time between the seismic interpretation of top basement and seismic Moho is calculated. Similarly, in the depth domain, the distance between top basement and seismic Moho is calculated. As per the velocity-distance-time relationship, the distance between top basement and seismic Moho is divided by the equivalent in time to give the velocity of the basement. Calculating the basement seismic velocity across the seismic profile can reveal any lateral changes that may relate to composition.

The relationship between seismic velocity (V_p) and basement thickness (H), H-V_p, corrected for pressure and temperature, can be used to indicate bulk crustal composition and the degree of mixing within igneous melt (Holbrook and Kelemen, 1993; Hopper et al., 2003; Korenaga et al., 2002; White and Smith, 2009). No correction for a reference pressure and temperature is made due to the ambiguity of choosing a reference pressure and temperature. Using this relationship, we can make interpretations regarding mantle temperature and mantle upwelling. For example, thicker crust formed from a melt originating from deep within the mantle will have seen higher the temperatures, and so will have a higher magnesium content resulting in a higher seismic velocity. If active upwelling has taken place, it will allow for the production of thicker crust from a shallower depth due to the regular movement of material across the solidus without needing an increased velocity.

When calculating estimates of basement velocity we do not set an upper crustal velocity to compensate for any alteration of the upper crust to avoid any ambiguity, nor do we separate out the SDRs and basement due to uncertainty of the boundary between the two.

Bibliography

Alvey, A., Gaina, C., Kusznir, N.J., Torsvik, T.H., 2008. Integrated crustal thickness mapping and plate reconstructions for the high Arctic. Earth Planet. Sci. Lett. 274, 310–321. https://doi.org/10.1016/j.epsl.2008.07.036

Armitage, J.J., Henstock, T.J., Minshull, T.A., Hopper, J.R., 2009. Lithospheric controls on melt production during continental breakup at slow rates of extension: Application to the North Atlantic. Geochemistry, Geophys. Geosystems 10. https://doi.org/10.1029/2009GC002404

Athy, L.F., 1930. Density, porosity and compaction of sedimentary rocks. Am. Assoc. Pet. Geol. Bull. 14, 1–24.

Barton, A.J., White, R.S., 1997. Volcanism on the Rockall continental margin. J. Geol. Soc. London. 154, 531–536. https://doi.org/10.1144/gsjgs.154.3.0531

Bastow, I.D., Pilidou, S., Kendall, J.M., Stuart, G.W., 2010. Melt-induced seismic anisotropy and magma assisted rifting in Ethiopia: Evidence from surface waves. Geochemistry, Geophys. Geosystems 11, 1–19. https://doi.org/10.1029/2010GC003036

Bergh, S.G., Sigvaldason, G.E., 1991. Pleistocene mass-flow deposits of basaltic hyaloclastite on a shallow submarine shelf, South Iceland. Bull. Volcanol. 53, 597–611. https://doi.org/10.1007/BF00493688

Birch, F., 1964. Density and composition of mantle and core. J. Geophys. Res. 69, 4377. https://doi.org/10.1029/JZ069i020p04377

Birch, F., 1961. The Velocity of Compressional Waves in Rocks to 10 Kilobars, Part 2. J. Geophys. Res. 66, 91–116. https://doi.org/10.1029/sp026p0091

Blaich, O.A., Faleide, J.I., Tsikalas, F., Gordon, A.C., Mohriak, W.U., 2013. Crustal-scale architecture and segmentation of the South Atlantic volcanic margin. Geol. Soc. London, Spec. Publ. 369, 167–183. https://doi.org/10.1144/sp369.22

Bodvarsson, G., Walker, G.P.L., 1964. Crustal Drift in Iceland. Geophys. J. R. Astron. Soc. 8, 285–300.

Boillot, G., Feraud, G., Recq, M., Giradeau, J., 1989. Undercrusting by Serpentinite beneath Rifted Margins. Nature 342, 189–92. https://doi.org/10.1038/340301a0

Bonatti, E., 1965. Palagonite, hyaloclastites and alteration of volcanic glass in the ocean. Bull. Volcanol. 28, 257–269. https://doi.org/10.1007/BF02596930

Borissova, I., Coffin, M.F., Charvis, P., Operto, S., 2003. Structure and development of a microcontinent: Elan Bank in the southern Indian Ocean. Geochemistry, Geophys. Geosystems 4, 1–16. https://doi.org/10.1029/2003GC000535

Bradley, D.C., 2008. Passive margins through earth history. Earth-Science Rev. 91, 1–26. https://doi.org/10.1016/j.earscirev.2008.08.001

Brocher, T.M., 2005. Empirical relations between elastic wavespeeds and density in the Earth's crust. Bull. Seismol. Soc. Am. 95, 2081–2092. https://doi.org/10.1785/0120050077

Brun, J.P., 1999. Narrow rifts versus wide rifts: inferences for the mechanics of rifting from laboratory experiments. Philos. Trans. R. Soc. A Math. Phys. Eng. Sci. 357, 695–712. https://doi.org/10.1098/rsta.1999.0349

Brune, S., Heine, C., Pérez-Gussinyé, M., Sobolev, S. V., 2014. Rift migration explains continental margin asymmetry and crustal hyper-extension. Nat. Commun. 5, 4014. https://doi.org/10.1038/ncomms5014

Buck, W.R., 2017. The role of magmatic loads and rift jumps in generating seaward dipping reflectors on volcanic rifted margins. Earth Planet. Sci. Lett. 466, 62–69. https://doi.org/10.1016/j.epsl.2017.02.041

Buck, W.R., 1986. Small-scale convection induced by passive rifting: the cause for uplift of rift shoulders. Earth Planet. Sci. Lett. 77, 362–372.

Carlson, R.L., Herrick, C.N., 1990. Densities and porosities in the oceanic crust and their variations with depth and age. J. Geophys. Res. 95, 9153. https://doi.org/10.1029/JB095iB06p09153

Chand, S., Radhakrishna, M., Subrahmanyam, C., 2001. India-East Antarctica conjugate margins: Rift-shear tectonic setting inferred from gravity and bathymetry data. Earth Planet. Sci. Lett. 185, 225–236. https://doi.org/10.1016/S0012-821X(00)00349-6

Chappell, A.R., Kusznir, N.J., 2008a. Three-dimensional gravity inversion for Moho depth at rifted continental margins incorporating a lithosphere thermal gravity anomaly correction. Geophys. J. Int. 174, 1–13. https://doi.org/10.1111/j.1365-246X.2008.03803.x

Chappell, A.R., Kusznir, N.J., 2008b. An algorithm to calculate the gravity anomaly of sedimentary basins with exponential density-depth relationships. Geophys. Prospect. 56, 249–258. https://doi.org/10.1111/j.1365-2478.2007.00674.x

Charvis, P., Operto, S., 1999. Structure of the Cretaceous Kerguelen Volcanic Province (southern Indian Ocean) from wide-angle seismic data. J. Geodyn. 28, 51–71. https://doi.org/10.1016/S0264-3707(98)00029-5

Charvis, P., Recq, M., Operto, S., Brefort, D., 1995. Deep structure of the northern Kerguelen Plateau and hotspot-related activity. Geophys. J. Int. 122, 899–924. https://doi.org/10.1111/j.1365-246X.1995.tb06845.x

Chenin, P., Schmalholz, S.M., Manatschal, G., Karner, G.D., 2018. Necking of the Lithosphere: A Reappraisal of Basic Concepts With Thermo-Mechanical Numerical Modeling. J. Geophys. Res. Solid Earth 123, 5279–5299. https://doi.org/10.1029/2017JB014155

Chian, D.P., Louden, K.E., Reid, I., 1995. Crustal structure of the Labrador Sea conjugate margin and implications for the formation of nonvolcanic continental margins. J. Geophys. Res. Earth 100, 24239–24253. https://doi.org/10.1029/95JB02162

Christensen, M.I., Mooney, W.D., 1995. Seismic velocity structure and composition of the continental crust - a global view. J. Geophys. Res. Earth 100, 9761–9788. https://doi.org/https://doi.org/10.1029/95JB00259

Clerc, C., Ringenbach, J.C., Jolivet, L., Ballard, J.F., 2018. Rifted margins: Ductile deformation, boudinage, continentward-dipping normal faults and the role of the weak lower crust. Gondwana Res. 53, 20–40. https://doi.org/10.1016/j.gr.2017.04.030

Coffin, M.F., Eldholm, O., 1994. Large igneous provinces: crustal structure, dimensions, and

external consequences. Rev. Geophys. 1–36. https://doi.org/10.1029/93RG02508

Coffin, M.F., Eldholm, O., 1992. Volcanism and continental break-up: a global compilation of large igneous provinces. Geol. Soc. London, Spec. Publ. 68, 17–30. https://doi.org/10.1144/GSL.SP.1992.068.01.02

Coffin, M.F., Storey, M., Müller, R.D., Gahagan, L. a., Pringle, M.S., Duncan, R.A., Gladczenko, T.P., 2002. Kerguelen hotspot magma output since 130 Ma. J. Petrol. 43, 1121–1139. https://doi.org/10.1093/petrology/43.7.1121

Cole, P.B., Minshull, T.A., Whitmarsh, R.B., 2002. Azimuthal seismic anisotropy in a zone of exhumed continental mantle, West Iberia margin. Geophys. J. Int. 151, 517–533. https://doi.org/10.1046/j.1365-246X.2002.01781.x

Connor, J.M.O., Duncan, A., 1990. Evolution of the Walvis Ridge-Rio Grande Rise Hot Spot System: Implications for African and South American Plate Motions Over Plumes. J. Geophys. Res. 95, 17475–17502.

Cooper, C., 2010. Anomalous bathymetry and mass heterogeneity at the conjugate Iberia and Newfoundland rifted margins.

Courtillot, V., Jaupart, C., Manighetti, I., Tapponnier, P., Besse, J., 1999. On causal links between flood basalts and continental breakup. Earth Planet. Sci. Lett. 166, 177–195. https://doi.org/10.1016/S0012-821X(98)00282-9

Cowie, L., Angelo, R.M., Kusznir, N.J., Manatschal, G., Horn, B., 2016. Structure of the ocean-continent transition, location of the continent-ocean boundary and magmatic type of the northern Angolan margin from integrated quantitative analysis of deep seismic reflection and gravity anomaly data. Geol. Soc. London, Spec. Publ. 438, 159–176. https://doi.org/10.1144/SP438.6

Cowie, L., Angelo, R.M., Kusznir, N.J., Manatschal, G., Horn, B., 2015a. The palaeo-bathymetry of base Aptian salt deposition on the northern Angolan rifted margin: constraints from flexural back-stripping and reverse post-break-up thermal subsidence modelling. Pet. Geosci. 2014–087. https://doi.org/10.1144/petgeo2014-087

Cowie, L., Kusznir, N., 2012. Mapping crustal thickness and oceanic lithosphere distribution in the Eastern Mediterranean using gravity inversion. Pet. Geosci. 18, 373–380. https://doi.org/10.1144/petgeo2011-071

Cowie, L., Kusznir, N.J., Manatschal, G., 2015b. Determining the COB location along the Iberian margin and Galicia Bank from gravity anomaly inversion, residual depth anomaly and subsidence analysis. Geophys. J. Int. 203, 1355–1372. https://doi.org/10.1093/gji/ggv367

Cox, K.G., 1993. Continental Magmatic Underplating. Philos. Trans. R. Soc. A Math. Phys. Eng. Sci. 342, 155–166. https://doi.org/10.1098/rsta.1993.0011

Crosby, A.G., McKenzie, D., 2009. An analysis of young ocean depth, gravity and global residual topography. Geophys. J. Int. 178, 1198–1219. https://doi.org/10.1111/j.1365-246X.2009.04224.x

Dahl-Jensen, T., Thybo, H., Hopper, J., Rosing, M., 1998. Crustal structure at the SE Greenland margin from wide-angle and normal incidence seismic data. Tectonophysics 288, 191–198. https://doi.org/10.1016/S0040-1951(97)00292-8

Davis, J.K., Lavier, L.L., 2017. Influences on the development of volcanic and magma-poor

morphologies during passive continental rifting. Geosphere 13, 1524–1540. https://doi.org/10.1130/GES01538.1

Davis, M., Kusznir, N., 2004. Depth-Dependent Lithospheric Stretching at Rifted Continental Margins. Proc. NSF Rift. Margins Theor. Inst. 136, 92–137. https://doi.org/10.7312/karn12738-005

Davison, I., 1997. Wide and narrow margins of the Brazilian South Atlantic. J. Geol. Soc. London. 154, 471–476. https://doi.org/10.1144/gsjgs.154.3.0471

Decarlis, A., Manatschal, G., Haupert, I., Masini, E., 2015. The tectono-stratigraphic evolution of distal, hyper-extended magma-poor conjugate rifted margins: Examples from the Alpine Tethys and Newfoundland-Iberia. Mar. Pet. Geol. 68, 54–72. https://doi.org/10.1016/j.marpetgeo.2015.08.005

Doré, T., Lundin, E., 2015. Hyperextended continental margins — Knowns and unknowns. Geology 43, 95–96. https://doi.org/10.1016/0040

Eldholm, O., 1972. Continental Margin off Norway: A Geophysical Study. Geol. Soc. Am. Bull. 83, 3575–3606.

Eldholm, O., Thiede, J., Taylor, A., 1987. Evolution of the Norwegian Continental margin - background and objectives. Proc. Ocean Drill. Program, Sci. Results 104, 5–25. https://doi.org/10.2973/odp.proc.ir.104.1987

Eldholm, O., Thiede, J., Taylor, E., 1989. Evolution of the Vøring Volcanic Margin. Proc. Ocean Drill. Program, 104 Sci. Results 104, 1033–1065. https://doi.org/10.2973/odp.proc.sr.104.191.1989

Ernesto, M., Marques, L.S., Piccirillo, E.M., Molina, E.C., Ussami, N., Comin-Chiaramonti, P., Bellieni, G., 2002. Parana Magmatic Province-Tristan da Cunha plume system: Fixed versus mobile plume, petrogenetic considerations and alternative heat sources. J. Volcanol. Geotherm. Res. 118, 15–36. https://doi.org/10.1016/S0377-0273(02)00248-2

Fioravanti, C., 2014. Echoes of Separation. Pesqui. FAPESP 42–45.

Fitton, J.G., Larsen, L.M., Saunders, A.D., Hardarson, B.S., Kempton, P.D., 2000. Palaeogene continental to oceanic magmatism on the SE Greenland continental margin at 63°N: A review of the results of Ocean Drilling Program Legs 152 and 163. J. Petrol. 41, 951–966. https://doi.org/10.1093/petrology/41.7.951

Fletcher, R., Kusznir, N.J., Cheadle, M., 2009. Melt initiation and mantle exhumation at the Iberian rifted margin: Comparison of pure-shear and upwelling-divergent flow models of continental breakup. Comptes Rendus - Geosci. 341, 394–405. https://doi.org/10.1016/j.crte.2008.12.008

Fletcher, R., Kusznir, N.J., Roberts, A.M., Hunsdale, R., 2013. The formation of a failed continental breakup basin: The Cenozoic development of the Faroe-Shetland Basin. Basin Res. 25, 532–553. https://doi.org/10.1111/bre.12015

Franke, D., 2013. Rifting, lithosphere breakup and volcanism: Comparison of magma-poor and volcanic rifted margins. Mar. Pet. Geol. 43, 63–87. https://doi.org/10.1016/j.marpetgeo.2012.11.003

Frey, F.A., Coffin, M.F., Wallace, P.J., Weis, D., Zhao, X., Wise, S.W., Wähnert, V., Teagle, D., Saccocia, P.J., Reusch, D.N., Pringle, M.S., Nicolaysen, K.E., Neal, C.R., Müller, R.D.,

Moore, C.L., Mahoney, J.J., Keszthelyi, L., Inokuchi, H., Duncan, R.A., Delius, H., Damuth, J.E., Damasceno, D., Coxall, H.K., Borre, M.K., Boehm, F., Barling, J., Arndt, N.T., Antretter, M., 2000. Origin and evolution of a submarine large igneous province: The Kerguelen Plateau and Broken Ridge, southern Indian Ocean. Earth Planet. Sci. Lett. 176, 73–89. https://doi.org/10.1016/S0012-821X(99)00315-5

Frolova, J., Ladygin, V., Franzson, H., Sigurðsson, O., Stefánsson, V., Shustrov, V., 2005. Petrophysical Properties of Fresh to Mildly Altered Hyaloclasitie Tuffs. Proc. World Geotherm. Congr. 24–29.

Frolova, Y. V., 2008. Specific features in the composition, structure, and properties of volcaniclastic rocks. Moscow Univ. Geol. Bull. 63, 28–37. https://doi.org/10.3103/S0145875208010043

Fromm, T., Planert, L., Jokat, W., Ryberg, T., Behrmann, J.H., Weber, M.H., Haberland, C., 2015. South Atlantic opening : A plume-induced breakup? Geology 43, 931–934. https://doi.org/10.1130/G36936.1

Funck, T., Erlendsson, Ö., Geissler, W.H., Gradmann, S., Kimbell, G.S., McDermott, K., Petersen, U.K., 2017. A review of the NE Atlantic conjugate margins based on seismic refraction data. Geol. Soc. London, Spec. Publ. 447, 171–205. https://doi.org/10.1144/SP447.9

Funck, T., Geissler, W.H., Kimbell, G.S., Gradmann, S., Erlendsson, Ö., McDermott, K., Petersen, U.K., 2016. Moho and basement depth in the NE Atlantic Ocean based on seismic refraction data and receiver functions. Geol. Soc. London, Spec. Publ. 447, 207–231. https://doi.org/10.1144/SP447.1

Gaina, C., Müller, R.D., Brown, B., Ishihara, T., 2003. Microcontinent formation around Australia. Geol. Soc. Am. Spec. Pap. 372 405–416. https://doi.org/10.1130/0-8137-2372-8.405

Gaina, C., Müller, R.D., Brown, B., Ishihara, T., Ivanov, S., 2007. Breakup and early seafloor spreading between India and Antarctica. Geophys. J. Int. 170, 151–169. https://doi.org/10.1111/j.1365-246X.2007.03450.x

Geoffroy, L., 2005. Volcanic passive margins. Comptes Rendus - Geosci. 337, 1395–1408. https://doi.org/10.1016/j.crte.2005.10.006

Geoffroy, L., Callot, J.-P., Scaillet, S., Skuce, A., Gelard, J.P., Ravilly, M., Angelier, J., Bonin, B., Cayet, C., Perrots, K., Lepvrier, C., 2001. Southeast Baffin volcanic margin and the North American-Greenland plate separation. Tectonics 20, 566–584. https://doi.org/https://doi.org/10.1029/2001tc900003

Gernigon, L., Lucazeau, F., Brigaud, F., Ringenbach, J.C., Planke, S., Le Gall, B., 2006. A moderate melting model for the Vøring margin (Norway) based on structural observations and a thermo-kinematical modelling: Implication for the meaning of the lower crustal bodies. Tectonophysics 412, 255–278. https://doi.org/10.1016/j.tecto.2005.10.038

Gernigon, L., Ringenbach, J.C., Planke, S., Le Gall, B., 2004. Deep structures and breakup along volcanic rifted margins: Insights from integrated studies along the outer Vøring Basin (Norway). Mar. Pet. Geol. 21, 363–372. https://doi.org/10.1016/j.marpetgeo.2004.01.005

Gibbons, A.D., Whittaker, J.M., Müller, R.D., 2013. The breakup of East Gondwana:

Assimilating constraints from Cretaceous ocean basins around India into a best-fit tectonic model. J. Geophys. Res. Solid Earth 118, 808–822. https://doi.org/10.1002/jgrb.50079

Gibson, I.L., Love, D., 1989. A Listric Fault Model for the Formation of the Dipping Reflectors Penetrated during the Drilling of Hole 642E, ODP Leg 104. Proc. Ocean Drill. Program, 104 Sci. Results. https://doi.org/10.2973/odp.proc.sr.104.195.1989

Gillard, M., Autin, J., Manatschal, G., 2016. Fault systems at hyper-extended rifted margins and embryonic oceanic crust: Structural style, evolution and relation to magma. Mar. Pet. Geol. 76, 51–67. https://doi.org/10.1016/j.marpetgeo.2016.05.013

Gillard, M., Autin, J., Manatschal, G., Sauter, D., Munschy, M., Schaming, M., 2015. Tectonomagmatic evolution of the final stages of rifting along the deep conjugate Australian-Antarctic magma-poor rifted margins: Constraints from seismic observations. Tectonics 34, 753–783. https://doi.org/10.1002/2015TC003850.Received

Gillard, M., Sauter, D., Tugend, J., Tomasi, S., Epin, M.E., Manatschal, G., 2017. Birth of an oceanic spreading center at a magma-poor rift system. Sci. Rep. 7. https://doi.org/10.1038/s41598-017-15522-2

Gladczenko, T.P., Hinz, K., Eldholm, O., Meyer, H., Neben, S., Skogseid, J., 1997. South Atlantic volcanic margins. J. Geol. Soc. London. 154, 465–470. https://doi.org/10.1144/gsjgs.154.3.0465

Graça, M., 2018. A formação da Elevação do Rio Grande e sua correlação com a evolução da Margem Continental Sudeste Brasileira.

Gradstein, F.M., Agterberg, F.P., Ogg, J.G., Hardenbol, J., van Veen, P., Thierry, J., Huang, Z., 1994. A Mesozoic Time-Scale. J. Geophys. Res. Earth 99, 24051–24074. https://doi.org/10.1029/94JB01889

Granot, R., Dyment, J., 2015. The Cretaceous opening of the South Atlantic Ocean. Earth Planet. Sci. Lett. 414, 156–163. https://doi.org/10.1016/j.epsl.2015.01.015

Greenhalgh, E.E., Kusznir, N.J., 2007. Evidence for thin oceanic crust on the extinct Aegir Ridge, Norwegian Basin, NE atlantic derived from satellite gravity inversion. Geophys. Res. Lett. 34, 1–5. https://doi.org/10.1029/2007GL029440

Harkin, C., Kusznir, N., Tugend, J., Manatschal, G., McDermott, K., 2019. Evaluating magmatic additions at a magma-poor rifted margin: An East Indian case study. Geophys. J. Int. 25–40. https://doi.org/10.1093/gji/ggz007

Harry, D.L., Sawyer, D.S., 1992. Basaltic volcanism, mantle plumes, and the mechanics of rifting: the Parana flood basalt province of South America. Geology 20, 207–210. https://doi.org/10.1130/0091-7613(1992)020<0207:BVMPAT>2.3.CO;2

Haupert, I., Manatschal, G., Decarlis, A., Unternehr, P., 2016. Upper-plate magma-poor rifted margins: Stratigraphic architecture and structural evolution. Mar. Pet. Geol. 69, 241–261. https://doi.org/10.1016/j.marpetgeo.2015.10.020

Hawkesworth, C.J., Gallagher, K., Kirstein, L., Mantovani, M.S.M., 2000. Tectonic controls on magmatism associated with continental break-up : an example from the Paranà-Etendeka Province. Earth Planet. Sci. Lett. 179, 335–349. https://doi.org/10.1016/S0012-821X(00)00114-X

Hawkesworth, C.J.Y., Gallagher, K., Kelley, S., Mantovani, M., Peate, D.W., Regelous, M.,

Rogers, N.W., 1992. Paraná magmatism and the opening of the South Atlantic. Geol. Soc. London, Spec. Publ. Magmatism, 221–240. https://doi.org/https://doi.org/10.1144/gsl.sp.1992.068.01.14

Heine, C., Zoethout, J., Müller, R.D., 2013. Kinematics of the South Atlantic rift. Solid Earth 4, 215–253. https://doi.org/10.5194/se-4-215-2013

Hill, R.I., 1991. Starting plumes and continental break-up. Earth Planet. Sci. Lett. 104, 398–416. https://doi.org/10.1016/0012-821X(91)90218-7

Hinz, K., 1981. A Hypothesis on Terrestrial Catastrophes. Geol. Jahrb. R. E.

Hinz, K., Neben, S., Schreckenberger, B., Roeser, H.A., Block, M., Souza, K.G. De, Meyer, H., 1999. The Argentine continental margin north of 48°S: Sedimentary successions, volcanic activity during breakup. Mar. Pet. Geol. 16, 1–25. https://doi.org/10.1016/S0264-8172(98)00060-9

Holbrook, W.S., Kelemen, P.B., 1993. Large igneous province on the US Atlantic margin and implications for magmatism during continental breakup. Nature 364, 433–436. https://doi.org/10.1038/364433a0

Holbrook, W.S., Larsen, H.C., Korenaga, J., Dahl-Jensen, T., Reid, I.D., Kelemen, P.B., Hopper, J.R., Kent, G.M., Lizarralde, D., Bernstein, S., Detrick, R.S., 2001. Mantle thermal structure and active upwelling during continental breakup in the North Atlantic. Earth Planet. Sci. Lett. 190, 251–266. https://doi.org/10.1016/S0012-821X(01)00392-2

Hopper, J.R., Dahl-Jensen, T., Holbrook, W.S., Larsen, H.C., Lizarralde, D., Korenaga, J., Kent, G.M., Kelemen, P.B., 2003. Structure of the SE Greenland margin from seismic reflection and refraction data: Implications for nascent spreading center subsidence and asymmetric crustal accretion during North Atlantic opening. J. Geophys. Res. 108, 61–64. https://doi.org/10.1029/2002jb001996

Hopper, J.R., Funck, T., Tucholke, B.E., Larsen, H.C., Holbrook, W.S., Louden, K.E., Shillington, D.J., Lau, H., 2004. Continental break-up and the onset of ultraslow seafloor spreading off Flemish Cap on the Newfoundland rifted margin. Geology 32, 93–96. https://doi.org/10.1130/G19694.1

Ingle, S., Weis, D., Frey, F.A., 2002a. Indian Continental Crust Recovered from Elan Bank, Kerguelen Plateau (ODP Leg 183, Site 1137). J. Petrol. 43, 1241–1257. https://doi.org/10.1093/petrology/43.7.1241

Ingle, S., Weis, D., Scoates, J.S., Frey, F.A., 2002b. Relationship between the early Kerguelen plume and continental flood basalts of the paleo-Eastern Gondwanan margins. Earth Planet. Sci. Lett. 197, 35–50. https://doi.org/10.1016/S0012-821X(02)00473-9

Jeanniot, L., Kusznir, N., Mohn, G., Manatschal, G., Cowie, L., 2016. Constraining lithosphere deformation modes during continental breakup for the Iberia-Newfoundland conjugate rifted margins. Tectonophysics 680, 28–49. https://doi.org/10.1016/j.tecto.2016.05.006

Jordan, T.H., Anderson, D.L., 1974. Earth Structure from Free Oscillations and Travel Times. Geophys. J. R. Astron. Soc. 36, 411–459. https://doi.org/10.1111/j.1365-246X.1974.tb03648.x

Karner, G.D., Driscoll, N.W., 1999. Tectonic and stratigraphic development of the West African and eastern Brazilian Margins: insights from quantitative basin modelling. Geol. Soc. London, Spec. Publ. 153, 11–40. https://doi.org/10.1144/GSL.SP.1999.153.01.02

Keen, C., Peddy, C., De Voogd, B., Matthews, D., 1989. Conjugate margins of Canada and Europe: results from deep reflection profiling. Geology 17, 173–176. https://doi.org/10.1130/0091-7613(1989)017<0173:CMOCAE>2.3.CO;2

Kendall, J.M., Stuart, G.W., Ebinger, C.J., Bastow, I.D., Keir, D., 2005. Magma-assisted rifting in Ethiopia. Nature 433, 146–148. https://doi.org/10.1038/nature03161

Korenaga, J., Holbrook, W.S., Detrick, R.S., Kelemen, P.B., 2001. Gravity anomalies and crustal structure at the southeast Greenland margin. J. Geophys. Res. 106, 8853. https://doi.org/10.1029/2000JB900416

Korenaga, J., Holbrook, W.S., Kent, G.M., Kelemen, P.B., Detrick, R.S., Larsen, H.C., Hopper, J.R., Dahl-Jensen, T., 2000. Crustal structure of the southeast Greenland margin from joint refraction and reflection seismic tomography. J. Geophys. Res. 105, 21591. https://doi.org/10.1029/2000JB900188

Korenaga, J., Kelemen, P.B., Holbrook, W.S., 2002. Methods for resolving the origin of large igneous provinces from crustal seismology. J. Geophys. Res. Solid Earth 107, ECV 1-1-ECV 1-27. https://doi.org/10.1029/2001JB001030

Kusznir, N., Karner, G., 1985. Dependence of the flexural rigidity of the continental lithosphere on rheology and temperature. Nature 316, 138–142. https://doi.org/10.1038/316138a0

Kusznir, N.J., Karner, G.D., 2007. Continental lithospheric thinning and breakup in response to upwelling divergent mantle flow: application to the Woodlark, Newfoundland and Iberia margins. Geol. Soc. London, Spec. Publ. 282, 389–419. https://doi.org/10.1144/SP282.16

Kusznir, N.J., Roberts, A.M., Alvey, A.D., 2018. Crustal structure of the conjugate Equatorial Atlantic Margins , derived by gravity anomaly inversion. Geol. Soc. London, Spec. Publ. 476. https://doi.org/https://doi.org/10.1144/SP476.5

Kusznir, N.J., Roberts, A.M., Morley, C.K., 1995. Forward and reverse modelling of rift basin formation. Geol. Soc. London, Spec. Publ. 80, 33–56. https://doi.org/10.1144/GSL.SP.1995.080.01.02

Lal, N.K., Siawal, A., Kaul, A.K., 2009. Evolution of east coast of India - A plate tectonic reconstruction. J. Geol. Soc. India 73, 249–260. https://doi.org/10.1007/s12594-009-0081-1

Larsen, H.C., 1994a. 13. Summary and Principal Results. Proc. Ocean Drill. Program, Sci. Results 152, 279–292.

Larsen, H.C., 1994b. 9. Site 917. Proc. Ocean Drill. Program, Sci. Results 152.

Larsen, H.C., 1978. Offshore continuation of East Greenland dyke swarm and North Atlantic Ocean formation. Nature 274, 220–223. https://doi.org/10.1038/274220a0

Larsen, H.C., Jakobsdottir, S., 1988. Distribution, crustal properties and significance of seawards-dipping sub-basement reflectors off E Greenland. Geol. Soc. London, Spec. Publ. 39, 95–114. https://doi.org/10.1144/GSL.SP.1988.039.01.10

Larsen, H.C., Saunders, A.D., 1998. Tectonism and volcanism at the southeast Greenland rifted margin: a record of plume impact and later continental rupture. Proc. Ocean Drill. Progr. Sci. Results 152, 503–533. https://doi.org/10.2973/odp.proc.sr.152.1998

Laske, G., Masters, G., 1997. A Global Digital Map of Sediment Thickness. EOS, Trans. AGU

78.

Lau, K.W.H., Louden, K.E., Funck, T., Tucholke, B.E., Holbrook, W.S., Hopper, J.R., Christian Larsen, H., 2006. Crustal structure across the Grand Banks-Newfoundland Basin Continental Margin - I. Results from a seismic refraction profile. Geophys. J. Int. 167, 127–156. https://doi.org/10.1111/j.1365-246X.2006.02988.x

Lizarralde, D., Gaherty, J.B., Collins, J.A., Hirth, G., Kim, S.D., 2004. Spreading-rate dependence of melt extraction at mid-ocean ridges from mantle seismic refraction data. Nature 432, 744–747. https://doi.org/10.1038/nature03140

Ludwig, W.J., Nafe, J.E., Drake, C.L., 1970. Seismic Refraction, the Sea. Vol. 4 (Part 1).

Lundin, E.R., Doré, A.G., 2011. Hyperextension, serpentinization, and weakening: A new paradigm for rifted margin compressional deformation. Geology 39, 347–350. https://doi.org/10.1130/G31499.1

Magee, C., Maharaj, S.M., Wrona, T., Jackson, C.A.L., 2015. Controls on the expression of igneous intrusions in seismic reflection data. Geosphere 11, 1024–1041. https://doi.org/10.1130/GES01150.1

Magee, C., Stevenson, C.T.E., Ebmeier, S.K., Keir, D., Hammond, J.O.S., Gottsmann, J.H., Whaler, K.A., Schofield, N., Jackson, C.A.-L., Petronis, M.S., O'Driscoll, B., Morgan, J., Cruden, A., Vollgger, S.A., Dering, G., Micklethwaite, S., Jackson, M.D., 2018. Magma Plumbing Systems: A Geophysical Perspective. J. Petrol. 1–35. https://doi.org/10.1093/petrology/egy064

Manatschal, G., 2004. New models for evolution of magma-poor rifted margins based on a review of data and concepts from West Iberia and the Alps. Int. J. Earth Sci. 93, 432–466. https://doi.org/10.1007/s00531-004-0394-7

Mann, P., Gahagan, L., Gordon, M.B., 2005. Tectonic setting of the world's giant oil and gas fields. AAPG Mem. 15–105.

Mantovani, M., Peate, D.W., Hawkesworth, C., 1988. Geochemical Stratigraphy of Paraná Continental Flood Basalts: A Contribution from Borehole Samples. Mesozoic FloodVolcanism Parana Basin Sao Paulo (Inst. Astron. e Geofis. Publ.) 15–24.

Masini, E., Manatschal, G., Mohn, G., 2013. The Alpine Tethys rifted margins: Reconciling old and new ideas to understand the stratigraphic architecture of magma-poor rifted margins. Sedimentology 60, 174–196. https://doi.org/10.1111/sed.12017

McBride, J.H., White, R.S., Smallwood, J.R., England, R.W., 2004. Must magmatic intrusion in the lower crust produce reflectivity? Tectonophysics 388, 271–297. https://doi.org/10.1016/j.tecto.2004.07.055

McDermott, C., Lonergan, L., Collier, J.S., McDermott, K.G., Bellingham, P., 2018. Characterization of Seaward-Dipping Reflectors Along the South American Atlantic Margin and Implications for Continental Breakup. Tectonics 37, 3303–3327. https://doi.org/10.1029/2017TC004923

McIntosh, K., van Avendonk, H., Lavier, L., Lester, W.R., Eakin, D., Wu, F., Liu, C.S., Lee, C.S., 2013. Inversion of a hyper-extended rifted margin in the Southern Central Range of Taiwan. Geology 41, 871–874. https://doi.org/10.1130/G34402.1

McKenzie, D., 1978. Some remarks on the development of sedimentary basins. Earth Planet. Sci. Lett. 40, 25–32. https://doi.org/10.1016/0012-821X(78)90071-7

Mckenzie, D., Bickle, M.J., 1988. The volume and composition of melt generated by extension of the lithosphere. J. Petrol. 29, 625–689. https://doi.org/https://doi.org/10.1093/petrology/29.3.625

Menzies, M., Klemperer, S.L., Ebinger, C.J., Baker, J., 2002. Characteristics of volcanic rifted margins. Geol. Soc. Am. Spec. Pap. 1–14. https://doi.org/10.1130/0-8137-2362-0.1

Minshull, T. a., Dean, S.M., White, R.S., Whitmarsh, R.B., 2001. Anomalous melt production after continental break-up in the southern Iberia Abyssal Plain. Geol. Soc. London, Spec. Publ. 187, 537–550. https://doi.org/10.1144/GSL.SP.2001.187.01.26

Mjelde, R., Faleide, J.I., Breivik, A.J., Raum, T., 2009. Lower crustal composition and crustal lineaments on the Vøring Margin, NE Atlantic: A review. Tectonophysics 472, 183–193. https://doi.org/10.1016/j.tecto.2008.04.018

Mjelde, R., Kasahara, J., Shimamura, H., Kamimura, A., Kanazawa, T., Kodaira, S., Raum, T., Shiobara, H., 2002. Lower crustal seismic velocity-anomalies; magmatic underplating or serpentinized peridotite? Evidence from the Vøring Margin , NE Atlantic. Mar. Geophys. Res. 23, 169–183.

Mjelde, R., Raum, T., Myhren, B., Shimamura, H., Murai, Y., Takanami, T., Karpuz, R., Næss, U., 2005. Continent-ocean transition on the Vøring Plateau , NE Atlantic, derived from densely sampled ocean bottom seismometer data. J. Geophys. Res. 110, 1–19. https://doi.org/10.1029/2004JB003026

Mohn, G., Manatschal, G., Beltrando, M., Masini, E., Kusznir, N.J., 2012. Necking of continental crust in magma-poor rifted margins: Evidence from the fossil Alpine Tethys margins. Tectonics 31, 1–28. https://doi.org/10.1029/2011TC002961

Moore, J.G., 2001. Density of basalt core from Hilo drill hole, Hawaii. J. Volcanol. Geotherm. Res. 112, 221–230. https://doi.org/https://doi.org/10.1016/s0377-0273(01)00242-6

Mueller, C.O., Jokat, W., Schreckenberger, B., 2016. The crustal structure of Beira High, central Mozambique—Combined investigation of wide-angle seismic and potential field data. Tectonophysics 683, 233–254. https://doi.org/10.1016/j.tecto.2016.06.028

Müller, R.D., Gaina, C., Roest, W.R., Hansen, D.L., 2001. A recipe for microcontinent formation. Geology 29, 203–206. https://doi.org/10.1130/0091-7613(2001)029<0203:ARFMF>2.0.CO;2

Müller, R.D., Gaina, C., Tikku, A., Mihut, D., Cande, S.C., Stock, J.M., 2000. Mesozoic/Cenozoic tectonic events around Australia. Hist. Dyn. Glob. Plate Motions 121, 161–188.

Müller, R.D., Roest, W.R., Royer, J.Y., Gahagan, L.M., Sclater, J.G., 1997. Digital isochrons of the world's ocean floor. J. Geophys. Res. 102, 3211–3214. https://doi.org/10.1029/96JB01781

Müller, R.D., Sdrolias, M., Gaina, C., Roest, W.R., 2008. Age, spreading rates, and spreading asymmetry of the world's ocean crust. Geochemistry, Geophys. Geosystems 9, 1–19. https://doi.org/10.1029/2007GC001743

Müntener, O., Manatschal, G., Desmurs, L., Pettke, T., 2010. Plagioclase peridotites in ocean-continent transitions: Refertilized mantle domains generated by melt stagnation in the shallow mantle lithosphere. J. Petrol. 51, 255–294. https://doi.org/10.1093/petrology/egp087

Mutter, J.C., Buck, W.R., Zehnder, C.M., 1988. Convective partial melting: 1. A model for the

formation of thick basaltic sequences during the initiation of spreading. J. Geophys. Res. 93, 1031–1048. https://doi.org/10.1029/JB093iB02p01031

Mutter, J.C., Talwani, M., Stoffa, P.L., 1984. Evidence for a Thick Oceanic Crust Adjacent to the Norwegian Margin. J. Geophys. Res. 89, 483–502.

Mutter, J.C., Talwani, M., Stoffa, P.L., 1982. Origin of seaward-dipping reflectors in oceanic crust off the Norwegian margin by subaerial sea-floor spreading. Geology 10, 353–357. https://doi.org/10.1130/0091-7613(1982)10<353

Nayar, K.G., Sharqawy, M.H., Banchik, L.D., Lienhard, J.H., 2016. Thermophysical properties of seawater: A review and new correlations that include pressure dependence. Desalination 390, 1–24. https://doi.org/10.1016/j.desal.2016.02.024

Nemčok, M., Sinha, S.T., Stuart, C.J., Welker, C., Choudhuri, M., Sharma, S.P., Misra, A.A., Sinha, N., Venkatraman, S., 2013. East Indian margin evolution and crustal architecture: integration of deep reflection seismic interpretation and gravity modelling. Geol. Soc. London, Spec. Publ. 369.1, 477–496. https://doi.org/10.1144/SP369.6

Nicolaysen, K.E., Bowring, S., Frey, F.A., Weis, D., Ingle, S., Pringle, M.S., Coffin, M.F., 2001. Provenance of Proterozoic garnet-biotite gneiss recovered from Elan Bank, Kerguelen Plateau, southern Indian Ocean. Geology 29, 235–238. https://doi.org/10.1130/0091-7613(2001)029<0235

Nirrengarten, M., Manatschal, G., Yuan, X.P., Kusznir, N.J., Maillot, B., 2016. Application of the critical Coulomb wedge theory to hyper-extended, magma-poor rifted margins. Earth Planet. Sci. Lett. 442, 121–132. https://doi.org/10.1016/j.epsl.2016.03.004

Niu, Y., Bideau, D., Hekinian, R., Batiza, R., 2001. Mantle compositional control on the extent of mantle melting, crust production, gravity anomaly, ridge morphology, and ridge segmentation: a case study at the Mid-Atlantic Ridge 33-35°N. Earth Planet. Sci. Lett. 186, 383–399.

Olierook, H.K.H., Jourdan, F., Merle, R.E., Timms, N.E., Kusznir, N.J., Muhling, J.R., 2016. Bunbury Basalt: Gondwana breakup products or earliest vestiges of the Kerguelen mantle plume? Earth Planet. Sci. Lett. 440, 20–32. https://doi.org/10.1016/j.epsl.2016.02.008

Osmundsen, P.T., Ebbing, J., 2008. Styles of extension offshore mid-Norway and implications for mechanisms of crustal thinning at passive margins. Tectonics 27, 1–25. https://doi.org/10.1029/2007TC002242

Palmason, G., 1973. Kinematics and Heat Flow in a Volcanic Rift Zone, with Application to Iceland. Geophys. J. R. Astron. Soc. 33, 451–481. https://doi.org/10.1111/j.1365-246X.1973.tb02379.x

Palmason, G., Saemundsson, K., 1974. Iceland in Relation to the Mid-Atlantic Ridge. Annu. Rev. Earth Planet. Sci. 2, 25–50. https://doi.org/10.1146/annurev.ea.02.050174.000325

Parker, R.L., 1972. The Rapid Calculation of Potential Anomalies. Geophys. J. R. Astron. Soc. 31, 447–455. https://doi.org/https://doi.org/10.1111/j.1365-246x.1973.tb06513.x

Paton, D.A., Pindell, J., McDermott, K., Bellingham, P., Horn, B., 2017. Evolution of seaward-dipping reflectors at the onset of oceanic crust formation at volcanic passive margins: Insights from the South Atlantic. Geology 45, 439–442. https://doi.org/10.1130/G38706.1

Peate, D.W., Hawkesworth, C., Mantovani, M., 1992. Chemical stratigraphy of the Paraná lavas (South America): Classification of magma types and their spatial distribution. Bull. Volcanol. 55, 119–139. https://doi.org/https://doi.org/10.1007/bf00301125

Pérez-Diaz, L., Eagles, G., 2014. Constraining South Atlantic growth with seafloor spreading data. Tectonics 33, 1848–1873. https://doi.org/10.1002/2014TC003644

Pérez-Gussinyé, M., 2013. A tectonic model for hyperextension at magma-poor rifted margins: an example from the West Iberia – Newfoundland conjugate margins. Geol. Soc. London, Spec. Publ. 369, 403–427. https://doi.org/10.1144/SP369.19

Pérez-Gussinyé, M., Morgan, J.P., Reston, T.J., Ranero, C.R., 2006. The rift to drift transition at non-volcanic margins: Insights from numerical modelling. Earth Planet. Sci. Lett. 244, 458–473. https://doi.org/10.1016/j.epsl.2006.01.059

Péron-Pinvidic, G., Manatschal, G., 2009. The final rifting evolution at deep magma-poor passive margins from Iberia-Newfoundland: A new point of view. Int. J. Earth Sci. 98, 1581–1597. https://doi.org/10.1007/s00531-008-0337-9

Picazo, S., Müntener, O., Manatschal, G., Bauville, A., Karner, G., Johnson, C., 2016. Mapping the nature of mantle domains in Western and Central Europe based on clinopyroxene and spinel chemistry: Evidence for mantle modification during an extensional cycle. Lithos 266–267, 233–263. https://doi.org/10.1016/j.lithos.2016.08.029

Pickup, S.L.B., Whitmarsh, R.B., Fowler, C.M.R., Reston, T.J., 1996. Insight into the nature of the ocean-continent transition off West-Iberia from a deep-multichannel seismic reflection profile. Geology 24, 1079–1082. https://doi.org/10.1130/0091-7613(1996)024<1079

Pindell, J., Graham, R., Horn, B., 2014. Rapid outer marginal collapse at the rift to drift transition of passive margin evolution, with a Gulf of Mexico case study. Basin Res. 26, 701–725. https://doi.org/10.1111/bre.12059

Planke, S., Eldholm, O., 1994. Seismic response and construction of seaward dipping wedges of flood basalts: Voring volcanic margin. J. Geophys. Res. 99, 9263–9278. https://doi.org/10.1029/94JB00468

Planke, S., Rasmussen, T., Rey, S.S., Myklebust, R., 2005. Seismic characteristics and distribution of volcanic intrusions and hydrothermal vent complexes in the Vøring and Møre basins. Pet. Geol. North-West Eur. Glob. Perspect. – Proc. 6th Pet. Geol. Conf. 833–844. https://doi.org/10.1144/0060833

Planke, S., Symonds, P.A., Alvestad, E., Skogseid, J., 2000. Seismic volcanostratigraphy of large-volume basaltic extrusive complexes on rifted margins. J. Geophys. Res. 105, 19335–19351. https://doi.org/10.1029/1999JB900005

Quirk, D.G., Hertle, M., Jeppesen, J.W., Raven, M., Mohriak, W.U., Kann, D.J., Norgaard, M., Howe, M.J., Hsu, D., Coffey, B., Mendes, M.P., 2013. Rifting, subsidence and continental break-up above a mantle plume in the central South Atlantic. Geol. Soc. London, Spec. Publ. 369, 185–214. https://doi.org/10.1144/SP369.20

Quirk, D.G., Shakerley, A., Howe, M.J., 2014. A mechanism for construction of volcanic rifted margins during continental breakup. Geology 42, 1079–1082. https://doi.org/10.1130/G35974.1

Radhakrishna, M., Twinkle, D., Nayak, S., Bastia, R., Rao, G.S., 2012. Crustal structure and rift architecture across the Krishna-Godavari basin in the central Eastern Continental

Margin of India based on analysis of gravity and seismic data. Mar. Pet. Geol. 37, 129–146. https://doi.org/10.1016/j.marpetgeo.2012.05.005

Ramana, M. V., Nair, R.R., Sarma, K.V.L.N.S., Ramprasad, T., Krishna, K.S., Subrahmanyam, V., D'Cruz, M., Subrahmanyam, C., Paul, J., Subrahmanyam, A.S., Chandra Sekhar, D. V., 1994. Mesozoic anomalies in the Bay of Bengal. Earth Planet. Sci. Lett. 121, 469–475. https://doi.org/10.1016/0012-821X(94)90084-1

Ramana, M. V., Ramprasad, T., Desa, M., 2001. Sea floor spreading magnetic anomalies in the Enderby Basin, East Antarctica. Earth Planet. Sci. Lett. 191, 241–255.

Renne, P., Ernesto, M., Pacca, I.G., Robert, S., Glen, J., Prevot, M., Perrin, M., 1992. The Age of Parana Flood Volcanism, Rifting of Gondwanaland, and the Jurassic-Cretaceous Bounday. Sci. Rep. 258, 975–979. https://doi.org/https://doi.org/10.1126/science.258.5084.975

Renne, P.R., Deckart, K., Ernesto, M., Feraud, G., Piccirillo, E.M., 1996. Age of the Ponta Grossa dike swarm (Brazil), and implications to Parana flood volcanism. Earth Planet. Sci. Lett. 144, 199–211. https://doi.org/10.1016/0012-821X(96)00155-0

Renne, Paul R., Glen, J.M., Milner, S.C., Duncan, A.R., 1996. Age of Etendeka flood volcanism and associated intrusions in southwestern Africa. Geology 24, 659–662. https://doi.org/10.1130/0091-7613(1996)024<0659:AOEFVA>2.3.CO;2

Reston, T.J., 2009. The structure, evolution and symmetry of the magma-poor rifted margins of the North and Central Atlantic: A synthesis. Tectonophysics 468, 6–27. https://doi.org/10.1016/j.tecto.2008.09.002

Reston, T.J., 2007. Extension discrepancy of North Atlantic nonvolcanic rifted margins: Depth-dependent stretching or unrecognized faulting? Geology 35, 367–370. https://doi.org/10.1130/G23213A.1

Reston, T.J., Manatschal, G., 2011. Chapter 1, Rifted Margins: Building Blocks of Later Collision, in: Arc-Continent Collions. https://doi.org/10.1007/978-3-540-88558-0

Reynisson, R., Ebbing, J., 2010. Properties and distribution of lower crustal bodies on the mid-Norwegian margin. Geol. Soc. … 2005. https://doi.org/10.1144/0070843

Richards, M.A., Duncan, R.A., Courtillot, V.E., 1989. Flood basalts and hot-spot tracks: plume heads and tails. Science 246, 103–107. https://doi.org/10.1126/science.246.4926.103

Roberts, A.M., Kusznir, N.J., Corfield, R.I., Thompson, M., Woodfine, R., 2013. Integrated tectonic basin modelling as an aid to understanding deep-water rifted continental margin structure and location. Eage 19, 65–88. https://doi.org/10.1144/petgeo2011-046

Roberts, A.M., Kusznir, N.J., Yielding, G., Styles, P., 1998. 2D flexural backstripping of extensional basins; the need for a sideways glance. Pet. Geosci. 4, 327–338. https://doi.org/10.1144/petgeo.4.4.327

Rowland, J. V., Wilson, C.J.N., Gravley, D.M., 2010. Spatial and temporal variations in magma-assisted rifting, Taupo Volcanic Zone, New Zealand. J. Volcanol. Geotherm. Res. 190, 89–108. https://doi.org/10.1016/j.jvolgeores.2009.05.004

Royer, J.Y., Coffin, M.F., 1988. 50. Jurassic to Eocene plate tectonic reconstructions in the Kerguelen Plateau region. Proc. Ocean Drill. Progr. Sci. Results The Program.

Sallarès, V., Charvis, P., Flueh, E.R., Bialas, J., Agudelo, W., Anglade, A., Berhorst, A., Bethoux,

N., Broser, A., Calahorrano, Y., Collot, J.Y., Fekete, N., Gailler, A., Gutscher, M.A., Hello, Y., Liersch, P., Michaud, F., Müller, M., Osorio, J.A., Ravaut, C., Steffen, K.P., Thierer, P., Walther, C., Yates, B., 2005. Seismic structure of the Carnegie ridge and the nature of the Galápagos hotspot. Geophys. J. Int. 161, 763–788. https://doi.org/10.1111/j.1365-246X.2005.02592.x

Sandwell, D., Smith, W.H., 2009. Global marine gravity from retracked Geosat and ERS-1 altimetry: Ridge segmentation versus spreading rate. J. Geophys. Res. Solid Earth 114, 1–18. https://doi.org/10.1029/2008JB006008

Sauter, D., Unternehr, P., Manatschal, G., Tugend, J., Cannat, M., Le Quellec, P., Kusznir, N.J., Munschy, M., Leroy, S., Mercier de Lepinay, J., Granath, J.W., Horn, B.W., 2016. Evidence for magma entrapment below oceanic crust from deep seismic reflections in the Western Somali Basin. Geology 44, G37747.1. https://doi.org/10.1130/G37747.1

Sawyer, D.S., Coffin, M.F., Reston, T.J., Stock, J.M., Hopper, J.R., 2007. COBBOOM: The Continental Breakup and Birth of Oceans Mission. Sci. Drill. 13–25. https://doi.org/10.2204/iodp.sd.5.02.2007

Schofield, N., Heaton, L., Holford, S.P., Archer, S.G., Jackson, C.A.-L., Jolley, D.W., 2012. Seismic imaging of “broken bridges”: linking seismic to outcrop-scale investigations of intrusive magma lobes. J. Geol. Soc. London. 169, 421–426. https://doi.org/10.1144/0016-76492011-150

Sclater, J.G., Christie, P.A.F., 1980. Continental stretching: An explanation of the Post-Mid-Cretaceous subsidence of the central North Sea Basin. J. Geophys. Res. Solid Earth 85, 3711–3739. https://doi.org/10.1029/JB085iB07p03711

Sharqawy, M.H., Lienhard, J.H., Zubair, S.M., 2010. The thermophysical properties of seawater: A review of existing correlations and data. Desalin. Water Treat. 16, 354–380.

Sibuet, J.C., Srivastava, S., Manatschal, G., 2007. Exhumed mantle-forming transitional crust in the Newfoundland-Iberia rift and associated magnetic anomalies. J. Geophys. Res. Solid Earth 112, 1–23. https://doi.org/10.1029/2005JB003856

Sinha, S.T., Nemčok, M., Choudhuri, M., Sinha, N., Rao Pundarika, D., 2015. The role of break-up localization in microcontinent separation along a strike-slip margin: the East India – Elan Bank case study. Geol. Soc. London, Spec. Publ. 431.

Sinton, C.W., Duncan, R.A., 1998. 40 Ar- 39 Ar Ages of lavas from the Southeast Greenland margin, ODP Leg 152, and the Rockall Plateau, DSDP Leg 81. Proc. Ocean Drill. Program, Sci. Results 152, 387–402.

Skelton, A., Whitmarsh, R., Arghe, F., Crill, P., Koyi, H., 2005. Constraining the rate and extent of mantle serpentinization from seismic and petrological data: Implications for chemosynthesis and tectonic processes. Geofluids 5, 153–164. https://doi.org/10.1111/j.1468-8123.2005.00111.x

Skogseid, J., Eldholm, O., 1987. Early Cenozoic crust at the Norwegian continental margin and the conjugate Jan Mayen Ridge. J. Geophys. Res. Solid Earth 92, 11471–11491. https://doi.org/10.1029/JB092iB11p11471

Skogseid, J., Planke, S., Faleide, J.I., Pedersen, T., Eldholm, O., Neverdal, F., 2000. NE Atlantic continental rifting and volcanic margin formation, Geological Society, London, Special Publications. https://doi.org/10.1144/GSL.SP.2000.167.01.12

Smith, R.A., 1961. A uniqueness theorem concerning gravity fields. Math. Proc. Cambridge

Philos. Soc. 57, 865–870. https://doi.org/10.1017/S030500410003601X

Smith, W.H., Sandwell, D., 1997. Global Sea Floor Topography from Satellite Altimetry and Ship Depth Soundings. Science (80-.). 277, 1956–1962. https://doi.org/10.1126/science.277.5334.1956

Soares, D.M., Alves, T.M., Terrinha, P., 2012. The breakup sequence and associated lithospheric breakup surface: Their significance in the context of rifted continental margins (West Iberia and Newfoundland margins, North Atlantic). Earth Planet. Sci. Lett. 355–356, 311–326. https://doi.org/10.1016/j.epsl.2012.08.036

Stanton, N., Kusznir, N., Gordon, A., Schmitt, R., 2019. Architecture and Tectono-magmatic evolution of the Campos Rifted Margin: Control of OCT structure by basement inheritance. Mar. Pet. Geol. 100, 43–59. https://doi.org/10.1016/j.marpetgeo.2018.10.043

Stica, J.M., Zalán, P.V., Ferrari, A.L., 2014. The evolution of rifting on the volcanic margin of the Pelotas Basin and the contextualization of the Paraná-Etendeka LIP in the separation of Gondwana in the South Atlantic. Mar. Pet. Geol. 50, 1–21. https://doi.org/10.1016/j.marpetgeo.2013.10.015

Storey, B.C., 1995. The Role of Mantle Plumes in Continental Breakup: Case Histories from Gondwanaland. Nature 377, 301–308.

Storey, M., Duncan, R.A., Tegner, C., 2007. Timing and duration of volcanism in the North Atlantic Igneous Province: Implications for geodynamics and links to the Iceland hotspot. Chem. Geol. 241, 264–281. https://doi.org/10.1016/j.chemgeo.2007.01.016

Sutra, E., Manatschal, G., 2012. How does the continental crust thin in a hyperextended rifted margin? Insights from the iberia margin. Geology 40, 139–142. https://doi.org/10.1130/G32786.1

Sutra, E., Manatschal, G., Mohn, G., Unternehr, P., 2013. Quantification and restoration of extensional deformation along the Western Iberia and Newfoundland rifted margins. Geochemistry, Geophys. Geosystems 14, 2575–2597. https://doi.org/10.1002/ggge.20135

Talwani, M., Mutter, J.C., Eldholm, O., 1981. The initiation of opening of the Norwegian Sea. Oceanol. Acta, Spec. Issue 23–30. https://doi.org/10.1136/bmj.b3136

Thybo, H., Artemieva, I.M., 2013. Moho and magmatic underplating in continental lithosphere. Tectonophysics 609, 605–619. https://doi.org/10.1016/j.tecto.2013.05.032

Torsvik, T.H., Rousse, S., Labails, C., Smethurst, M.A., 2009. A new scheme for the opening of the South Atlantic Ocean and the dissection of an Aptian salt basin. Geophys. J. Int. 183, 29–34. https://doi.org/10.1111/j.1365-246X.2010.04728.x

Tucholke, B.E., Behn, M.D., Buck, W.R., Lin, J., 2008. Role of melt supply in oceanic detachment faulting and formation of megamullions. Geology 36, 455–458. https://doi.org/10.1130/G24639A.1

Tucholke, B.E., Sawyer, D.S., Sibuet, J.C., 2007. Breakup of the Newfoundland Iberia rift. Geol. Soc. London, Spec. Publ. 282, 9–46. https://doi.org/10.1144/SP282.2

Tugend, J., Gillard, M., Manatschal, G., Nirrengarten, M., Harkin, C.J., Epin, M.E., Sauter, D., Autin, J., Kusznir, N.J., McDermott, K., 2018. Reappraisal of the Magma-rich versus

Magma-poor Rifted Margin Archetypes. Geol. Soc. London, Spec. Publ.

Tugend, J., Manatschal, G., Kusznir, N.J., 2015. Spatial and temporal evolution of hyperextended rift systems: Implication for the nature, kinematics, and timing of the Iberian-European plate boundary. Geology 43, 15–18. https://doi.org/10.1130/G36072.1

Tugend, J., Manatschal, G., Kusznir, N.J., 2014a. Characterizing , identifying and mapping structural domains at rifted continental margins : insights from the Bay of Biscay margins and its Pyrenean fossil analogue. Geol. Soc. London, Spec. Publ. 413, 8416. https://doi.org/10.1002/2014TC003529

Tugend, J., Manatschal, G., Kusznir, N.J., Masini, E., Mohn, G., Thinon, I., 2014b. Formation and deformation of hyperextended rift systems: Insights from rift domain mapping in the Bay of Biscay-Pyrenees. Tectonics 33, 1239–1276. https://doi.org/10.1002/2014TC003529

Turner, S., Regelous, M., Kelley, S., Hawkesworth, C., Mantovani, M., 1994. Magmatism and continental break-up in the South Atlantic: high precision 40Ar-39Ar geochronology. Earth Planet. Sci. Lett. 121, 333–348. https://doi.org/10.1016/0012-821X(94)90076-0

Viereck, L.G., Taylor, P.N., Parson, L.M., Morton, a. C., Hertogen, J., Gibson, I.L., 1988. Origin of the Palaeogene Voring Plateau volcanic sequence. Geol. Soc. London, Spec. Publ. 39, 69–83. https://doi.org/10.1144/GSL.SP.1988.039.01.08

W.J. Morgan, 1971. Convection Plumes in Lower Mantle. Nature 230, 42–43.

Wager, L.R., Deer, W.A., 1938. A Dyke Swarm and Crustal Flexure in East Greenland. Geol. Mag. 75, 39–46. https://doi.org/10.1017/S0016756800089226

Waichel, B.L., Tratz, E.B., Pietrobelli, G., Jerram, D.A., Calixto, G.R., Bacha, R.R., Tomazzolli, E.R., da Silva, W.B., 2013. Lava tubes from the Paraná-Etendeka Continental Flood Basalt Province: Morphology and importance to emplacement models. J. South Am. Earth Sci. 48, 255–261. https://doi.org/10.1016/j.jsames.2013.10.005

Walker, G.P.L., 1981. Evidence of Crustal Drift from Icelandic Geology. Philos. Trans. R. Soc. London.

Walker, G.P.L., 1960. Zeolite zones and dike distributions in relation to the structure of the basalts of eastern iceland. J. Geol. 68, 515–528. https://doi.org/10.1086/626685

Walker, G.P.L., 1959. Geology of the Reydarfjördur area, Eastern Iceland. Q. J. Geol. Soc. 114, 367–391. https://doi.org/https://doi.org/10.1144/gsjgs.114.1.0367

Warner, M.R., 1987. Seismic reflections from the Moho - the effect of isostasy. Geophys. J. R. Astron. Soc. 88, 425–435. https://doi.org/10.1111/j.1365-246X.1987.tb06651.x

White, J.D.L., McPhie, J., Soule, S.A., 2015. Submarine Lavas and Hyaloclastite, Second Edi. ed, The Encyclopedia of Volcanoes. Elsevier Inc. https://doi.org/10.1016/B978-0-12-385938-9.00019-5

White, R.S., 1992. Magmatism during and after continental break-up. Geol. Soc. London, Spec. Publ. 68, 1–16. https://doi.org/10.1144/gsl.sp.1992.068.01.01

White, R.S., McKenzie, D., 1995. Mantle plumes and flood basalts. J. Geophys. Res. Solid Earth 100, 17543–17585. https://doi.org/10.1029/95jb01585

White, R.S., McKenzie, D., 1989. Magmatism at rift zones: The generation of volcanic

continental margins and flood basalts. J. Geophys. Res. 94, 7685. https://doi.org/10.1029/JB094iB06p07685

White, R.S., McKenzie, D., O'Nions, R.K., 1992. Oceanic crustal thickness from seismic measurements and rare earth element inversions. J. Geophys. Res. 97, 19683. https://doi.org/10.1029/92JB01749

White, R.S., Smith, L.K., 2009. Crustal structure of the Hatton and the conjugate east Greenland rifted volcanic continental margins, NE Atlantic. J. Geophys. Res. Solid Earth 114, 1–28. https://doi.org/10.1029/2008JB005856

White, R S, Smith, L.K., Roberts, a W., Christie, P. a F., Kusznir, N.J., Roberts, a M., Healy, D., Spitzer, R., Chappell, a, Eccles, J.D., Fletcher, R., Hurst, N., Lunnon, Z., Parkin, C.J., Tymms, V.J., 2008. Lower-crustal intrusion on the North Atlantic continental margin. Nature 452, 460–464. https://doi.org/10.1038/nature06687

White, R. S., Smith, L.K., Roberts, A.W., Christie, P.F., Kusznir, N.J., Roberts, A.M., Healy, D., Spitzer, R., Chappell, A.R., Eccles, J.D., Fletcher, R., Hurst, N., Lunnon, Z., Parkin, C.J., Tymms, V.J., 2008. Lower-crustal intrusion on the North Atlantic continental margin. Nature 452, 460–464. https://doi.org/10.1038/nature06687

Whittaker, J.M., Goncharov, A., Williams, S.E., Müller, R.D., Leitchenkov, G., 2013. Global sediment thickness data set updated for the Australian-Antarctic Southern Ocean. Geochemistry, Geophys. Geosystems 14, 3297–3305. https://doi.org/10.1002/ggge.20181

Wilson, J.T., 1973. Mantle plumes and plate motions. Tectonophysics 19, 149–164.

Wilson, J.T., 1963. A possible origin of the Hawaiian Islands. Can. J. Earth Sci. 41, 863–870.

Wilson, R.C.L., Manatschal, G., Wise, S., 2001. Rifting along non-volcanic passive margins: stratigraphic and seismic evidence from the Mesozoic successions of the Alps and western Iberia. Geol. Soc. London, Spec. Publ. 187, 429–452. https://doi.org/10.1144/GSL.SP.2001.187.01.21

Zehnder, C., Mutter, J., Buhl, P., 1990. Deep Seismic and geochemical constraints on the nature of rift-induced magmatism during breakup of the North Atlantic. Tectonophysics 173. https://doi.org/10.1016/0040-1951(90)90245-4